Long-term variation in cosmic-ray modulation

MG Mosotho

23853786

Dissertation submitted in partial fulfilment of the requirements for the degree *Magister Scientiae* in Space Physics at the Potchefstroom Campus of the North-West University

Supervisor: Dr H Krüger

Co-supervisor: Prof RA Burger

May 2017

It all starts here ™

NORTH-WEST UNIVERSITY ®
YUNIBESITI YA BOKONE-BOPHIRIMA
NOORDWES-UNIVERSITEIT

Acknowledgements

I would like to express my gratitude to my supervisor, Dr. Helena Krüger. Her essential guidance has been helpful and her moral support is really appreciated as it enabled me to complete this dissertation. I can only say that I am very thankful for her patience throughout these years. I would like to thank my co-supervisor, Prof. Adri Burger for his useful discussion and his assistance on various occasions. This dissertation would not have been possible without their work. I have greatly benefited from the advice of the late Prof. Harm Moraal and I am pleased to acknowledge my debt to him. I would like to thank him for teaching me everything I know about the modulation parameters and his willingness to help with all problems that arose in this study.

I would like to recognize the excellent service which I have received from the Centre for Space Research at the NWU Potchefstroom campus. I am obliged to

- The physics department for their generous financial support, and for the use of their office and computer facilities.
- Mrs. P. Sieberhagen for handling all my financial inquiries most efficiently.
- Mrs. L. van Wyk and Mrs. E. van Rooyen for handling various administrative issues.
- Mr. M. Holleran for his help with computer-related problems.
- The Natural Sciences Library for providing me with information on the use of all the library facilities and how to find scientific information on accredited academic journals.

A special thanks to

- My parents for their encouragement, love, and support.
- My special friend, Ncebakazi Cebani, for her love, encouragement, and endless faith in me and for sharing my dreams.
- The National Research Foundation and the South African National Space Agency for financial support throughout this study.
- Our Heavenly Father, to whom I am eternally grateful for His grace to have allowed me to complete this work.

Mosotho Moshe Godfrey

Centre for Space Research, North-West University,

November 2016

Abstract

The transport of cosmic rays inside the heliosphere can be described by the Parker equation (*Parker*, 1965). Since there are no full analytical solutions to the Parker equation, two first-order approximate solutions of the equation can be derived, namely the Convection-Diffusion and the Force-Field approximations. These approximations were implemented to account for heliospheric modulation only. Utilizing the Force-Field approximations, *Usoskin et al.* (2011) calculated the modulation potentials between 1936 and 2009 using the ionization chamber and neutron monitor data. The normalized difference between the calculated modulation potentials by *Usoskin et al.* (2005) and *Usoskin et al.* (2011) is 3.4 % for solar maximum in June 1991. According to *Usoskin et al.* (2011), their lower calculated values compared with the earlier study are related to the addition of the third neutron monitor yield function. Despite that, these authors argue that these new calculated modulation potentials remain consistent with the old values within the uncertainties.

Herbst et al. (2010) have shown that the calculation of modulation potentials do not only depend on the Local Interstellar Spectrum but also on the energy (or rigidity) range of interest. These authors pointed out that the use of a different LIS can cause the calculated modulation potential to either increase or decrease. Based on these findings, this study re-calculated the modulation potentials by *Usoskin et al.* (2005, 2011). To investigate modulation this study uses both space-borne (i.e. PAMELA, IMP - 8 and Voyager - 1) and ground-based detectors (SANAE, Hermanus, Potchefstroom and Tsumeb neutron monitors). The

equivalence, validity and limitations of the Convection-Diffusion and Force-Field approximate solutions are employed at neutron monitor energies. The modulation potential results of this study are found to be in accordance with that found by other authors and in particular *Ghelfi et al.* (2016). There is a significant difference though between the results of this study and *Usoskin et al.* (2005, 2011) especially during solar maximum periods.

Keywords: Galactic cosmic rays, Modulation, Force-Field approximation, Convection-Diffusion approximation, Neutron monitors, Yield functions, proton fluxes, local interstellar spectrum.

Nomenclature

AU	Astronomical unit (1 AU = 1.49×10^8 km)
LISM	Local interstellar medium
LIS	Local interstellar spectrum
IMP - 8	Interplanetary Monitoring Platform 8
PAMELA	Payload for Antimatter Matter Exploration and Light Nuclei Astrophysics
NWU	North-West University

Table of Contents

Chapter 1

Introduction

The dynamic nature of the sun has captured the interest of scientists since the early 1600s. The sun, located at the centre of our solar system, is by definition at a distance of one astronomical unit (1 AU = 1.49×10^8 km) from earth. The sun is known to go through various non-stationary active processes. Such non-stationary and non-equilibrium (sometimes eruptive) processes can generally be interpreted as solar activity. These temporal changes are the major drivers of climate changes on earth. Modern science records provide us with an important source of knowledge about the manner in which solar activity rises and falls. The best-known indicator of solar activity is the sunspot number. Sunspots are visible dark spots appearing on its surface when the sun is active during a period known as solar maximum. However, when few or no sunspots appear on the surface of the sun the period is known as solar minimum.

As the sun moves through interstellar space, it blows a magnetic bubble into the interstellar space by means of its solar wind. This bubble is known as the heliosphere, named by Leverett Davis in 1955 (*Davis*, 1955). The heliosphere is constantly bombarded by numerous highly energetic atomic and subatomic particles, known as galactic cosmic rays, with energies larger than 1 MeV. The study of the effects of the heliosphere on the propagation of galactic cosmic rays from interstellar space to the earth is of great importance. As these particles enter the heliosphere, they interact with the solar wind and the heliospheric magnetic field. This interaction causes the intensities of these particles to change as a function of position, energy and time, a process known as the modulation of cosmic rays. In the

heliosphere, modulation of cosmic rays involves four major processes, namely (1) diffusion, (2) convection, (3) energy changes, e.g. adiabatic cooling and (4) drift effects. These processes are quantitatively combined and described by the full Parker transport equation (*Parker*, 1963, 1965). The quantities required to describe the transport equation and its solution include the diffusion tensor, which can be approximated as a function of heliocentric radial distance and rigidity, the interstellar energy spectrum and the solar wind speed.

Luckily, measurements over sufficiently large regions of energy, heliocentric radial distance, and time are now available and the interstellar energy spectrum parameters can now be calculated. However, it has not been possible to obtain an analytical solution to the full Parker transport equation for reasonably accurate forms of the approximated diffusion coefficients. There are numerous analytical approximations in existence but it is difficult to assess to what extent these approximations are valid, see e.g. *Gleeson* and *Axford* (1968a), *Burger* (1971), *Burger* and *Swanenburg* (1971), *Bedijn et al.* (1973) and *Caballero-Lopez* and *Moraal* (2004). The most commonly used semi-analytical approximate solutions of the full Parker transport equation are calculated from the Convection-Diffusion and the Force-Field approximations. The Force-Field approximation describes the modulation of cosmic rays as energy (or rigidity) losses at the same intensity measured from primary cosmic-rays. However, the Convection-Diffusion approximation describes modulation of cosmic rays as a reduction in intensity at the same rigidity between earth and the boundary of the heliosphere (*Gleeson* and *Axford*, 1968a; *Caballero-Lopez* and *Moraal*, 2004). In literature, this reduction in intensity is denoted by M and energy (or rigidity) losses are denoted by ϕ. The description of parameters has led to some confusion in the

literature. Hence, in this study both M and ϕ are known as modulation parameters.

Knowledge of the behaviour of modulation of cosmic rays on long time scales is important. On the ground cosmic-rays are detected by neutron monitors. This has been the main instrument used to study the long-term variations of cosmic rays since the 1950s. The count rates of neutron monitors during the last decades are dominated by the 11-year solar activity cycles which anti-correlate with sunspot numbers. The 22-year solar magnetic cycle is reflected in the alternating sharp and flat peaked cosmic-ray maxima. Data from ionization chambers can be used to study cosmic-ray variations since the early 1930s or Beryllium-10 (^{10}Be) concentration extracted from ice over a period of several centuries (*McCracken* and *Beer*, 2007; *Beer et al.*, 2012).

Attempts were made to calculate time-dependent modulation parameters in the past, in the framework of the Force-Field approximation. However, most of the results are based on different datasets or methodologies and therefore the results are not easy to compare with each other. *Usoskin et al.* (2005, 2011) calculated the modulation parameters using the Force-Field approximation. The main focus of this study is to re-calculate the modulation parameters obtained by *Usoskin et al.* (2005, 2011) by using both the Convection-Diffusion and the Force-Field approximations. Throughout this study, it is important to keep in mind that the modulation parameters calculated cannot reproduce the exact data used. This occurs because the count rates or intensities used might be suppressed or distorted by these approximate solutions calculated from the full Parker transport equation. The focus of this study is, however, primarily on what these results suggest about the behaviour of the calculated modulation parameters for all chosen neutron monitors in this study.

The structure and chapters of this study are as follows:

Chapter 2: This chapter gives an introduction to the dynamic nature of the sun, the solar wind, the heliospheric magnetic field, the heliosphere along with its boundaries and cosmic rays. The last section of this chapter gives a brief summary on the propagation of galactic cosmic rays from the interstellar space to earth.

Chapter 3: This chapter serves to introduce the most important space-borne and ground-based detectors used in this study. These detectors are important in the following chapters as they are used in this study to explain the variations in primary cosmic-ray intensities and secondary cosmic-ray count rates. The data chosen in this study were adopted from the Interplanetary Monitoring Platform 8 (IMP - 8) satellite, Payload for Antimatter Matter Exploration and Light-nuclei Astrophysics (PAMELA) satellite-borne experiment and Voyager - 1. At earth, the nucleonic component of secondary cosmic rays is detected using neutron monitors. Prior to neutron monitors, different detectors existed such as ionization chambers, Geiger-Müller counters and muon telescopes. Furthermore, the radionuclide such as ^{10}Be produced from nucleonic component of secondary cosmic rays can be used to study the behaviour of cosmic rays with solar activity, currently and over a period of several centuries. After discussing these detectors, the concepts of response functions and differential response functions are introduced. Following that, the chapter ends with a discussion of the neutron monitor yield functions.

Chapter 4: Here, the modulation of cosmic rays is discussed. This is followed by the transport equation of cosmic rays which combines all four major processes that cosmic rays undergo inside the heliosphere, the diffusion tensor used in this study and the assumptions used to simplify the full Parker transport equation. The approximate solutions of the full

Parker equation described by modulation parameters M and ϕ, are discussed.

Chapter 5: In this chapter, a detailed calculation of the monthly values of the modulation parameters using data of four neutron monitor stations (with the oldest station having data from July 1957) until October 2016 is discussed.

Chapter 6: A detailed calculation of the modulation parameters using data from IMP - 8, PAMELA and Voyager - 1 is discussed in this chapter.

Chapter 7: This chapter compares the modulation parameters to each other and to those calculated by *Usoskin et al.* (2005, 2011).

Chapter 8: In this final chapter a summary, conclusions and recommendations are given.

Chapter 2

The sun, the heliosphere and cosmic rays

2.1 Introduction

The heliosphere is constantly bombarded by highly energetic charged particles known as galactic cosmic rays which are produced at astrophysical sources in our galaxy. These particles enter the heliosphere from all directions. Once inside the heliosphere they interact with the solar wind and the heliospheric magnetic field embedded on the sun's surface. Since their discovery more than 100 years ago, significant progress has been made in understanding their evolution and propagation inside the heliosphere.

In this chapter, important concepts and processes regarding cosmic rays are introduced. An overview is given of the heliosphere, the solar wind, the heliospheric magnetic field and the related solar cycles. Cosmic rays, in particular galactic cosmic rays, are the main species discussed in this study. The propagation of these particles coming from the galaxy, propagating through the heliosphere, the geomagnetic field, and atmosphere of the earth before they are detected on the ground, is discussed. At the end of this chapter a brief summary is given. The following chapters use the concepts and nomenclatures introduced in this chapter.

2.2 The sun and solar activity cycles

The sun is a star composed of gaseous hot ionized plasma and its mass is about 2.0×10^{30} kg, which is 300 000 times more massive than the earth. The main elements present in the sun are hydrogen (92 %), followed by helium (7.8 %), and less than 1 % of heavier elements like oxygen, carbon, nitrogen and neon. Its surface temperature is about 5 873 K and close to its centre the temperature is about 15 000 000 K. The sun is thermally conductive with a plasma density of about 1.41 kg.m^{-3} (*Wilkinson*, 2012).

The sun is located at an average distance of 1 AU from the earth. It possesses a magnetic field, as in a typical magnetic dipole, where it has opposite polarities in the northern and southern hemispheres. Further, the sun can be divided into six different regions, as shown in Figure 2.1 (a), namely, the core, the radiative zone, the convection zone, the photosphere, the chromosphere and the corona. The visible surface of the sun is known as the photosphere. However, the sun's outermost layer, known as the solar corona, is less bright than the photosphere and it is not confined to the sun's surface. This layer continuously expands away from the sun at very high speeds in the form of a continuous stream of ionized gas, known as the solar wind (discussed in the next section). The sun continuously loses mass, approximately 10^{-14} solar masses per year, by means of this outflow (*Hanslmeier*, 2002).

The sun is known to go through various non-stationary active processes. Such non-stationary and non-equilibrium (sometimes eruptive) processes can be generally interpreted as solar activity. Modern science records provide us with an important source of knowledge about the manner in which solar activity rises and falls (*Usoskin*, 2013). The best-known indicator of solar activity is the sunspot number. Sunspots are visible dark

spots appearing on the photosphere, filling the umbra and penumbra (*Moore* and *Rabin*, 1985). The umbra is the inner, dark region of a sunspot. The penumbra is the outer, light region of a sunspot surrounding the umbra (*Moore* and *Rabin*, 1985; *Scharmer*, 2002).

An example of sunspots on the photosphere is shown in Figure 2.1 (b). The sunspots result due to the temperature drop at a localized area compared with the entire photosphere (*Usoskin*, 2013). Sunspots appear mostly in magnetic regions with coronal magnetic field strengths of about 0.3 T in the centre of the umbra (nearly vertical to the sun's surface). They also appear on the outer penumbra where the field is about 0.1 T (nearly horizontal or parallel to the surface). Evidently, sunspots appear in isolation, but often they originate as a set of two, one with a north and the other one with a south coronal magnetic field (*Moore* and *Rabin*, 1985). At the equator, sunspots take 25 days to move once around the sun and at the poles it takes 36 days (*Wilkinson*, 2012).

Since around 1600, scientists have recorded the advents and departures of these sunspots on the sun. Their measurements directly reflect the current state of the sun, thereby providing us with valuable information about the solar activity cycles. The activity on the sun varies on a time-scale of approximately 11-years. This regular pattern, known as the solar activity cycle, is assumed to be the result of the solar differential rotation and the related internal solar dynamo (*Babcock*, 1961; *Schwadron et al.*, 2008). When the sun is particularly active, numerous dark sunspots are visible on its surface (as seen in Figure 2.1 (b)). This period of maximum visible sunspots is known as solar maximum and the period when only few or no sunspots appear is known as solar minimum. The time from 1755 to 1766 ($\approx$ 11 years) has been chosen as solar cycle number 1 and currently (2016) the solar cycle is at number 24.

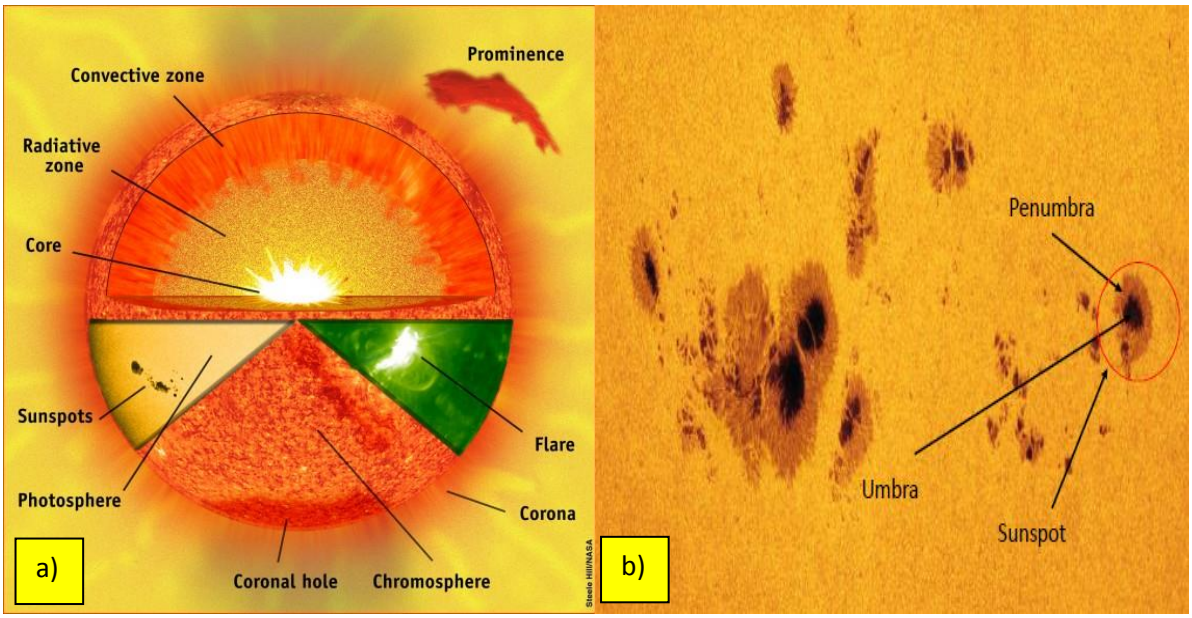

Figure 2.1: Different features observed on the sun. Panel (a) shows different regions of the sun and its layers. Source: *http//www.the.suntoday.org/overview/layers-of-thesun/*. Panel (b) shows visible sunspots during solar maximum. Source: *https//en.wikipedia.org/wiki/sunspot*.

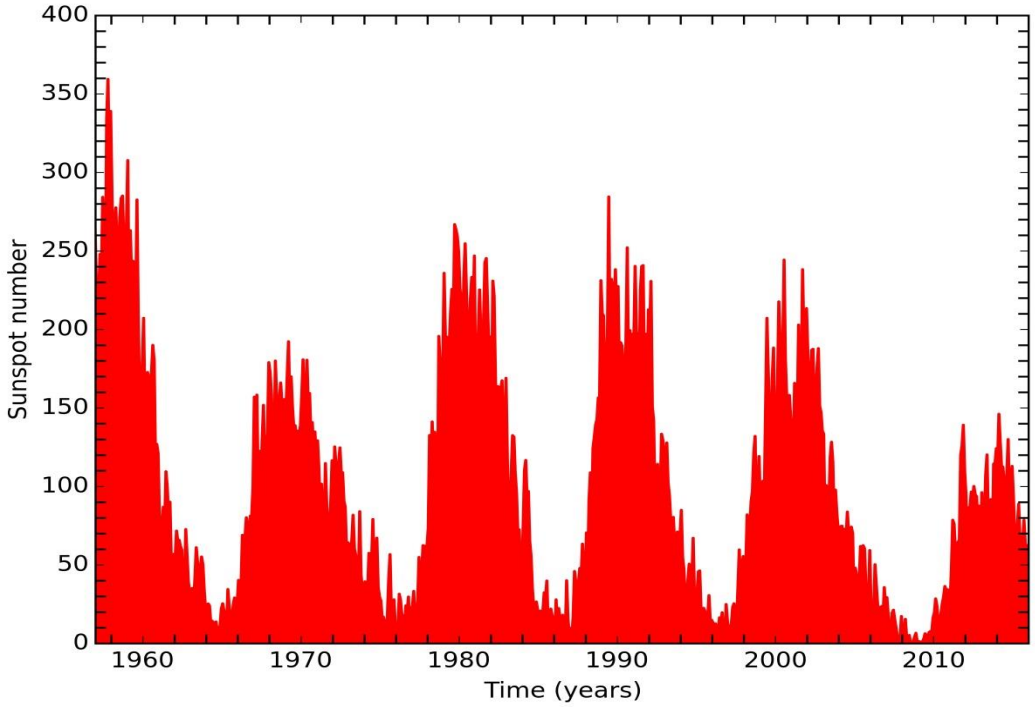

Figure 2.2: The monthly-averaged sunspot numbers as a function of time from July 1957 to October 2016. From this graph, the 11-year solar activity cycle is clearly seen in the sunspot numbers. Data source: *http//www.sidc.be/silso/*.

Figure 2.2 shows the monthly averaged sunspot numbers that are direct indications of the level of solar activity from July 1957 to October 2016. The year 2009 saw the longest and weakest solar minimum since scientists have been monitoring the sun with space-based instruments. For a detailed description of the concept of solar activity and a discussion of observational methods, see e.g. *Hathaway* and *Wilson* (2004); *Balogh et al.* (2008); *Hathaway* (2010); *Usoskin* (2013) and *Clette et al.* (2014).

2.3 The heliosphere

The heliosphere is defined as the local region of interstellar space influenced by the sun. In 1958, Eugene Parker provided an important vision explaining the manner in which the sun controls the gas density and magnetic field throughout the heliosphere. He showed that the high solar coronal temperatures imply that the magnetized plasma emerging from the sun's photosphere constantly blows radially away from the sun to maintain dynamic equilibrium. He called this plasma the solar wind. As the solar wind expands, it remains unaffected by the planetary bodies in the heliosphere (*Parker*, 1958; 1963). The solar wind observed at earth moves with a proton plasma speed of about 400 $km.s^{-1}$ in the equatorial plane of the sun and about 800 $km.s^{-1}$ in the solar polar regions. Confirmation of this plasma speed variations was provided by measurements from the Ulysses space mission (*Heber* and *Potgieter*, 2006; 2008).

Since the solar wind consists of fully ionized plasma, it has a high electric as well as thermal conductivity. Hence, the plasma cannot move across the magnetic field lines embedded at the sun's coronal holes, according to Lenz's law. Therefore, the sun's magnetic field is frozen into this plasma. As the magnetic field radially moves away from the sun with the solar

wind into the interplanetary space, it remains attached to the rotating sun resulting in a field known as the Parker spiral field (*Parker*, 1958; 1963). In the interplanetary space, this magnetic field is known as the interplanetary magnetic field or the heliospheric magnetic field.

The interstellar medium is known to consist of some mixture of dust, magnetic field, neutral gas, ionized plasma and highly energy charged particles (*Smith*, 2001). The expansion of the solar wind reaches a point where its pressure is counter-balanced by that of the local interstellar medium (LISM). At this region, where the solar wind meets the LISM, a strong standing shock wave is created, known as the termination shock. The existence of this shock was first suggested by Parker in 1961 (*Parker*, 1961). Its confirmation was obtained from two National Aeronautics and Space Administration (NASA) spacecraft measurements, namely Voyager - 1 and Voyager-2. Voyager - 1 crossed the termination shock at $\sim$ 94 AU (*Stone et al.*, 2005) and Voyager-2 crossed it at $\sim$ 84 AU away from the sun (*Stone et al.*, 2008).

Beyond the termination shock, there is a thick region known as the heliosheath, which is distinguished by its slow-moving solar plasma. Beyond the heliosheath, the heliopause exists at a distance of $\sim$ 120 AU from the sun (*Stone et al.*, 2013). Beyond the heliopause, a bow shock is expected where the interstellar plasma is decelerated from supersonic to subsonic speeds. Recent measurements from the Interstellar Boundary Explorer spacecraft mission suggest a bow wave exists far beyond the heliopause rather than a bow shock (*McComas et al.*, 2012). Figure 2.3 shows a schematic representation of the major features of the heliosphere and its boundaries.

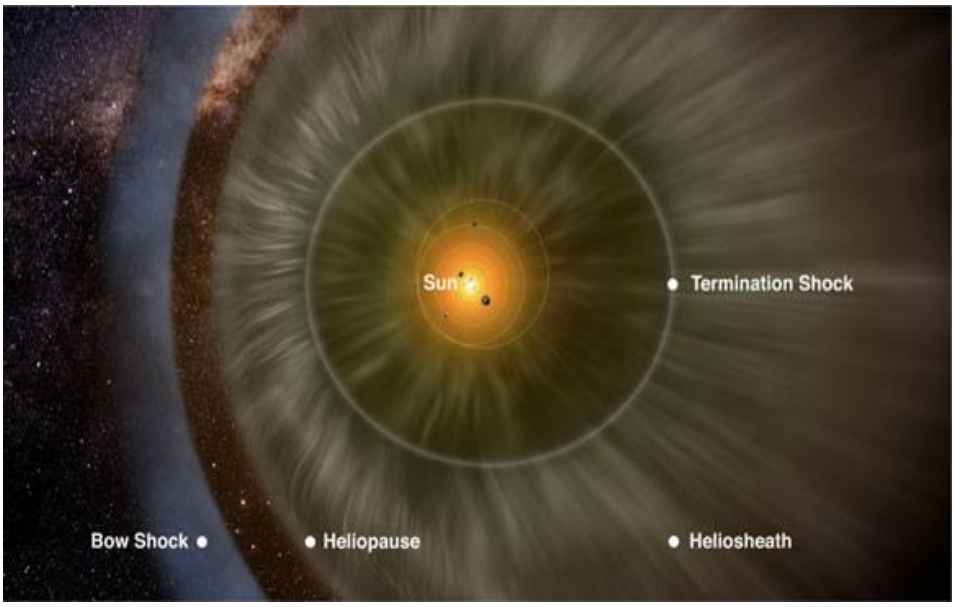

Figure 2.3: The graphic representation of the heliosphere and its boundaries. Source: *https//www.nasa.gov/pdf/623511main_IBEX_lithograph.pdf*.

2.4 The galaxy

The word galaxy is derived from the ancient Greek term literally meaning Milky (*Gaggero*, 2012). Our galaxy is a system of 10^{11} stars, plus nebulae filled with gas and dust, held together by gravitational attraction, and has the shape of a flat disk. The radius of the galaxy is about 15 kpc (1 pc = 3.1×10^{16} m = 3.26 light years). It rotates with respect to its centre of gravity with a time of 2×10^{8} years and forms a spiral structure. The schematic diagram of this spiral is shown in Figure 2.4 panel (a) and (b). The origin of the magnetic fields in the universe is still a mystery (*Widrow*, 2002). Since the galactic magnetic field was discovered more than 60 years ago, the field of research has grown (*Hiltner*, 1949). While direct measurements of the galactic magnetic field are not possible, a host of indirect methods exists. The strength of this field is about 1 nT and is directed along the spiral arms.

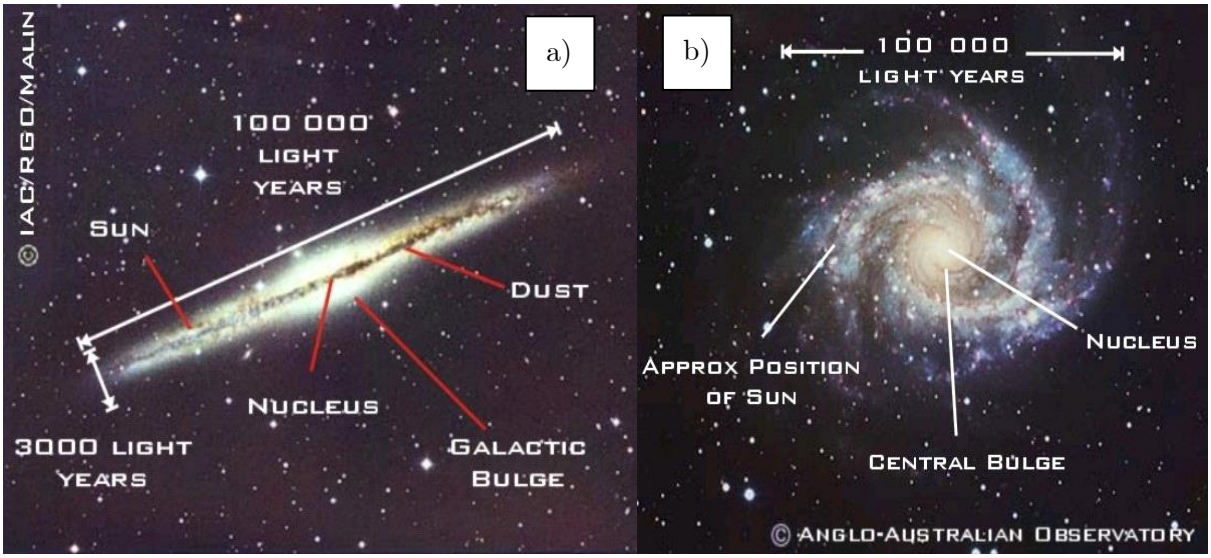

Figure 2.4: The view of the galaxy from above (panel (a)) and from the side (panel (b)). Source: *https//www.le.ac.uk/ph/faulkes/web/galaxies/r_ga_milky.html*.

2.5 Cosmic rays

The discovery of cosmic rays is universally attributed to an Austrian nuclear physicist Victor Franz Hess, who was awarded the Nobel Prize in physics in 1936 for his discovery. Before that, experiments and hypotheses were proposed by different scientists for the ionization rate measurements in the atmosphere of the earth. Hence, Hess gave the final answer to the problem after many balloon flights with different instruments on board.

He pointed out that radiation increased with height, in contrast to what was expected. From his measurements, Hess concluded that this radiation, which is now called cosmic rays (after the name was proposed by Robert Andrews Millikan in 1925), is coming from outside the atmosphere of the earth. Generally, cosmic rays are high-energy charged particles, originating mainly from outside the heliosphere but some originate inside the heliosphere.

Inside the heliosphere, cosmic rays can be classified into four main groups, namely

i) **Galactic cosmic rays**:

These are energetic charged particles produced at astrophysical sources such as supernova remnants in our galaxy (*Fisk* and *Gloeckler*, 2012).

ii) **Solar cosmic rays**:

These energetic charged particles originate from solar flares especially when the sun gets active. The coronal mass ejections can also create these particles through diffusive shock acceleration. Solar cosmic rays usually have energies up to 100 MeV, but are observed only for a few hours before they dissipate (*Forbush*, 1946; *Cliver*, 2000).

iii) **Anomalous cosmic ray component**:

These particles arrive in the heliosphere as neutral interstellar atoms. They become singly ionized relatively close to the sun, either through charge-exchange or photo-ionization (*Pesses et al.*, 1981). These ions are then "picked up" by the heliospheric magnetic field, now known as pick-up ions, and transported by the solar wind to the termination shock where they are accelerated through a process of first order Fermi acceleration up to energies of 100 MeV (*Fichtner*, 2001; *Strauss*, 2010).

iv) **Jovian electrons**:

These particles originate in Jupiter's large magnetic field. They dominate the low energy electron spectrum within the first 10 AU from the sun (*Ferreira* 2002; *Potgieter* 2008; *Ferreira* and *Potgieter* 2004).

2.6 The energy spectrum of cosmic rays

The energy spectrum of cosmic rays is the mean number of cosmic particles, per surface unit, per time unit, per solid angle unit and per energy unit that reach the earth (see Figure 2.5). This spectrum can be described by a power law equation of the form given below for almost all energies as

$$j_{\mathrm{T}}(\mathrm{T}) \propto \mathrm{T}^{-\gamma}, \tag{2.1}$$

where γ is the spectral index which changes with energy, T, taking the approximate values summarized in Table 2.1.

Table 2.1: Cosmic-ray classifications and their properties (*http://antares.in2p3.fr/users/bailey/thesis/html/node16.html*).

Types of cosmic rays	Spectral index (γ)	Energy range (eV)
Anomalous cosmic rays and jovian electrons	2.6	$10^7 < \mathrm{T} < 10^9$
Solar cosmic rays	2.7	$< 10^7$
Galactic cosmic rays	2.8	$10^{10} < \mathrm{T} < 10^{15}$
Extragalactic cosmic rays	3.0	$> 10^{15}$

The spectrum in Figure 2.5 has a change in slope, known as the "knee", at $10^{15.5}$ eV. For particles of galactic origin, this spectrum shows a power law distribution of the form $\mathrm{T}^{-2.8}$, from 10^{10} eV to 10^{15} eV. Another change in slope, known as the "ankle", occurs near 10^{17} eV. The spectrum above 10^{15} eV is considered the origin of extragalactic cosmic rays with a power law distribution of the form $\mathrm{T}^{-3.0}$. The oxygen spectrum is also shown, which indicates the presence of anomalous cosmic rays at 10^7 eV $<$ T $<$

10^9 eV with a power law distribution of the form $T^{-2.6}$. Beneath 10^7 eV, the particles are considered to be of solar origin with a power law distribution of the form $T^{-2.7}$ and there is a rise in their spectrum, as seen from the figure. These features of cosmic ray energy spectra will be re-visited and discussed in chapter 6.

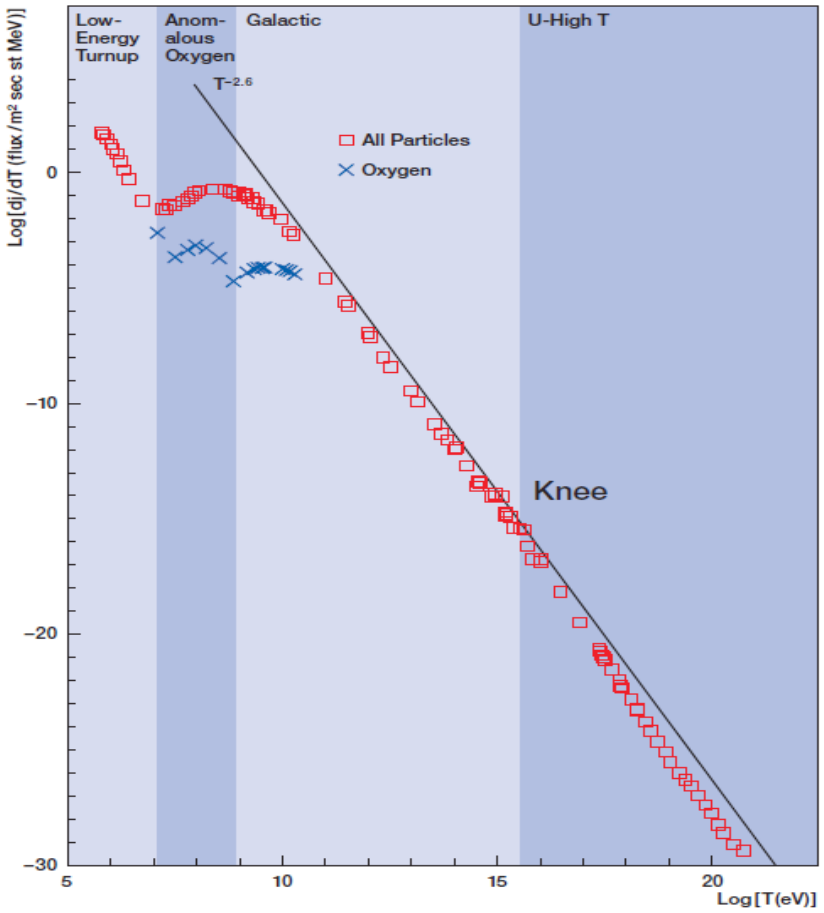

Figure 2.5: The differential energy spectrum of cosmic rays near earth. Source: *Schlaepfer* (2003).

2.7 The origins of galactic cosmic rays: Astrophysical sources

Galactic cosmic rays are the dominant particle population in the solar system, consisting mostly of hydrogen and helium ions. These particles have high energies (10^{10} eV $< T <$ 10^{15} eV). They are produced mainly in the galaxy and transported through the heliosphere to reach the earth. In

the heliosphere, they undergo processes that are discussed in sections 4.1, 6.2.1 and 6.2.2, which depend on the solar activity, the magnetic field embedded in the solar wind, and the geomagnetic field.

Black holes, pulsars, active galactic nuclei, neutron stars, quasars, supernovae and some unknown sources, all have been implicated as possible sources of galactic cosmic rays. However, progress has been slow to produce evidence as whether or not these are good galactic candidates for these particles.

A supernova is a stellar explosion that briefly outshines an entire galaxy. This kind of explosion radiates as much energy as the sun or any ordinary star. Therefore, according to NASA, a supernova can occur in two different ways, i.e.

i) **Binary star systems:**

   Binary stars are two stars that orbit the same point. One of the stars is a carbon-oxygen white dwarf. This star steals matter from its companion star. Finally, the carbon-oxygen white dwarf star gathers too much matter. Having accumulated too much matter from its companion star, this causes the star to explode resulting in a supernova (*http//www.nasa.gov/audience/forstudents/5-8/what-is-a-supernova.html*).

ii) **Dying stars:**

   When a star runs out of nuclear fuel, its mass flows into its core. Finally, the core becomes so heavy to a point where it cannot resist its own gravitational force. Therefore, the core collapses and results in a huge explosion of a supernova (*http//www.nasa.gov/audience/forstudents/5-8/what-is-a-supernova.html*).

Supernovae explosions have energies between 10^5 eV and $3.2{\times}10^{20}$ eV. Moreover, galactic cosmic rays perhaps originate not only from such explosions, but also from supernova remnants which may include neutron stars (*Ginzburg and Syrovatskii*, 1969). Figure 2.6 shows a star (supernova) exploding into billions of pieces sending off shock waves.

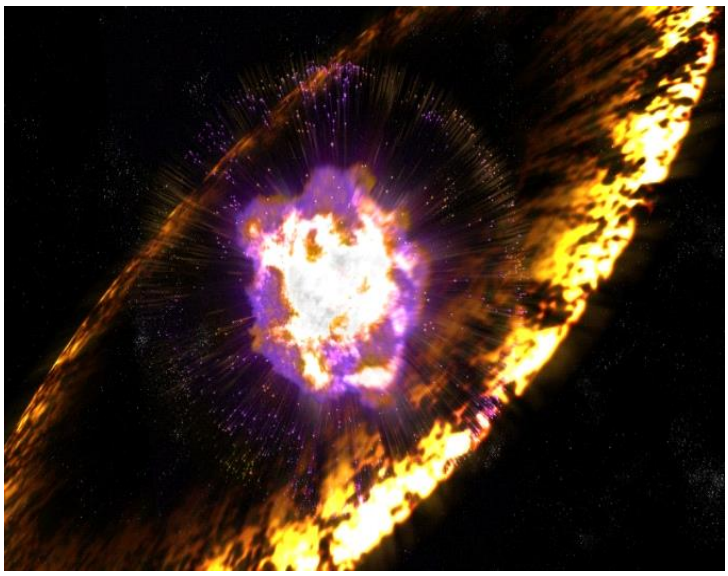

Figure 2.6: A star exploding sending off waves which accelerate protons to cosmic-ray energies through a process known as Fermi acceleration. Source: *http//www.kavlifoundation.org/science-spotlights/cosmic-rays-interview-stefan-funk*.

2.8 Transport of galactic cosmic rays

The motion of charged particles in the galaxy is governed by conditions such as the strength of the magnetic field and density of matter. These conditions often show strong fluctuations (*Stanev*, 2004). *Schlaepfer* (2003) stated that the elementary composition of galactic cosmic rays provides information about the nature of the source. The variation of the charge and mass composition with energy can be related to the acceleration process and to particle transport in the galaxy. Galactic cosmic rays have to travel through the galaxy, the heliosphere, the geomagnetic field, and the atmosphere of the earth before they can be detected on earth. The

next sections briefly describe the propagation of these particles from the galaxy to earth.

2.8.1 In the galaxy

Since our galaxy is strongly ionized, it has a high electric conductivity. This gives rise to the freezing-in-condition of the galactic magnetic field in the plasma. Hence, the galactic cosmic rays are guided by the galactic magnetic field and its fluctuations. It can be deduced from the gyration radius of the particles that the galactic magnetic field with its fluctuations will significantly scatter galactic cosmic-ray particles. Therefore, these particles remain confined in the galactic magnetic field to form an almost isotropic intensity inside the galaxy. *Fermi* (1949) suggested that galactic cosmic rays are accelerated primarily by bouncing back and forth along the galactic field between reflections from moving magnetic gas clouds. Hence, generally, the particles are believed to be accelerated by astrophysical sources, e.g. supernovae (*Blasi*, 2011), pulsars and pulsar wind nebulae (*Gaensler* and *Slane*, 2006).

2.8.2 In the heliosphere

Galactic cosmic rays that have successfully made their way through the galaxy encounter the heliosphere and enter it from all directions. Inside the heliosphere, they interact with the solar wind. During the interactions, they undergo processes which depend on solar activity that are discussed in section 4.1. The following sections describe the propagation of these particles through the geomagnetic field and the atmosphere of the earth before reaching the ground.

2.8.3 In the geomagnetic field

At earth level, cosmic rays are denied free access as they encounter the earth's magnetic field. This magnetic field, known as the geomagnetic field, is approximately represented by a magnetic dipole. Between the solar wind and the geomagnetic field, there is a boundary known as the magnetopause. The solar wind distorts the geomagnetic field into a teardrop shape, as shown in Figure 2.7, so that some field lines form a long tail behind the earth on the night side. The magnitude of this field is larger on the dayside. Since the solar wind changes are highly time-dependent, the changes in the geomagnetic field near the earth's surface are also time-dependent.

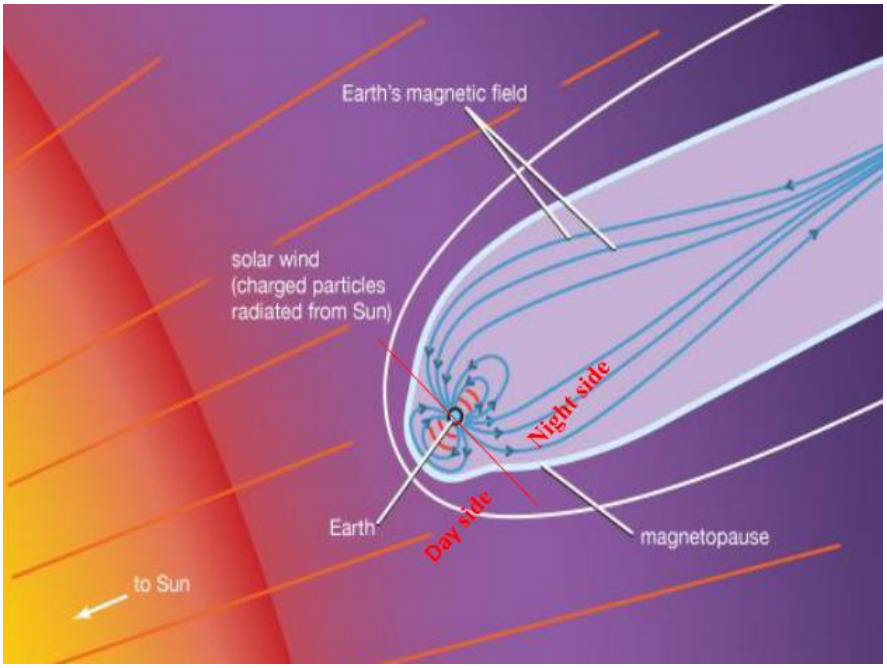

Figure 2.7: A two-dimensional cut through the geomagnetic field with the sun to the left. Source: *http //global.britannica.com/topic/space-weather*.

The direction of particles before entering the geomagnetic field is defined as their asymptotic direction of approach. The equation of motion for a

particle of charge q, under the action of the Lorentz force $\boldsymbol{F}$, moving with a velocity $\boldsymbol{v}$ in a uniform magnetic field $\boldsymbol{B}$ can be written as

$$\boldsymbol{F} = m\left(\frac{d\boldsymbol{v}}{dt}\right) = q\boldsymbol{v} \times \boldsymbol{B}, \tag{2.2}$$

where m is the mass of charged particles. This force causes charged particles to follow a curved trajectory, where the radius of curvature (or gyro-radius) is given as

$$r_{\mathrm{c}} = \frac{m\upsilon}{qB}\sin\delta, \tag{2.3}$$

where δ is the angle between $\boldsymbol{v}$ and $\boldsymbol{B}$. When $\delta = 90^{\circ}$, the curved trajectory becomes a circle with radius

$$r_{\mathrm{c}} = \frac{m\upsilon}{qB} = \frac{p}{qB}, \tag{2.4}$$

where p is the particle's relativistic momentum. In order for particles to penetrate the geomagnetic field, they must have a minimum rigidity. Generally, rigidity is defined as a measure of the momentum of the particle per elementary charge, i.e.

$$\mathrm{P} = \frac{pc}{q} = \frac{pc}{Ze}, \tag{2.5}$$

where Z represents the particle atomic number, e is the elementary charge of 1.602×10^{-19} C and c the speed of light. Now, the radius of curvature (equation 2.4) can be expressed in terms of the rigidity and the magnetic field as

$$r_{\mathrm{c}} = \frac{\mathrm{P}}{Bc}. \tag{2.6}$$

To express rigidity in terms of particle kinetic energy, the energy-momentum relationship

$$\mathrm{E}^2 = p^2c^2 + m_0^2c^4, \tag{2.7}$$

is used, where E is the total energy of particles per nucleon (i.e. kinetic energy per nucleon plus rest-mass energy per nucleon). According to Einstein's mass-energy equation, $\mathrm{E} = mc^2$ and $\mathrm{E}_0 = m_0c^2$ with m_0 the rest mass of the particles. Substituting $\mathrm{E} = mc^2$, $\mathrm{E}_0 = m_0c^2$ and equation 2.5 into equation 2.7, the relationship between rigidity, P, and the kinetic energy, T, is given as

$$\mathrm{P} = (A \,/\, Ze)(\mathrm{T}(\mathrm{T} + 2\mathrm{E}_0))^{1/2}, \tag{2.8}$$

where A is the mass number and E_0 is the particle rest-energy. Hence, a higher momentum particle will have a higher resistance to deflection by a geomagnetic field. Therefore, depending on their rigidities, these particles can be reflected back into space, trapped in the geomagnetic field or they can penetrate and make their way to the atmosphere of the earth. Figure 2.8 plots rigidity against kinetic energy per nucleon for protons and helium. It shows that the ratio (rigidity) of helium to proton is two at any kinetic energy. Therefore, this in turn tells us that the radius of curvature (equation 2.7) of helium is twice that of protons. This means that helium nuclei in space and in the geomagnetic field are less deflected by magnetic fields than protons.

Now, the minimum rigidity a charged particle can possess and still arrive at a specific point on the earth's surface from the top of the atmosphere is defined as the cutoff rigidity (*Shea et al.*, 1965). At earth, cutoff rigidity varies from 0 GV at the geomagnetic poles to about 17 GV in the equatorial regions. The vertical cutoff rigidity is the cutoff rigidity in the

direction radial from the earth centre. This vertical cutoff rigidity is given as

$$\mathrm{P_c} = \frac{M_m}{r_\oplus^2} \frac{\cos^4(\lambda)}{((1+\cos(\theta)\cos^3(\lambda))^{1/2}+1)^2}, \tag{2.9}$$

where M_m is the normalization magnetic dipole moment and $r_\oplus$ is the radius of the earth. The geographic latitude is represented by λ and θ represents the angle of arrival of cosmic rays. When $\theta = 0^\circ$ this means that cosmic-rays will arrive from the western horizon and when $\theta = 180^\circ$ they will arrive from the eastern horizon (*Shea* and *Smart*, 1970). In the case that $\theta = 90^\circ$ it means that they will arrive from any direction in the North (or South) vertical magnetic plane.

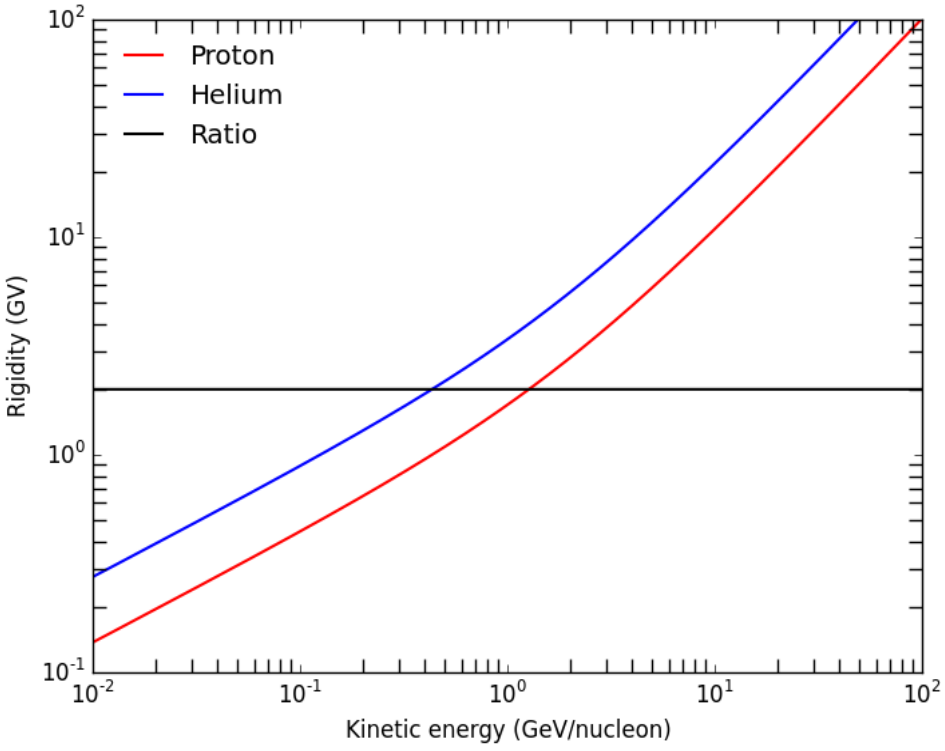

Figure 2.8: The relationship between rigidity and energy per nucleon as a function of A/Z given by equation 2.8. The red line represents protons, the blue represents helium and the black represents the ratio of helium to proton.

2.8.4 In the atmosphere

Before entering the atmosphere of the earth, cosmic rays are known as primary cosmic rays. These primary particles reach the atmosphere of the earth almost isotropically. When entering the atmosphere they interact with atmospheric nuclei, mainly nitrogen and oxygen molecules. These interactions create a cascade of secondary cosmic rays with lower energies than the primary cosmic rays.

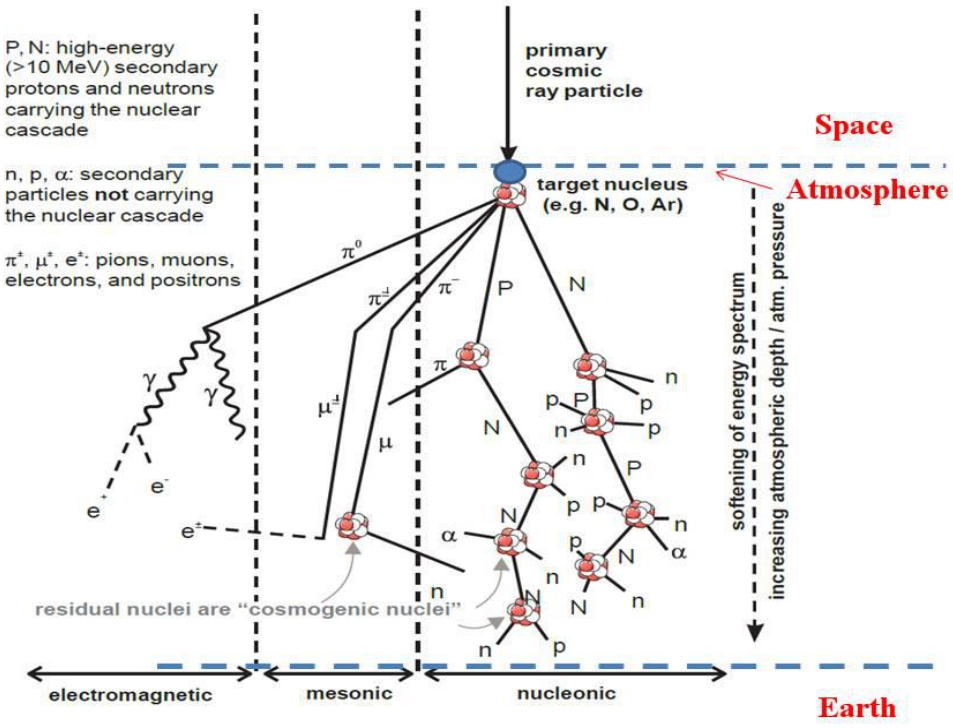

Figure 2.9: When Cosmic-rays enter the atmosphere of the earth, they collide with the nuclei of atmospheric molecules, forming a shower of secondary cosmic rays. The cascade consists of a nucleonic, a mesonic and an electromagnetic component. Source: *Dunai* (2010).

During the interactions, the production rate of these secondary cosmic rays depends strongly on atmospheric depth (or pressure variations and temperature effects), geomagnetic latitude and solar activity. The average propagation direction of secondary cosmic-ray particles is more or less the

same as the incidence direction of the primary particle. Secondary particles can be divided into three groups, as shown in Figure 2.9. The groups are

i) The nucleonic component (mainly protons and neutrons).

ii) The electromagnetic or soft component (mainly electrons, positrons, gamma rays).

iii) The hard component (mainly muons).

Among other produced secondary nuclear radionuclides important for studying modulation in the distant past, are ^{10}Be and ^{14}C. These radionuclides are stored in ice in polar regions and in tree rings, respectively (*Dunai*, 2010; *Steinhilber*, 2012; *Usoskin*, 2013). The only radionuclide discussed in this study is ^{10}Be. It is described in detail in section 3.6 when cosmic-ray archives and detectors are discussed. Therefore, in section 7.5 the importance of this radionuclide in the calculation of modulation intensities in the distant past is discussed.

2.9 Summary

In this chapter the basic background in order to understand modulation of cosmic rays in the heliosphere was given. This includes a description of the dynamic magnetic nature of the sun and the solar activity cycles. The formation of the heliosphere as a result of the solar wind blowing radially out from the sun into the entire region of space influenced by the sun and the heliospheric magnetic field was discussed. Illustration of how galactic cosmic rays propagate from the galaxy to earth was briefly discussed. This chapter concluded with a discussion of the production of secondary cosmic rays at earth.

Chapter 3

Cosmic-ray detectors and data archives

3.1 Introduction

Cosmic-rays can be measured with particle detectors in space or on earth. Primary cosmic-ray detection with sufficient statistics needs space-borne detectors, which can directly measure their energy in space. The energy of secondary cosmic rays decreases rapidly until they reach the earth's surface. Therefore, different detectors are needed to detect these particles. On the ground, the nucleonic component of secondary cosmic rays is detected using neutron monitors. Prior to neutron monitors, a wide range of detectors were used such as ionization chambers, Geiger-Müller counters and muon telescopes. Furthermore, radionuclides such as ^{10}Be produced from nucleonic component of secondary cosmic rays, is stored in ice. This can be used to study the behaviour of cosmic rays with solar activity, currently and over a period of several centuries.

In this chapter, a short introduction to cosmic-ray detectors, important in studying modulation in chapters 4, 5, 6 and 7, is given. This chapter starts with a discussion of the space missions, in particular IMP - 8, PAMELA and Voyager - 1. After this, ground-based detectors such as ionization chambers and neutron monitors are discussed. Following that, a discussion of cosmogenic radionuclides such as ^{10}Be is given, namely, on how the ^{10}Be is stored in ice, extracted and interpreted. After discussing these detectors, the concept of a differential response function is introduced. The chapter ends with a discussion of neutron monitor yield functions and a

short summary. In the next chapters, when the focus shifts to the modulation of cosmic rays, the concepts and nomenclatures introduced in this chapter are widely used.

3.2 Selected space missions

For more than fifty years now, a unique network of space-borne detectors located at various positions in the heliosphere measured (some are still measuring) intensity of cosmic rays. These detectors provide (d) data of energetic particles, plasma, and electric and magnetic fields. Space missions both in the inner and the outer heliosphere are of great importance in studying the global structure of the heliosphere and its constituents. In this chapter, a brief discussion on IMP - 8, PAMELA and Voyager - 1 missions is given.

3.2.1 The IMP - 8 mission

IMP - 8 carried instruments for top of the atmosphere studies, such as primary cosmic rays, plasmas, electric and magnetic fields. The objectives of the mission were to provide solar-wind parameters as input for magnetospheric and solar cycle variation studies. This satellite was the last one of the IMP series. It was launched on the 25^{th} of October 1973. The satellite was built and operated at Goddard and provided important space physics data as part of NASA's sun-earth connection research programme. It operated for 33 years until 7^{th} of October 2006. Its orbit around the earth was more elliptical than intended at a distance between 45 and 25 earth radii. Its orbital inclination varied between 0° and 55° with a periodicity of several years. The satellite spin axis was normal to the ecliptic plane, and the spin rate was 23 revolutions per minute (*http//nssdc.gsfc.nasa.gov/space/IMP - 8.html*). The most important

data from IMP - 8 used in this study are those of protons measured in 1987. Data measurements will be discussed in more detail in section 6.2.2.

3.2.2 PAMELA mission

PAMELA was developed to study mainly the antimatter component of the cosmic radiation at earth level (*Picozza et al.*, 2007). This instrument was kept inside a pressurised container attached to a Russian Resurs-DK1 earth-observation satellite which was launched into space by a Soyuz-U rocket from the Baikonur cosmodrome in Kazakhstan on the 15th of June 2006. This satellite orbited the earth in an elliptical quasi-polar orbit at altitudes ranging between 350 km and 600 km and with an inclination of 70° (*Picozza et al.*, 2007). In September 2010 the orbit was changed to a nearly circular one, at an altitude of 570 km and it has not changed since then. It also has a number of sub-detectors capable of detecting cosmic rays and providing accurate information about particle charge, mass, momentum and energy (or rigidity) range (*Casolino et al.*, 2008; *Adriani et al.*, 2014). For this study, the most important data from this satellite-borne experiment are protons measured in 2008. Data measurements will be discussed in more detail in section 6.2.3.

3.2.3 Voyager - 1 mission

NASA's twin spacecraft, Voyager - 1 and Voyager-2, were launched on the 5th of September 1977 and the 20th of August 1977, respectively. In December 2004, Voyager - 1 encountered the termination shock (*Stone et al.*, 2005; *Burlaga et al.*, 2008) at a distance of 94 AU. After passing through the termination shock, this spacecraft went to the inner heliosheath, the region of shocked solar wind between the termination shock and the heliopause. On the 25th of August 2012, Voyager - 1 crossed the heliopause and started sampling the LISM (*Krimigis et al.*, 2013;

Stone et al., 2013; *Krimigis et al.*, 2013; *Stone et al.*, 2013; *Webber* and *McDonald*, 2013; *Webber* and *Intriligator*, 2014 and *Senanayake et al.*, 2015). The proton data detected in 2012 by this spacecraft are discussed in more detail in section 6.2.1, particularly in the determination of the local interstellar spectrum (LIS) intensities and the modulation parameter used in this study. According to NASA, Voyager - 1 has enough electrical power and fuel to operate and send back data until 2020, at least (*http//Voyager.jpl.nasa.gov/mission/ interstellar.html*).

3.3 Ground-based detectors

In this section, relevant ground-based detectors for the secondary cosmic rays relevant to this study are discussed.

3.3.1 Ionization chambers

In his quest to study cosmic radiation, Hess used an air-tight ionization chamber measuring the rate of discharge of electrified fibre in the chamber during his balloon flights in 1911. Since then, a continuous recording of cosmic rays using ground-based detectors such as ionization chambers started (*Simpson*, 1990). For studying the geographic dependence of cosmic-ray time variations in detail, a standardized ionization chamber was designed for world-wide distribution. The first routine monitoring of cosmic rays was initiated in 1930 by Compton and Bennett of the University of Chicago, and Sterns of the University of Denver. This resulted in the construction of a special precision ionization chamber (*Compton et al.*, 1934). Seven of these chambers were installed as part of the first world-wide network of cosmic-ray stations. Between 1949 and 1953, this network of ionization chambers was significantly extended by the former Union of Soviet Socialist Republics. In these early

measurements, pressure and temperature variations in the atmosphere of the earth obstructed the recognition of variations of secondary cosmic rays. Papers by *Forbush* (1938, 1946) provided the first convincing evidence for intensity variations that were due to other effects than atmospheric (*Simpson*, 1990). This programme was operated continuously for more than three solar activity cycles (*Dorman*, 2004).

In the 1920s, ionization chambers were very large and expensive. According to *Shea* and *Smart* (2000), ionization chambers measured only secondary cosmic rays produced by protons with energies larger than 4 GeV per nucleon. Further, *Simpson* (1948) discovered that the latitude variation of the intensity of evaporating neutrons in the atmosphere is several times larger than that of the hard component. Hence, Simpson noted that these measurements have to be corrected for variations in atmospheric pressure and the production heights in the atmosphere. According to *Forbush* (1954); *Shea* and *Smart* (2000) and *McCraken* and *Beer* (2007), the radioactive contamination of the chamber itself and its surroundings was difficult to account for. However, it is important to recover these data series to construct the long-term behaviour of cosmic-ray variation in the distant past. Retrieving this historical data are not that simple and often yields misleading results when these data points are used to reconstruct the distant past cosmic-ray record, according to *McCraken* and *Beer* (2007).

Furthermore, the statistical accuracy of the chambers' count rate was low. Hence, in the early 1940s, Geiger-Müller counters, together with muon telescopes operated from 1940 to 1946, were also used to monitor secondary cosmic rays (*Dorman*, 1974). In the early 1950s a new type of detector was developed by Simpson, described in the next section, which can record secondary cosmic rays created by incident primary cosmic rays

with lower energy, and which was relatively easy to maintain. This device is universally known as a neutron monitor (*Simpson*, 2000).

3.3.2 Neutron monitors

The nucleonic component of secondary cosmic rays is produced when primary cosmic rays experience multiple interactions with the atmosphere of the earth, as discussed in section 2.8.4. Simpson selected in his original design (see Figure 3.1) of a neutron monitor five main parts, i.e.

i) **The reflector:**

This is the outer part that consists of a material that contains hydrogen, like paraffin wax or polyethylene. A reflector reflects unwanted low energy neutrons coming from the surroundings while the low-energy neutrons created in the lead-ring producers are kept in.

ii) **The lead-ring producers:**

Inside the reflector there is a lead-ring producer which consists of several lead rings and is the heaviest component of a neutron monitor. Fast neutrons that travel through the reflector interact with the lead to produce lower energy neutrons.

iii) **The moderator:**

Inside the lead-ring producers, there is a moderator that thermalizes or moderates the lower energy neutrons created in the lead-ring producer. The inner moderator consists of a high-density natural polyethylene pipe or paraffin wax. The function of the moderator is to decrease the energies of the neutrons through elastic collisions and brings them as close to thermal energies (about 0.025 eV) as possible.

iv) **Detector tube:**

Inside the moderator, a gas-filled proportional counter is used to detect mainly neutrons. This is the "heart" of a neutron monitor.

After neutrons are created by the lead producers and slowed down by moderators, they can encounter a nucleus in the gas tube and cause it to disintegrate. This nuclear reaction produces energetic charged particles that ionize the gas in the detector tube, producing an electrical signal. The exothermic reaction for counting neutrons with a $^{10}BF_3$ counter is

$$^{10}BF_3 + {}^1n \rightarrow {}^7Li + {}^4He + \text{energy}. \tag{3.1}$$

From 1990, counter tubes filled with ^{3}He gas instead of $^{10}BF_3$ gas were also used in neutron monitors. According to *Stoker et al.* (2000), the ^{3}He detector tube has a much higher efficiency per unit volume compared with the large $^{10}BF_3$ detector tube. The exothermic reaction in a ^{3}He counter is

$$^3He_2 + {}^1n \rightarrow {}^3H_1 + \text{proton}. \tag{3.2}$$

v) **Detector electronics:**

The detector tubes are connected to detector electronics. This passes electronic signal information to a storage system, which records counts, pressure, high voltage and temperature.

For more information about the neutron monitor designs, see *Stoker et al.* (2000) or visit the website *http //www.nmdb.eu/*.

Since they were invented, there have been a number of neutron monitors of different types operating continuously at various positions, forming a global neutron monitor network covering a wide range of cutoff rigidities. The most notable are the β-IGY-type, β-NM64-type and β-NMD-type. Here β denotes the number of counter tubes. The IGY neutron monitors were deployed in a worldwide network during the International Geophysical Year in 1957 (*Simpson*, 1957). The 6-NM64 neutron monitor type was designed by Carmichael for deployment in time for the

International Quiet Sun Year in 1964. These neutron monitors are known as "super" neutron monitors. *Hatton* and *Carmichael* (1964) studied comprehensively the experimental design of the β-NM64-type. The detection efficiency for the β-IGY-type is 1.9 % and 5.7 % for the β-NM64-type. The β-NMD-type is known as the neutron moderated detector and it has no lead producer. This detector is more sensitive to low rigidity neutrons close to 1 GV than the β-NM64-type (*Stoker et al.*, 1979; *Balabin et al.*, 2008).

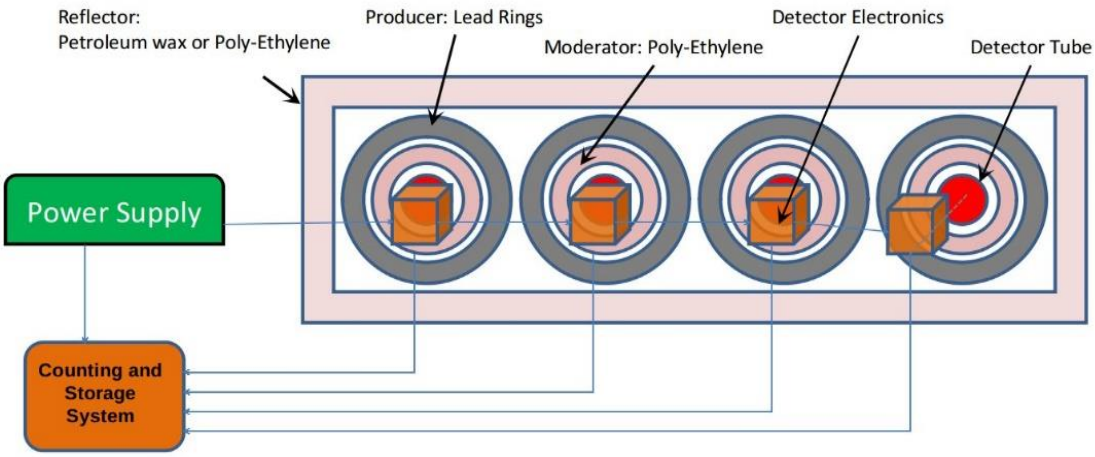

Figure 3.1: This is an artist's illustration showing a basic neutron monitor lay-out.

The count rate of a neutron monitor is sensitive to atmospheric pressure. Therefore, corrections of the pressure variations are very important. Atmospheric pressure effects are discussed by *Hatton* and *Griffiths* (1968). The atmospheric pressures used in this study are annual averages. The detection efficiency of every monitor differs due to its design and the environment. Furthermore, the count rate varies with geographic latitude and longitude, cutoff rigidity and altitude.

3.3.3 The selected neutron monitors

The four neutron monitors selected in this study are operated by the Centre for Space Research at the Potchefstroom campus of the North-West University (NWU) and are listed below:

i) **The Hermanus neutron monitor:**

The monitor consists of 12 counter tubes of the NM64-type. It operates in Hermanus, a town at sea level close to the southern tip of Africa. The neutron monitor has been in operation since the International Geophysical Year (IGY), from July 1957. This monitor is the oldest continuously operating neutron monitor in the world.

ii) **The Tsumeb neutron monitor:**

This 18-NM64 operates at a research station that was established by the Max Planck Institute for Aeronomy in 1957 for ionospheric measurements during the IGY. Presently, the station is maintained by the Geological Survey of Namibia. The station is situated about 12 kilometres north-west from the town Tsumeb, in the northern part of Namibia.

iii) **The SANAE neutron monitors:**

Since April 1997, the 6-NM64 has operated in Antarctica on Vesleskarvet, a small outcrop (nunatak). This base is 170 km inland from the former South African bases. The old SANAE neutron monitor used before 1994 was a 3-NM64 and it was built on the ice shelf. This monitor operated from 1964 to 1994. The neutron moderated detector (4-NMD) at SANAE is not used in this study. The data gap between December 1994 and April 1997 for both monitors is due to the move and re-construction of the base from the ice shelf to solid rock at Vesleskarvet.

iv) **The Potchefstroom neutron monitor:**

Since 1971, the monitor has consisted of 15 counters of the IGY-type. The monitor is situated on the roof of the physics building of the Potchefstroom campus of the NWU. This centre is

responsible for processing of data recorded by all these above-mentioned neutron monitors.

Data of all these neutron monitors can be accessed through the online NWU webpage. The monitors' information is summarized in Table 3.1 (*http//www.nwu.ac.za/neutron-monitor*).

Table 3.1: List of neutron monitors used in this study.

Station	Type	Altitude (m)	P_c (GV)	Average atmospheric pressure (mm Hg)
SANAE	6-NM64	856	0.8	660
Hermanus	12-NM64	26	4.9	760
Potchefstroom	15-IGY	1351	7.2	652.4
Tsumeb	18-NM64	1240	9.2	660

3.4 Cosmogenic radionuclide archives

Prior to the 1930s, no direct primary (or secondary) cosmic-ray measurements existed. Cosmogenic radionuclide can be used to describe solar activity. In this framework, the most commonly used radionuclide isotope is ^{10}Be. As mentioned in section 2.8.4, ^{10}Be is produced in the atmosphere of the earth by nuclear reactions of primary cosmic rays with atmospheric nitrogen and oxygen. ^{10}Be is removed from the atmosphere of the earth relatively fast within a few years and precipitated into the snow in polar regions. Therefore, this ^{10}Be radionuclide gets compacted into natural archives such as polar ice sheets. ^{10}Be can only exist in ice sheets because if it falls on the soil (or water) it disappears. These cosmogenic radionuclides have a half-life of about 1.5×10^9 years. *Korschinek et al.* (2010) and *Chmeleff et al.* (2010) recently corrected the ^{10}Be half-life to $(1.387 \pm 0.012)\times10^6$ years.

There are several ice cores where ^{10}Be has been sampled. The Greenland ice cores are in North GRIP, Dye3 and Milcent. Sites in Antarctica include Dome Fuji and South Pole. Figure 3.2 shows how ice is extracted from the ground by a drilling machine. This ice consists of several layers. Each layer of ice represents a year with a certain ^{10}Be concentration. The length of the record depends on the depth of the ice core, i.e. the deeper the core the more the layers from the ice can be accumulated and this in turn can be used to calculate the level of ^{10}Be concentration as a function of time.

The time resolution (i.e. the shortest time which can be correctly differentiated) depends on the amount of annual snowfall. ^{10}Be samples extracted are prepared chemically (*Steinhilber et al.*, 2012). First, the ice is cut into small samples of several lengths corresponding to an average time resolution in years. Then it is melted and mixed with a (^{9}Be) carrier. Later, it is passed through a cation ion exchange resin. The samples of concentrated ^{10}Be are then analyzed by using accelerator mass-spectrometry (AMS) at the facility of the Ion Beam physics group at the Swiss Federal Institute of Technology in Zürich, Switzerland. The typical AMS uncertainty is about 5 %. Uncertainties are introduced mainly due to atmospheric mixing processes and wet and dry deposition from the atmosphere of the earth to the ice (*Steinhilber et al.*, 2012).

However, *McCracken* and *Beer* (2007) pointed out that the sampling of several more ice cores at annual intervals is clearly desirable to assess such system errors. A problem is that computation of the ^{10}Be concentration differs because different normalization methods are used for different ^{10}Be samples. For reviews on ^{10}Be and chemical preparation of samples from the ice core, see studies by *Yiou et al.* (1997); *Muscheler et al.* (2004); *Dunai* (2010) and *Steinhilber et al.* (2012).

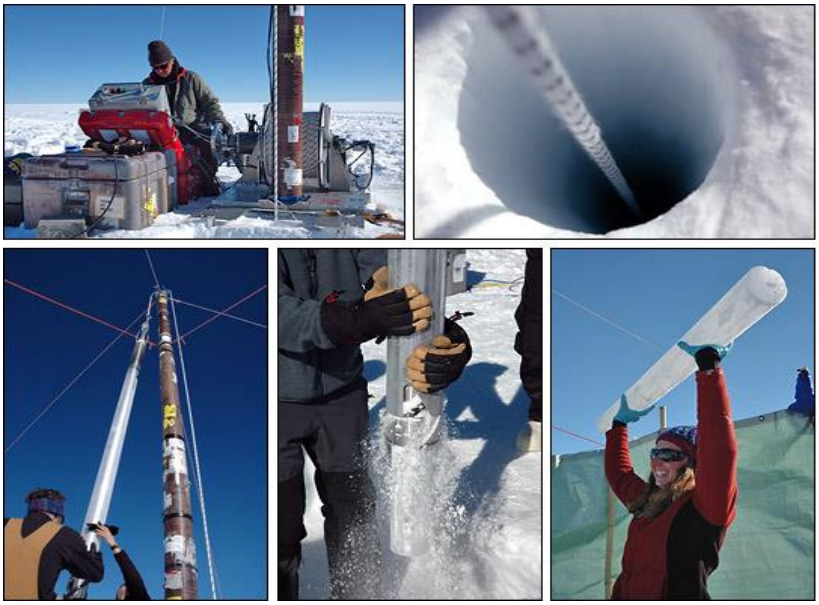

Figure 3.2: Illustrating the extraction of ^{10}Be concentration in ice. A small drilling system used to recover a short core in Antarctica is shown. The ice core was then protected against contamination and, following sample preparation, analyzed using an accelerometer mass spectrometer. Source: *http//earthobservatory.nasa.gov/Features/Paleoclimatology_IceCores/*.

3.5 Neutron monitor differential response function

The concept of response functions was introduced by *Fonger* (1953); *Dorman* (1957) and *Brown* (1957). To completely understand this concept, knowledge of the geomagnetic and atmospheric particle transport of secondary cosmic rays is required. Since the 1930s, various surveys have been conducted to investigate the latitudinal dependence of cosmic-ray count rates.

Differentiating the count rate with respect to cutoff rigidity yields the differential response function. These differential response functions are cutoff rigidity spectra of secondary cosmic rays inside the atmosphere of the earth. For this study, the latitude surveys that were conducted by the previously known Potchefstroom University which is now known as the NWU (Centre for Space Research, Potchefstroom campus) during the

solar minimum of 1986/7 were used. The primary purpose of this survey was to study the neutron monitor response function as derived from the latitudinal dependence (*Moraal et al.*, 1989). *Moraal et al.* (1989) used a parameterized function to study the relationship between the measured count rates of neutron monitors, $N(\mathrm{P_c},\, x,\, t)$, and cutoff rigidity. This function is known as the Dorman function (*Dorman et al.*, 1970), and is given by

$$N(\mathrm{P_c},\, x,\, t) = N_0(1 - \exp(-\alpha \mathrm{P_c}^{-k})), \tag{3.3}$$

where x is the atmospheric depth (or pressure) and $\mathrm{P_c}$ is the cutoff rigidity of a detector at time t. To fit the measured count rates from the survey, *Moraal et al.* (1989) used parameters, $\alpha = 10.068$, $k = 0.952$ and the normalization constant $N_0 = 1.0$. Figure 3.3 shows the normalized count rates recorded during the survey as a function of cutoff rigidity. The red squares represent the measured count rates at a specific cutoff rigidity and the solid red line represents equation 3.3.

Differentiating the Dorman function (equation 3.3) gives

$$-\frac{dN(\mathrm{P_c},\, x,\, t)}{d\mathrm{P_c}} = \alpha k N_0 \exp(-\alpha \mathrm{P_c}^{-k}) \mathrm{P_c}^{-k-1}. \tag{3.4}$$

According to *Caballero-Lopez* and *Moraal* (2012), equation 3.4 is known as the differential count rate of a neutron monitor and the differential response function is $-d \ln N(\mathrm{P_c},\, x,\, t) \,/\, d\mathrm{P_c}$. However, in this study equation 3.4 is used to represent the differential response function.

Figure 3.4 shows the differential response function on a log-log scale calculated from equation 3.4. The maximum value of this differential response function is 4.72 %/GV calculated with parameters $\alpha = 10.068$, $k = 0.952$ and $N_0 = 100$ %.

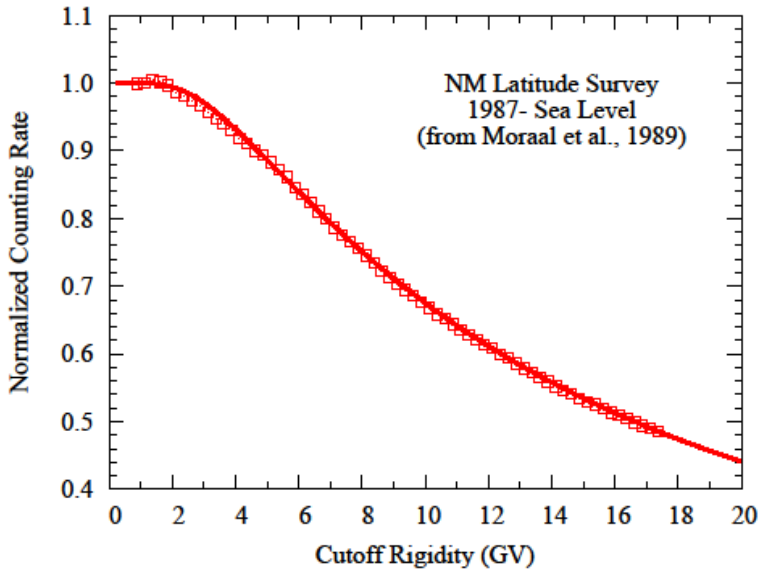

Figure 3.3: Hourly count rates from sea-borne surveys obtained at different cutoff rigidities. Source: *Moraal et al.* (1989).

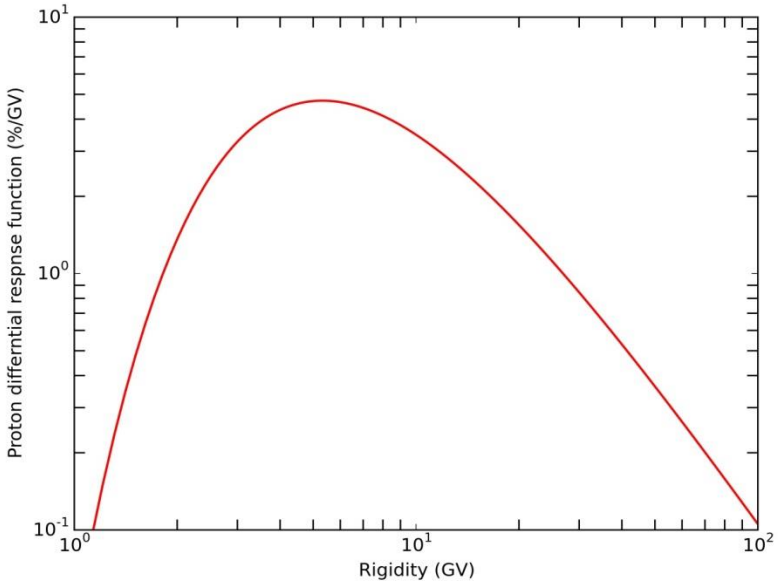

Figure 3.4: A differential response function, given by equation 3.4, calculated from the 1986/7 latitude survey, conducted by *Moraal et al.* (1989).

3.6 The neutron monitor yield function

The yield function is the number of secondary cosmic rays detected by a neutron monitor per primary particle penetrating the top of the

atmosphere of the earth. The relation between the response function inside the atmosphere of the earth, $-dN(\mathrm{P},\, x,\, t)\,/\,d\mathrm{P}$, and the intensity spectrum of primary cosmic rays above the atmosphere, $j_i(r,\, \mathrm{P},\, t)$, is given as

$$\mathrm{S}_i(x,\ \mathrm{P}) = -\frac{dN(\mathrm{P},\, x,\ t)}{d\mathrm{P}} \Big/ j_i(r,\, \mathrm{P},\, t), \tag{3.5}$$

where $\mathrm{S}_i(x,\ \mathrm{P})$ is the atmospheric yield function and i represents various particle species. According to *Caballero-Lopez* and *Moraal* (2012), in order to calculate an accurate neutron monitor yield function, it is important that the measurements in space and inside the atmosphere must be taken at the same time, or at least during times when the intensity levels of cosmic rays are comparable.

Basically, there are three methods of determining a neutron monitor yield function, i.e. (1) parameterization of latitude survey measurements, (2) theoretical calculation and (3) Monte Carlo simulation of cosmic ray transport through the atmosphere and the neutron monitor. The parameterization method is by far the most used. In this study, the double power law yield function parameterization is adopted from *Caballero-Lopez* and *Moraal* (2012). This yield function was calculated from the proton intensities measured by PAMELA in 2008, and IMP - 8 in 1987. The *Caballero-Lopez* and *Moraal* (2012) double power law neutron monitor yield function parameterization for protons is given as

$$\mathrm{S}_i^{\mathrm{Proton}}(x,\ \mathrm{P}) = \mathrm{S}_0(\mathrm{P}_0^a + \mathrm{P}^a)^{(\gamma_1-\gamma_2)/a}\mathrm{P}^{\gamma_2}, \tag{3.6}$$

where S_0, P_0, a, γ_1 and γ_2 are constants. According to *Caballero-Lopez* (2016), these authors made a misprint in their published yield function constants. Therefore, in this study the correct parameters publisehed by *Caballero-Lopez* (2016) which appear in Table 2 as cab12 are used. These

set of parameters are given as $S_0 = 4.37 \times 10^{-4}$, $P_0 = 0.089$ GV, $a = 0.9$, $\gamma_1 = 0.748$ and $\gamma_2 = 61.3$.

Figure 3.5 shows the yield function from *Clem* and *Dorman* (2000) (blue line is denoted by CD00) and that of *Caballero-Lopez* and *Moraal* (2012) (red line is denoted by CM12) with the new constants adopted from *Caballero-Lopez* (2016). At about 30 GV the CM12 yield function is essentially the same as that of CD00. However, below 30 GV the CM12 yield function is significantly lower than that of CD00.

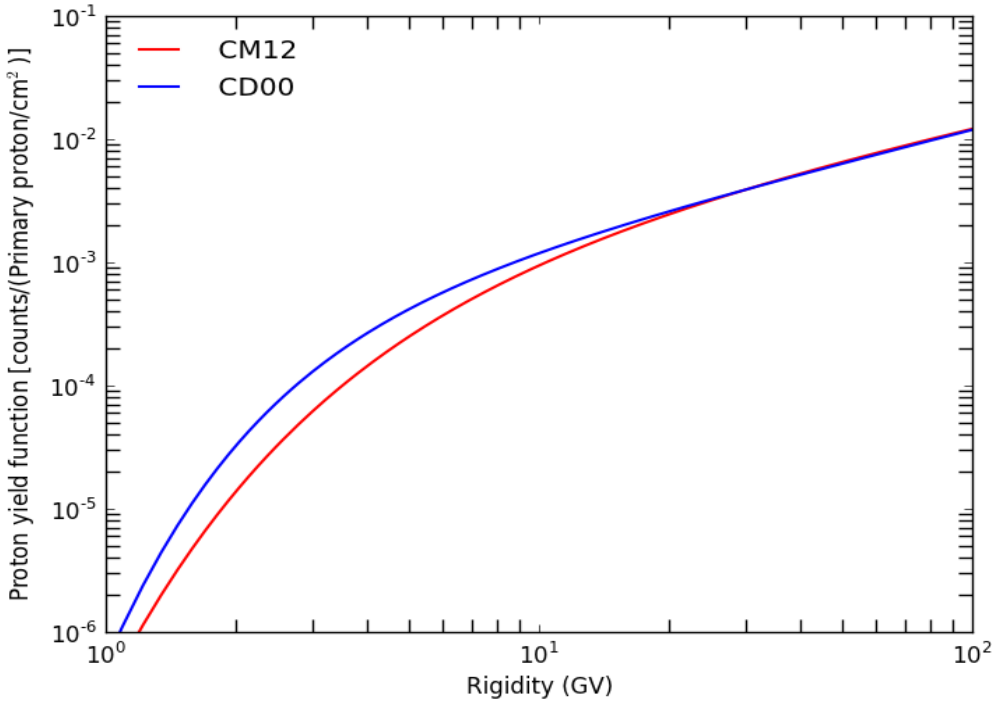

Figure 3.5: The neutron monitor yield function by *Caballero-Lopez* and *Moraal* (2012) (red line) and *Clem* and *Dorman* (2000) (blue line).

3.7 Summary

This chapter discussed the space-borne detector missions, ground-based detectors and the cosmogenic radionuclides most relevant to this study. The missions most relevant to this study are IMP – 8, PAMELA and

Voyager – 1. The four neutron monitors operated by NWU were discussed as well as ionization chambers and the ^{10}Be radionuclide. This chapter concluded with a discussion of the neutron monitor yield function, following the introduction of the concept of a differential response function.

Chapter 4

Modulation of cosmic rays and approximate solutions of the full Parker transport equation

4.1 Introduction

Inside the heliosphere, cosmic-ray intensities continuously change due to the radially expanding solar wind and the heliospheric magnetic field embedded on the sun's surface. This phenomenon is known as modulation of cosmic rays. Measurements recorded by various particle detectors have shown and confirmed that the count rates of secondary cosmic rays measured on earth and the intensity of primary cosmic rays in space varies with time, position and rigidity (or energy). Cosmic-ray modulation can be classified according to the time scale for a process, as short-term, medium-term, and long-term.

Short-term modulation of cosmic rays was discovered in the late 1930s and these times range from minutes to several hours, e.g. Forbush decreases (*Forbush*, 1946). Medium-term times range from days to about a month (sometimes more than a month), e.g. the 27-day rotation time of the sun (*Alania et al.*, 2011). The long-term modulation of cosmic rays ranges over a period of time longer than a month to years (or decades and even beyond), e.g. the 11-year and 22-year cycles (detailed in section 4.2). The space-borne and ground-based detectors show the same long-term variation pattern. Only long-term modulation is considered in this study.

The modulation processes experienced by cosmic rays in the heliosphere are combined in the full Parker transport equation. This equation was first derived in 1965 by Eugene Parker and therefore it was named after him. Because of the complexity of the full Parker transport equation with a realistic diffusion tensor, modulation studies in the heliosphere are done with various approximate solutions to simplify it, i.e. the Convection-Diffusion and the Force-Field approximations.

In this study, the modulation parameters are described by the modulation parameter $\phi(r, t)$ (calculated from the Force-Field approximation) and the modulation function $M(r, t)$ (calculated from the Convection-Diffusion approximation). In this chapter, the focus is on discussing the long-term modulation of cosmic rays and the full Parker transport equation that describes it. Further sections describe the key components of the modulation parameters of the full Parker transport equation. At the end of the chapter, a brief summary is given. The concepts and nomenclatures introduced in this chapter are important for the subsequent chapters.

4.2 Count rates of neutron monitors and modulation of cosmic rays

The neutron monitors located on the earth's surface have been used over the last decades to study the behaviour of secondary cosmic rays. Figure 4.1 panel (a) shows the mean monthly measurements of the four neutron monitors of NWU mentioned in section 3.3.3. The count rates of these neutron monitors are normalized to 100 % in March 1987 and plotted as a function of time. Count rates for the three stations were shifted by the values shown in the graph, to easily distinguish among the four stations because they have similar count rates. Note that SANAE count

rates show a gap between December 1994 and April 1997. That was because the monitor was not operating in those years due to the building of the new SANAE base, as mentioned in section 3.3.3.

Figure 4.1 panel (b) shows the sunspot numbers, representing the level of solar activity, plotted as a function of time. Panels (a) and (b) of Figure 4.1 show an anti-correlation between the intensities of secondary cosmic rays at earth and solar activity, i.e. the 11-year solar cycles. This periodicity in sunspot number records is named for Schwabe (*Schwabe*, 1843), who was the first person to describe this cycle. All neutron monitors show these 11-year cycles.

In Figure 4.1, neutron monitor normalized measurements show that higher count rates are observed during solar minimum conditions and low count rates during times of solar maximum. The solid silver vertical lines on the figure indicate the years of cosmic-ray minima. During solar activity minima, count rates of neutron monitors showed three peaks in 1965, 1987, 2009 and two plateaus in 1976 and 1998. The rise and fall in sunspot numbers from solar minimum to solar maximum and back to solar minimum occur every 11-years to complete one cycle. The peaks in the count rates of neutron monitors occur after 22-years, i.e. from 1965 and 1987 or 1987 and 2009. This so-called 22-year cycle in the count rates of neutron monitors is thus clearly visible on the figure with its peaks and plateaus alternating. This alternating peaks and plateaus pattern is caused by different drift fields in the heliospheric magnetic field, as mentioned by *Jokipii et al.* (1977); *Potgieter* (1985a; 1985b); *Potgieter* and *Moraal* (1985); *Engelbrecht* (2008) and *Potgieter* (2013).

The recent 2009 solar minimum record of detected cosmic rays worldwide was significantly higher than that of March 1987. Also, solar minimum

conditions unexpectedly continued for several months when compared with previous ones.

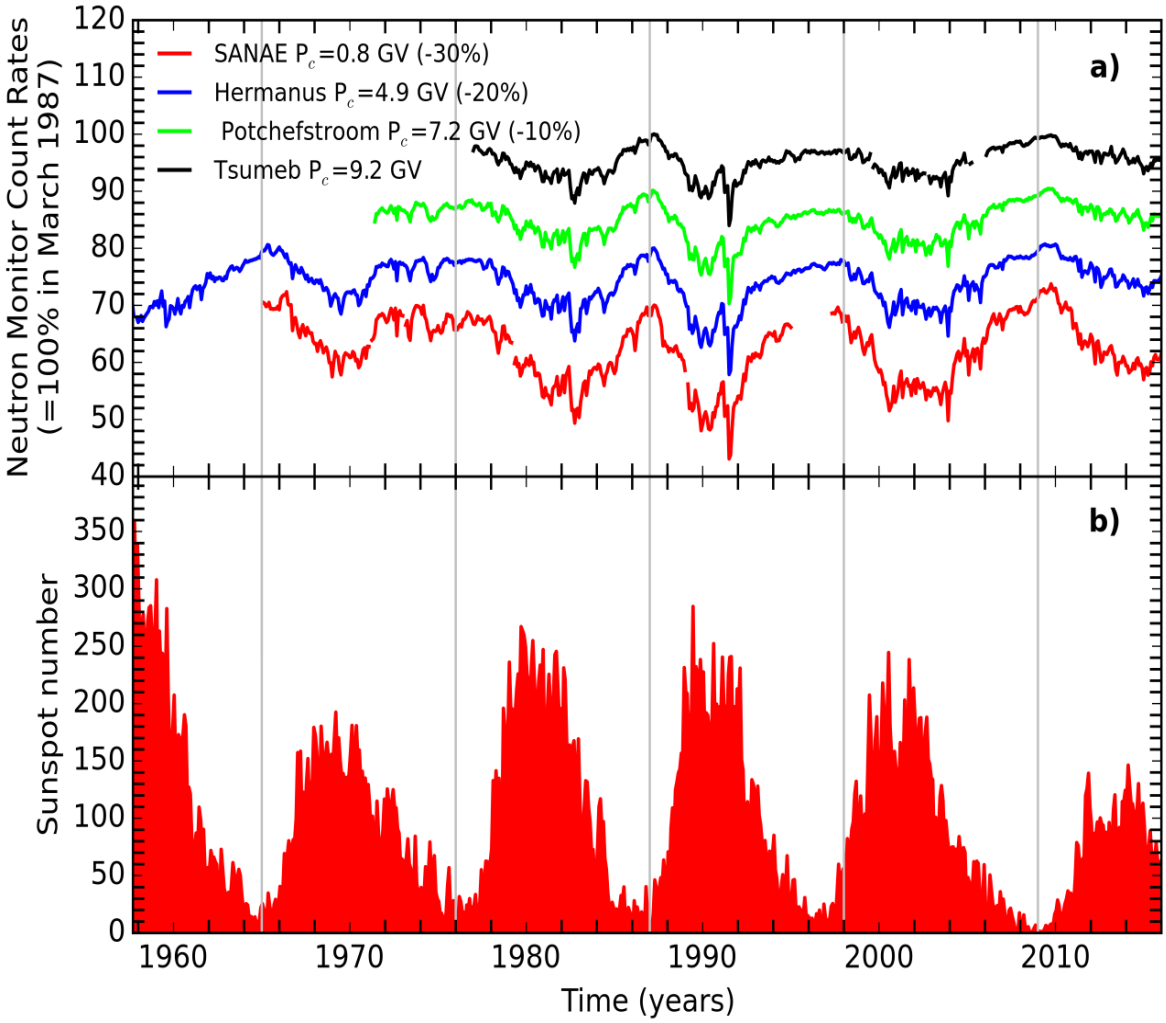

Figure 4.1: The mean-monthly count rates of the four neutron monitors operated by NWU (normalized to 100 % in March 1987) as a function of time together with the sunspot numbers, from July 1957 to October 2016. The solid silver vertical lines on the figure indicate the times of cosmic-ray minima. The sunspot numbers anti-correlates with the count rates of neutron monitors. Data source of neutron monitors is *http//www.nwu.ac.za/neutron-monitor-data* and the sunspot data source is *ftp//ftp.ngdc.noaa.gov*.

Secondary cosmic rays at earth react to modulation based on cutoff rigidity. For that reason, a monitor having a lower cutoff rigidity will be

more sensitive to modulation of cosmic rays compared with monitors having higher cutoff rigidity. Evidently, during this 2009 solar minimum, not all neutron monitors recorded higher values than the March 1987 solar minimum. The neutron monitors with high cutoff rigidity in this study (e.g. Tsumeb, $P_c = 9.2$ GV) showed that its count rate has decreased compared with the March 1987 solar minimum count rate. In contrast, the one with low cutoff rigidity (e.g. SANAE, $P_c = 0.8$ GV) has significantly increased count rates compared with the March 1987 solar minimum.

4.3 The Parker transport equation

The modulation processes of cosmic rays in the heliosphere are combined in the Parker transport equation (*Parker*, 1965). Later, this equation was derived once more by *Gleeson* and *Axford* (1967) and then simplified by *Gleeson* and *Axford* (1968a); *Gleeson* and *Urch* (1968); *Jokipii* and *Parker* (1970) and *Gleeson* and *Urch* (1973). This equation originates from the continuity equation, as discussed in detail by *Potgieter* (1998) and *Moraal* (2011). In the heliosphere, the full Parker transport equation involves four major processes:

i) Convection due to the radially expanding solar wind.

ii) Diffusion along and across the heliospheric magnetic field.

iii) Energy changes like adiabatic cooling (or heating).

iv) Drift effects, due to the gradient and curvatures of the heliospheric magnetic field.

As stated by *Caballero-Lopez* and *Moraal* (2004) and *Moraal* (2011), the full Parker transport equation has three forms and all these forms are equivalent, i.e.

$$\frac{\partial f}{\partial t} + \boldsymbol{\nabla} \cdot (\mathrm{V}(r) f - \mathbf{K} \cdot \boldsymbol{\nabla} f) - \frac{1}{3p^2} (\boldsymbol{\nabla} \cdot \mathrm{V}(r)) \frac{\partial}{\partial p} (p^3 f) = Q, \qquad (4.1)$$

$$\frac{\partial f}{\partial t} + \boldsymbol{\nabla} \cdot (\mathrm{C}\mathrm{V}(r) f - \mathbf{K} \cdot \boldsymbol{\nabla} f) + \frac{1}{3p^2} \frac{\partial}{\partial p} (p^3 \mathrm{V}(r) \cdot \boldsymbol{\nabla} f) = Q, \qquad (4.2)$$

$$\frac{\partial f}{\partial t} + \mathrm{V}(r) \cdot \boldsymbol{\nabla} f - \boldsymbol{\nabla} \cdot (\mathbf{K} \cdot \boldsymbol{\nabla} f)) - \frac{1}{3} (\boldsymbol{\nabla} \cdot \mathrm{V}(r)) \frac{\partial f}{\partial \ln p} = Q, \qquad (4.3)$$

where $f = f(r,\, p,\, t)$ describes the cosmic-ray distribution function, r is the heliocentric radial distance from the sun, p is the particle momentum and t represents time. The diffusion tensor is $\mathbf{K} = \mathbf{K}(r,\, \mathrm{P},\, t)$, the solar wind speed is $\mathrm{V}(r)$ and Q is a possible source of cosmic rays inside the heliosphere. The 'C' in equation 4.2 is the Compton-Getting coefficient. Although the full Parker transport equation is written in terms of momentum, it is usually solved in terms of rigidity. Therefore, henceforth all momentum terms will be replaced by rigidity terms. This equation cannot be solved analytically due to its complexity and the solution describing it is not exact but instead it is an estimate. Many approximate solutions of the full Parker transport equation were proposed over the years and all of them have some shortcomings. In sections 4.5 and 4.8, a detailed description of two approximate solutions in the order of their complexity is given.

4.4 The cosmic-ray convection and diffusion process

The Parker transport equation diffusion term

In the full Parker equation, the term $\boldsymbol{\nabla} \cdot (\mathbf{K}(r,\, \mathrm{P},\, t) \cdot \boldsymbol{\nabla} f(r,\, \mathrm{P},\, t))$ represents diffusion. This diffusion term describes cosmic rays diffusing inwards in a spherically symmetrical heliosphere as they scatter off the fluctuations in the heliospheric magnetic field. Once cosmic rays are inside the heliosphere, an interior radial diffusive intensity is created. The cosmic-ray intensity diffusion tensor $\mathbf{K}(r,\, \mathrm{P},\, t)$ specifies the scattering

properties of the heliospheric magnetic field. In the full Parker transport equation it has the form

$$\mathbf{K}(r,\,\mathrm{P},\,t) = \begin{pmatrix} \kappa_{\parallel} & 0 & 0 \\ 0 & \kappa_{\perp\theta} & \kappa_{d} \\ 0 & -\kappa_{d} & \kappa_{\perp r} \end{pmatrix}, \tag{4.4}$$

where $\kappa_{\parallel}$ denotes the diffusion coefficient parallel and $\kappa_{\perp\theta}$ denotes the diffusion coefficient perpendicular to the mean heliospheric magnetic field in the direction away from the poles of the sun. $\kappa_{\perp r}$ denotes the diffusion coefficient perpendicular to the mean heliospheric magnetic field in the r radial/azimuthal direction. The element κ_{d} describes the gradient, curvature and heliospheric current sheet drifts of cosmic-rays in the background heliospheric magnetic field (*Scherer et al.*, 2006). For a more detailed overview about diffusion coefficients, see e.g. *Burger et al.* (2000); *Teufel* and *Schlickeiser* (2002); *Engelbrecht* (2008); *Effenberger et al.* (2012); *Potgieter* (2013) and *Manuel* (2013).

In order to calculate a simple expression describing cosmic-ray diffusion in a spherically symmetrical heliosphere, the diffusion tensor $\mathbf{K}(r,\,\mathrm{P},\,t)$ is assumed to collapse into a single radial diffusion coefficient, $\kappa_{rr}(r,\,\mathrm{P},\,t)$. This diffusion coefficient is expressed as

$$\kappa_{rr}(r,\,\mathrm{P},\,t) = \kappa_{\parallel}(r,\,\mathrm{P},\,t)\cos^{2}\psi + \kappa_{\perp}(r,\,\mathrm{P},\,t)\sin^{2}\psi, \tag{4.5}$$

in units of $\mathrm{cm}^{2}\,\mathrm{s}^{-1}$. Here, ψ is the spiral angle between the background magnetic field and the radial direction. The diffusion coefficient $\kappa_{\perp}$ dominates κ_{rr} in the outer heliosphere, while $\kappa_{\parallel}$ dominates in the inner heliosphere due to their dependence on ψ. *Gleeson* and *Urch* (1968) used a separable diffusion coefficient to study modulation, i.e.

$$\kappa(r,\,\mathrm{P},\,t) = \beta^{\eta}\kappa_{1}(r,\;t)\kappa_{2}(\mathrm{P},\;t), \tag{4.6}$$

where the rigidity dependent factor, $\kappa_2(\mathrm{P},\ t)$, was chosen to be $\approx \mathrm{P}^{\gamma}$ with values of $\gamma = 1$ while $\eta = 1$. Since then, this assumption of separability has been questioned by many who preferred representing it as a function of scattering mean free path (e.g. *Burger*, 1971; *Burger* and *Swanenburg*, 1971 and *Bedijn et al.*, 1973). However, because of the fact that various published papers have been supporting and defending this separable diffusion coefficient in the form of equation 4.6 (e.g. *Gleeson* and *Urch*, 1971, 1973; *Caballero-Lopez* and *Moraal*, 2004 and *Moraal*, 2011), this study adopts it to study modulation. The reason is that it enables the Convection-Diffusion approximation (sections 4.5 to 4.7) and the Force-Field approximation (sections 4.8 to 4.10) to be used as an approximate solution to the full Parker transport equation. This separable diffusion coefficient form is based on a personal choice and can differ from one author to another in several ways.

The Parker transport equation convection term

In the full Parker equation, the term $\boldsymbol{\nabla}\cdot(\mathrm{CV}(r)f(r,\mathrm{P},\ t))$ represents convection. Convection describes the manner in which the solar wind "pushes" all the cosmic rays (on average) entering the spherically symmetric heliosphere. Understanding the "frozen-in" condition of the heliospheric magnetic field and the solar wind is very important, as discussed in section 2.8.3, to get a clear picture of cosmic-ray convection. Basically, when cosmic rays diffuse inward in a spherically symmetrical heliosphere these particles move inward due to the density gradient. This inward diffusion is countered by an outward "convective" flow carried by the solar wind.

4.5 The Convection-Diffusion solution

The Convection-Diffusion equation describes the lowest order approximate solution of the Parker equation for the transport of cosmic rays in a spherically symmetric heliosphere. This solution was proposed by *Krimsky* (1964) and precedes the full Parker transport equation by more than a year.

The process of Convection-Diffusion depends upon the speed of the solar wind and the heliospheric magnetic field. The total effect of these two quantities determines the number of cosmic rays entering (or being reflected from) the heliosphere. Therefore, one can anticipate that the modulation of cosmic rays will be greater when the solar wind speed is high and vice versa. The solar wind speed and the magnetic field cannot be deduced separately (*Moraal*, 2011). An approximate solution expression describing Convection-Diffusion has to be derived. For this, the following assumptions were made for the full Parker transport equation in a spherically symmetric heliosphere:

i) The diffusion tensor $\mathbf{K}(r, \mathrm{P}, t)$ collapses into a single coefficient κ and this single diffusion coefficient is expressed as a separable function of rigidity and heliocentric radial distance (equation 4.6). The heliocentric radial distance factor is assumed to be constant, i.e. $\kappa_1(r, t) = \kappa_1$ in unit of $\mathrm{cm}^2 \cdot \mathrm{s}^{-1} \cdot \mathrm{GV}^{-1}$ and the rigidity factor is assumed to take the form proposed by *Gleeson* and *Urch* (1971), i.e. $\kappa_2(\mathrm{P}, t) = \mathrm{P}_0^{(1-\gamma)}\mathrm{P}^{\gamma}$ in units of GV for any value of γ chosen. In this study, $\mathrm{P}_0 = 1$ GV.

ii) There are no additional sources of cosmic rays within the heliosphere, implying that $Q = 0$.

iii) The heliosphere is in a quasi steady-state condition, implying that $\partial f(r,\ \mathrm{P},\ t)\ /\ \partial t = 0$. This steady-state assumption means that the relaxation time of the distribution function is short with respect to the solar cycle duration of 11-years.

iv) The Compton-Getting coefficient C is assumed to be one in all convection terms.

v) The solar wind speed is assumed to be constant, i.e. $\mathrm{V}(r) = \mathrm{V}$

vi) The adiabatic energy loss term is neglected and there are no drifts.

vii) The dependence of the cosmic-ray intensity on direction is small.

Taking these assumptions into account, the majority of the terms in the full Parker transport equation vanish and a simplified equation is given as

$$\mathrm{V} f(r,\ \mathrm{P},\ t) - \kappa(r,\ \mathrm{P},\ t)\frac{\partial f(r,\ \mathrm{P},\ t)}{\partial r} = 0. \tag{4.7}$$

Re-arranging equation 4.7 and integrating from earth at $(r,\ \mathrm{P})$ to the LIS at $(r_{\mathrm{LIS}},\ \mathrm{P}_{\mathrm{LIS}})$ gives a solution of

$$f(r,\ \mathrm{P},\ t) = f_{\mathrm{LIS}}(r_{\mathrm{LIS}},\ \mathrm{P}_{\mathrm{LIS}},\ t)\mathrm{e}^{-M(r,\ t)} \quad \text{and} \quad M(r,\ t) = \int_{r}^{r_{\mathrm{LIS}}} \frac{\mathrm{V}}{\kappa(r,\ \mathrm{P},\ t)} dr, \tag{4.8}$$

where $f_{\mathrm{LIS}}(r_{\mathrm{LIS}},\ \mathrm{P}_{\mathrm{LIS}},\ t)$ is the distribution function at the outer boundary of the heliosphere and $M(r,\ t)$ is known as the dimensionless modulation function or the modulation depth (*Moraal*, 2014). Using the separable diffusion coefficient (equation 4.6), the dimensionless modulation function in equation 4.8 can be re-written as

$$\ln\left(\frac{f_{\mathrm{LIS}}(r_{\mathrm{LIS}},\ \mathrm{P}_{\mathrm{LIS}},\ t)}{f(r,\ \mathrm{P},\ t)}\right) = \int_{r}^{r_{\mathrm{LIS}}} \frac{\mathrm{V}}{\beta^{\eta}\kappa_{1}\kappa_{2}(\mathrm{P},\ t)}\,\mathrm{d}r \equiv M(r,\ t), \tag{4.9}$$

where

$$\beta = \begin{cases} 1 & \text{or} \\ \left[\mathrm{P} \Big/ \sqrt{\mathrm{P}^2 + (\mathrm{A}/\mathrm{Ze})^2 \mathrm{E}_0^2} \right]. \end{cases} \tag{4.10}$$

Henceforth, the second form of β is denoted as $\beta \neq 1$.

4.6 The Convection-Diffusion spectrum approximation

According to *Forman et al.* (1973) and *Moraal* (2011), modulation problems are simpler to understand and explore when the spectrum is given as a distribution function $f(r, \mathrm{P}, t)$. The spectrum in terms of the intensity is suited for experimental purposes because experiments measure intensities. Therefore, to interpret the measured intensities theoretically it is more useful to express them in terms of a distribution function. To do that the experimental measured intensities have to be divided by the squared rigidity (see, e.g., *Moraal*, 2011). Also, the energy in which these intensities were measured with has to be converted to rigidity through the energy-rigidity relation given by equation 2.8. Doing so will convert the measured intensities to distribution functions. This distribution function expresses the same dependence for the modulated cosmic-ray spectrum as the measured intensities spectrum but in terms of r, P and t. The equation that relates the distribution function to the measured differential intensity spectrum is

$$\left.\begin{aligned} j_{\mathrm{P}}(r, \mathrm{P}, t) &= f(r, \mathrm{P}, t)\mathrm{P}^2 \\ \Rightarrow \quad f(r, \mathrm{P}, t) &= \frac{j_{\mathrm{P}}(r, \mathrm{P}, t)}{\mathrm{P}^2} \\ j_{\mathrm{P,\,LIS}}(r_{\mathrm{LIS}}, \mathrm{P}_{\mathrm{LIS}}, t) &= f_{\mathrm{LIS}}(r_{\mathrm{LIS}}, \mathrm{P}_{\mathrm{LIS}}, t)\mathrm{P}_{\mathrm{LIS}}^2 \\ \Rightarrow \quad f_{\mathrm{LIS}}(r_{\mathrm{LIS}}, \mathrm{P}_{\mathrm{LIS}}, t) &= \frac{j_{\mathrm{P,\,LIS}}(r_{\mathrm{LIS}}, \mathrm{P}_{\mathrm{LIS}}, t)}{\mathrm{P}_{\mathrm{LIS}}^2} \end{aligned}\right\}, \tag{4.11}$$

where the units of the measured differential intensity spectra are particles·m^{-2}·s^{-1}·sr^{-1}·MeV^{-1}. The benefits and advantages of using equation 4.11 are discussed in detail in *Forman et al.* (1973).

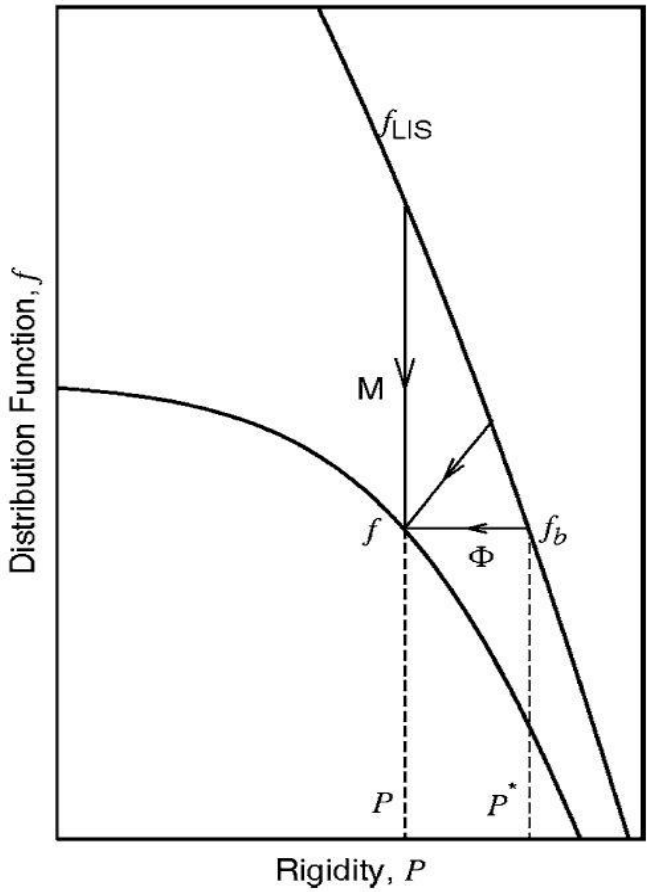

Figure 4.2: Graphic representation of the intensity reduction parameter $M(r,\ t)$ (vertical line) and energy (or rigidity) loss parameter $\Phi(r,\ t)$ (horizontal line). Source: *Caballero-Lopez* and *Moraal* (2004) and *Moraal* (2011).

Taking the ratio of $f(r,\ \mathrm{P},\ t)$ and $f_{\mathrm{LIS}}(r_{\mathrm{LIS}},\ \mathrm{P}_{\mathrm{LIS}}\ t)$ from equation 4.11 yields

$$\frac{f(r,\ \mathrm{P},\ t)}{f_{\mathrm{LIS}}(r_{\mathrm{LIS}},\ \mathrm{P}_{\mathrm{LIS}},\ t)} = \left(\frac{\mathrm{P}_{\mathrm{LIS}}}{\mathrm{P}}\right)^2 \left\{\frac{j_{\mathrm{P}}(r,\ \mathrm{P},\ t)}{j_{\mathrm{P,\ LIS}}(r_{\mathrm{LIS}},\ \mathrm{P}_{\mathrm{LIS}},\ t)}\right\}. \tag{4.12}$$

This ratio can be substituted into the solution of the Convection-Diffusion equation 4.8 to find

$$\left(\frac{\mathrm{P_{LIS}}}{\mathrm{P}}\right)^2 \left(\frac{j_{\mathrm{P}}(r,\,\mathrm{P},\,t)}{j_{\mathrm{P,\,LIS}}(r_{\mathrm{LIS}},\,\mathrm{P_{LIS}},\,t)}\right) = \mathrm{e}^{-M(r,\,t)}. \tag{4.13}$$

Therefore, the differential intensity spectrum is

$$j_{\mathrm{P}}(r,\,\mathrm{P},\,t) = j_{\mathrm{P,\,LIS}}(r_{\mathrm{LIS}},\,\mathrm{P_{LIS}},\,t)\left(\frac{\mathrm{P}}{\mathrm{P_{LIS}}}\right)^2 \mathrm{e}^{-M(r,\,t)}. \tag{4.14}$$

According to *Caballero-Lopez* and *Moraal* (2004), the particle rigidities at the LIS and at earth are assumed to be essentially the same (i.e. $\mathrm{P_{LIS}} = \mathrm{P}$) in the calculation of $M(r,\,t)$ (see Figure 4.2). Therefore, equation 4.14 becomes

$$j_{\mathrm{P}}(r,\,\mathrm{P},\,t) = j_{\mathrm{P,\,LIS}}(r_{\mathrm{LIS}},\,\mathrm{P},\,t)\mathrm{e}^{-M(r,\,t)}, \tag{4.15}$$

and this is known as the Convection-Diffusion spectrum approximation equation.

4.7 The Convection-Diffusion modulation changes

In section 4.5, the dimensionless modulation parameter $M(r,\,t)$ (equation 4.8) can be obtained at different positions (i.e. at r and r_{LIS}) and at the same rigidity between the LIS and earth. In this section, the same $M(r,\,t)$ at these positions is now obtained at two different times, i.e. at time t_1 and t_2. The modulation change between two specific times is calculated from equation 4.8 by taking the ratio of the distribution functions, i.e.

$$\frac{f(r_{t_2},\,\mathrm{P},\,t_2)}{f(r_{t_1},\,\mathrm{P},\,t_1)} = \frac{f_{\mathrm{LIS}}(r_{\mathrm{LIS},\,t_2},\,\mathrm{P},\,t_2)\;\mathrm{e}^{-M(r_{t_2},\,t_2)}}{f_{\mathrm{LIS}}(r_{\mathrm{LIS},\,t_1},\,\mathrm{P},\,t_1)\mathrm{e}^{-M(r_{t_1},\,t_1)}}. \qquad 4.16$$

Note that the possibility that the LIS itself as well where it occurs, can change, is taken into account in this expression. Taking the natural logarithm on both sides of equation 4.16

$$\ln\frac{f(r_{t_2},\,\mathrm{P},\,t_2)}{f(r_{t_1},\,\mathrm{P},\,t_1)} = \ln\frac{f_{\mathrm{LIS}}(r_{\mathrm{LIS},\,t_2},\,\mathrm{P},\,t_2)}{f_{\mathrm{LIS}}(r_{\mathrm{LIS},\,t_1},\,\mathrm{P},\,t_1)} - \Delta M(r_{t_1},\;r_{t_2},\;t_1,\;t_2), \qquad 4.17$$

where $\Delta M(r_{t_1},\;r_{t_2},\;t_1,\;t_2) = M(r_{t_2},\,t_2) - M(r_{t_1},\,t_1)$ is the modulation change between time t_2 and t_1. This modulation change could also be calculated between the radial position r and r_{LIS} at time t_2 and t_1 using 4.8 as

$$\Delta M(r_{t_1},\;r_{t_2},\;t_1,\;t_2) = \int_{r_{t_2}}^{r_{\mathrm{LIS},\,t_2}} \frac{\mathrm{V}}{\kappa(r_{t_2},\,\mathrm{P},\,t_2)}\,\mathrm{d}r_{t_2} - \int_{r_{t_1}}^{r_{\mathrm{LIS},\,t_1}} \frac{\mathrm{V}}{\kappa(r_{t_1},\;\mathrm{P},\;t_1)}\,\mathrm{d}r_{t_1}, \qquad 4.18$$

where $\kappa(r_{t_1},\;\mathrm{P},\;t_1) \approx \kappa(r_{t_2},\,\mathrm{P},\,t_2) = \beta^{\eta}\kappa_1\kappa_2(\mathrm{P},\,t_2)$ and $\kappa_2(\mathrm{P},\,t_2)$ is $\approx \mathrm{P}_0^{(1-\gamma)}\mathrm{P}^{\gamma}$. At neutron monitor energies r_{LIS} at time t_2 and t_1 is assumed to be the same. Performing the integration in equation 4.18 gives

$$\Delta M(r_{t_1},\;r_{t_2},\;t_1,\;t_2) = \frac{M^{*}(r_{t_1},\;t_1,\;r_{t_2},\;t_2)}{\beta^{\eta}\mathrm{P}_0^{(1-\gamma)}\mathrm{P}^{\gamma}}, \qquad (4.19)$$

where

$$M^{*}(r_{t_1},\;t_1,\;r_{t_2},\;t_2) = \frac{\mathrm{V}}{\kappa_1}[(r_{\mathrm{LIS}} - r_{t_2}) - \;(r_{\mathrm{LIS}} - r_{t_1})]. \qquad (4.20)$$

Substituting equation 4.19 into 4.17 gives

$$\ln\frac{f(r_{t_2},\,\mathrm{P},\,t_2)}{f(r_{t_1},\,\mathrm{P},\,t_1)} = \ln\frac{f_{\mathrm{LIS}}(r_{\mathrm{LIS}},\,\mathrm{P},\,t_2)}{f_{\mathrm{LIS}}(r_{\mathrm{LIS}},\,\mathrm{P},\,t_1)} - \frac{M^{*}(r_{t_1},\;t_1,\;r_{t_2},\;t_2)}{\beta^{\eta}\mathrm{P}_0^{(1-\gamma)}\mathrm{P}^{\gamma}}. \qquad (4.21)$$

Equation 4.21 can also be re-written as

$$\ln\frac{f(r_{t_2},\,\mathrm{P},\,t_2)}{f_{\mathrm{LIS}}(r_{\mathrm{LIS}},\,\mathrm{P},\,t_2)} = \ln\frac{f(r_{t_1},\,\mathrm{P},\,t_1)}{f_{\mathrm{LIS}}(r_{\mathrm{LIS}},\,\mathrm{P},\,t_1)} - \frac{M^{*}(r_{t_1},\;t_1,\;r_{t_2},\;t_2)}{\beta^{\eta}\mathrm{P}_0^{(1-\gamma)}\mathrm{P}^{\gamma}}. \tag{4.22}$$

Multiplying both sides of equation 4.22 with a negative sign and $\beta^{\eta}\mathrm{P}_0^{(1-\gamma)}\mathrm{P}^{\gamma}$ gives

$$\beta^{\eta}\frac{\mathrm{P}^{\gamma}}{\mathrm{P}_0^{(\gamma-1)}}\ln\frac{f_{\mathrm{LIS}}(r_{\mathrm{LIS}},\,\mathrm{P},\,t_2)}{f(r_{t_2},\,\mathrm{P},\,t_2)} = \beta^{\eta}\frac{\mathrm{P}^{\gamma}}{\mathrm{P}_0^{(\gamma-1)}}\ln\frac{f_{\mathrm{LIS}}(r_{\mathrm{LIS}},\,\mathrm{P},\,t_1)}{f(r_{t_1},\,\mathrm{P},\,t_1)} + M^{*}(r_{t_1},\;t_1,\;r_{t_2},\;t_2). \tag{4.23}$$

Let

$$M^{f}(r_{t_2},\,t_2) = \beta^{\eta}\frac{\mathrm{P}^{\gamma}}{\mathrm{P}_0^{(\gamma-1)}}\ln\frac{f_{\mathrm{LIS}}(r_{\mathrm{LIS}},\,\mathrm{P},\,t_2)}{f(r_{t_2},\,\mathrm{P},\,t_2)}, \tag{4.24}$$

and

$$M^{\mathrm{R}}(r_{t_1},\,t_1) = \beta^{\eta}\frac{\mathrm{P}^{\gamma}}{\mathrm{P}_0^{(\gamma-1)}}\ln\frac{f_{\mathrm{LIS}}(r_{\mathrm{LIS}},\,\mathrm{P},\,t_1)}{f(r_{t_1},\,\mathrm{P},\,t_1)}. \tag{4.25}$$

Then

$$M^{f}(r_{t_2},\,t_2) = M^{\mathrm{R}}(r_{t_1},\,t_1) + M^{*}(r_{t_1},\;t_1,\;r_{t_2},\;t_2). \tag{4.26}$$

$M^{f}(r_{t_2},\,t_2)$ is called the full Convection-Diffusion modulation parameter. This parameter is calculated in section 7.2. $M^{\mathrm{R}}(r_{t_1},\,t_1)$ is called the reference modulation parameter. This parameter is calculated with reference to the measured LIS intensities in section 6.6.2. $M^{*}(r_{t_1},\;t_1,\;r_{t_2},\;t_2)$ is called the modulation parameter change at neutron monitor energies. This parameter is calculated in section 5.2.1.

4.8 The Force-Field solution

The Force-Field solution is certainly the most generally used approximation of modulation theory. Similar to Convection-Diffusion, this approximation solution also dates back to the 1960s. In this study, the Force-Field solution calculated by *Gleeson* and *Urch* (1973) is presented. In order to calculate a simple expression describing the Force-Field solution, the same assumptions as for the Convection-Diffusion solution are used, with two exceptions.

The assumptions that differ compared with the Convection-Diffusion solution are that (1) the Compton-Getting coefficient, C, is assumed to be a function of rigidity, and (2) the rigidity dependence of the LIS and the spectra inside of the boundary are not the same. Therefore, taking those assumptions into account, the majority of the terms in the full Parker transport equation vanish, and a simplified Parker transport equation follows

$$\mathrm{CV}f(r,\ \mathrm{P},\ t) - \kappa(r,\ \mathrm{P},\ t)\frac{\partial f(r,\ \mathrm{P},\ t)}{\partial r} = 0, \tag{4.27}$$

where C is the Compton-Getting coefficient given as

$$\mathrm{C} = -\frac{1}{3}\frac{\partial(\ln f(r,\ \mathrm{P},\ t))}{\partial(\ln \mathrm{P})} = -\frac{1}{3}\frac{\mathrm{P}}{f}\frac{\partial f(r,\ \mathrm{P},\ t)}{\partial \mathrm{P}}. \tag{4.28}$$

Now substituting equation 4.28 into 4.27, equation 4.27 results in a first order partial differential equation of the form

$$\frac{\mathrm{PV}}{3}\frac{\partial f(r,\ \mathrm{P},\ t)}{\partial \mathrm{P}} + \kappa(r,\ \mathrm{P},\ t)\frac{\partial f(r,\ \mathrm{P},\ t)}{\partial r} = 0, \tag{4.29}$$

or

$$\frac{\partial \mathrm{P}}{\partial r} = -\frac{1}{3}\frac{\mathrm{PV}}{\kappa(r,\ \mathrm{P},\ t)}. \tag{4.30}$$

The solutions of equation 4.30 are characteristic lines, where the distribution function is constant in the $(r,\ \mathrm{P})$ and $(r_{\mathrm{LIS}},\ \mathrm{P}_{\mathrm{LIS}})$ plane, i.e. $f(r,\ \mathrm{P},\ t) \approx f_{\mathrm{LIS}}(r_{\mathrm{LIS}},\ \mathrm{P}_{\mathrm{LIS}},\ t)$ along contours of the characteristic equation. Using the fact that the total derivative of $f(r,\ \mathrm{P},\ t)$ is

$$df(r,\ \mathrm{P},\ t) = \frac{\partial f(r,\ \mathrm{P},\ t)}{\partial \mathrm{P}}d\mathrm{P} + \frac{\partial f(r,\ \mathrm{P},\ t)}{\partial r}dr = 0. \tag{4.31}$$

Since $df(r,\ \mathrm{P},\ t) = 0$, equation 4.31 can be re-written as

$$\frac{d\mathrm{P}}{dr} = -\frac{\partial f(r,\ \mathrm{P},\ t)}{\partial r}\frac{\partial \mathrm{P}}{\partial f(r,\ \mathrm{P},\ t)} = -\frac{\partial \mathrm{P}}{\partial r}. \tag{4.32}$$

Now, substituting equation 4.32 into 4.30

$$\frac{d\mathrm{P}}{dr} = \frac{1}{3}\frac{\mathrm{PV}}{\kappa(r,\ \mathrm{P},\ t)}. \tag{4.33}$$

Multiplying both sides of equation 4.33 by dr and P^{-1} and integrating from $(r,\ \mathrm{P})$ to $(r_{\mathrm{LIS}},\ \mathrm{P}_{\mathrm{LIS}})$, equation 4.33 can be re-written as

$$\int_{\mathrm{P}}^{\mathrm{P}_{\mathrm{LIS}}} \frac{1}{\mathrm{P}}d\mathrm{P} = \frac{1}{3}\int_{r}^{r_{\mathrm{LIS}}} \frac{\mathrm{V}}{\kappa(r,\ \mathrm{P},\ t)}dr. \tag{4.34}$$

Using the separable diffusion coefficient (equation 4.6), equation 4.34 can be re-written as

$$\int_{\mathrm{P}}^{\mathrm{P}_{\mathrm{LIS}}} \frac{\beta^{\eta}\kappa_{2}(\mathrm{P},\ t)}{\mathrm{P}}d\mathrm{P} = \frac{1}{3}\frac{\mathrm{V}}{\kappa_{1}}(r_{\mathrm{LIS}} - r) \equiv \Phi(r,\ t), \tag{4.35}$$

where the rigidity dependent factor, $\kappa_{2}(\mathrm{P},\ t)$, is chosen to be $\approx \mathrm{P}_{0}^{(1-\gamma)}\mathrm{P}^{\gamma}$ with $\gamma = 1$ and $\beta \approx 1$.

The quantity $\Phi(r,\ t)$ is known as the Force-Field rigidity (or energy) loss and it has units of GV (*Gleeson* and *Urch*, 1968; *Caballero-Lopez* and *Moraal*, 2004; *Moraal*, 2011; and *Ihongo* and *Wang*, 2016). In Figure 4.2, $\Phi(r,\ t)$ is represented by a solid horizontal line between $f_{\text{LIS}}(r_{\text{LIS}},\ \text{P}_{\text{LIS}},\ t)$ and $f(r,\ \text{P},\ t)$. The modulation parameter in the form of equation 4.35 causes rigidity changes while one of the assumptions in the full Parker transport equation neglected the adiabatic energy (or rigidity) loss term. *Gleeson* and *Urch* (1971) demonstrated that $\Phi(r,\ t)$ of equation 4.35 is an upper limit of the true adiabatic energy (or rigidity) loss.

According to *Gleeson* and *Axford* (1968); *Caballero-Lopez et al.* (2003); *Caballero-Lopez* and *Moraal* (2004) and *Moraal* (2011), the modulation rigidity loss $\Phi(r,\ t)$ is related to the modulation parameter $\phi(r,\ t)$ by $\Phi(r,\ t) = (A/Ze)\phi(r,\ t)$. This $\Phi(r,\ t)$ is only numerically equal to $\phi(r,\ t)$ when one deals with protons since the mass to charge ratio is ≈ 1. The diffusion coefficient parameters of the form of equation 4.6 with the values $\gamma = 1$ and $\beta = 1$ is the only case where $\Phi(r,\ t)$ can be converted to $\phi(r,\ t)$ from equation 4.35. The rigidity loss $\Phi(r,\ t)$ is usually quoted in GV, and the modulation parameter $\phi(r,\ t)$ is often quoted in GeV when the energy-rigidity equation (equation 2.8) is used.

4.9 The Force-Field intensity spectrum approximation

The cosmic-ray spectrum in terms of differential intensity is suited for experimental purposes because experiments measure intensities as a function of energy as mentioned. According to *Gleeson* and *Axford* (1968a), the differential intensity spectrum of the Force-Field solution to the full Parker transport equation is

$$j_{\mathrm{T}}(r,\ \mathrm{E}) = j_{\mathrm{T,\ LIS}}(\mathrm{E}+\Phi)\frac{(\mathrm{E}^2-\mathrm{E}_0^2)}{(\mathrm{E}+\Phi)^2-\mathrm{E}_0^2}, \tag{4.36}$$

where the units of the measured differential intensity spectrum at earth and at the LIS are both particles·m^{-2}·s^{-1}·sr^{-1}·MeV^{-1}. Here, E_0 is the rest mass energy in MeV and E is the total energy of the particle (i.e. the rest mass plus kinetic energy). Hence, Φ is known as modulation energy loss that particles suffer as they propagate inwards into the heliosphere (*Gleeson* and *Urch*, 1968).

The calculation of the Force-Field spectrum approximate equation follows the same approach as in section 4.6 until equation 4.12. In section 4.8, it was mentioned that the distribution functions between the earth and the LIS are constant in the $(r,\ \mathrm{P})$ and $(r_{\mathrm{LIS}},\ \mathrm{P}_{\mathrm{LIS}})$ plane, i.e. along contours of the characteristic equation. Therefore, applying this assumption in equation 4.12, the simplified Force-Field spectrum approximate equation becomes

$$j_{\mathrm{P}}(r,\ \mathrm{P},\ t) = j_{\mathrm{P,\ LIS}}(r_{\mathrm{LIS}},\ \mathrm{P}_{\mathrm{LIS}},\ t)\left(\frac{\mathrm{P}^2}{\mathrm{P}_{\mathrm{LIS}}^2}\right), \tag{4.37}$$

where the units of $j_{\mathrm{P}}(r,\ \mathrm{P},\ t)$ at earth and $j_{\mathrm{P,\ LIS}}(r_{\mathrm{LIS}},\ \mathrm{P}_{\mathrm{LIS}},\ t)$ at the LIS are both particles·m^{-2}·s^{-1}·sr^{-1}·MeV^{-1}. The rigidity at the LIS in equation 4.37 is calculated from equation 4.35, where P is represented by equation 2.8. The differential intensity spectrum at the LIS is parameterized in section 6.3 using Voyager - 1 intensities.

4.10 The Force-Field modulation changes

In section 4.8, the modulation rigidity loss, $\Phi(r,\ t)$, (equation 4.35) was obtained. In this section, the same $\Phi(r,\ t)$ is obtained at two different

times, i.e. at time t_1 and t_2. Therefore, the rigidity loss changes between time t_1 and t_2 can be obtained as

$$\Delta\Phi(r_{t_1},\ t_1,\ r_{t_2},\ t_2) = \Phi(r_{t_2},\ t_2) - \Phi(r_{t_1},\ t_1). \tag{4.38}$$

Now, switching from rigidity loss Φ to the modulation parameter ϕ, at time t_1

$$\phi(r_{t_1},\ t_1) = \mathrm{P}_{\mathrm{LIS},\ t_1} - \mathrm{P}_{t_1}, \tag{4.39}$$

and at time t_2

$$\phi(r_{t_2},\ t_2) = \mathrm{P}_{\mathrm{LIS},\ t_2} - \mathrm{P}_{t_2}. \tag{4.40}$$

Therefore, the equation that represents the modulation parameters between two specific times is

$$\mathrm{P}_{\mathrm{LIS},\ t_2} - \mathrm{P}_{t_2} = (\mathrm{P}_{\mathrm{LIS},\ t_1} - \mathrm{P}_{t_1}) + \Delta\phi(r_{t_1},\ t_1,\ r_{t_2},\ t_2). \tag{4.41}$$

Let

$$\phi^f(r_{t_2},\ t_2) = \mathrm{P}_{\mathrm{LIS},\ t_2} - \mathrm{P}_{t_2}, \tag{4.42}$$

and

$$\phi^{\mathrm{R}}(r_{t_1},\ t_1) = \mathrm{P}_{\mathrm{LIS},\ t_1} - \mathrm{P}_{t_1}. \tag{4.43}$$

Then

$$\phi^f(r_{t_2},\ t_2) = \phi^{\mathrm{R}}(r_{t_1},\ t_1) + \Delta\phi(r_{t_1},\ t_1,\ r_{t_2},\ t_2). \tag{4.44}$$

$\phi^f(r_{t_2},\ t_2)$ is called the full Force-Field modulation parameter. This parameter is calculated in section 7.3. $\phi^{\mathrm{R}}(r_{t_1},\ t_1)$ is called the reference modulation parameter. This parameter is calculated with reference to the measured LIS intensities in section 6.7.2. $\Delta\phi(r_{t_1},\ t_1,\ r_{t_2},\ t_2)$ is called the

modulation parameter change at neutron monitor energies. This parameter is calculated in section 5.2.2.

4.11 Summary

Modulation of cosmic rays, in particular the galactic cosmic rays inside the heliosphere, occurs as a result of their interaction with the solar wind and the heliospheric magnetic field. These particles experience changes in their intensities as a function of energy, position and time. The distribution of cosmic rays inside the heliosphere occurs as a result of four different processes, namely diffusion, drifts, convection and adiabatic energy loss. The cosmic-ray transport equation combines all these four major processes (*Parker*, 1965). The purpose of this chapter was to give a short overview of the existing knowledge of the semi-analytical methods used for solving the full Parker transport equation and in particular, the convection and diffusion processes.

Chapter 5

Calculation of modulation parameters using neutron monitor normalized measurements

5.1 Introduction

The modulation of cosmic rays is described by the full Parker transport equation as mentioned in section 4.3. A direct and meaningful comparison of the widely used Convection-Diffusion and Force-Field approximations is not a straightforward task. The modulation parameters presented in section 4.7 and 4.10 are now calculated using neutron monitor data.

The method used to calculate modulation parameters with the approximate solutions is discussed. The discussion unfolds in the order of their complexity, i.e. first the Convection-Diffusion and then the Force-Field approximation. Further sections illustrate the effects of varying the key components of the diffusion coefficient while special attention is given to the constants η , β , and γ (equation 4.6) and their influence on modulation parameters. This chapter is devoted to calculate the modulation time profiles from both approximations. At the end of this chapter a short summary is given.

5.2 Modelling count rates of neutron monitors

The normalized measured count rates plotted in Figure 4.1 for a specific neutron monitor are now discussed. As mentioned in section 4.7, reference times have to be chosen. The reference time March 1987 is denoted by t_{87} while for any other time it is denoted by t. The normalized measured count

rates of neutron monitors during solar minimum in March 1987 is denoted by $N^*(P_c,\ x,\ t_{87})$ and for any other time by $N^*(P_c,\ x,\ t)$. The average atmospheric pressure (depth) is denoted by x. Hence, t and t_{87} denote two different times and P_c is the cutoff rigidity.

In March 1987, all measured count rates of neutron monitors are normalized to 100 % as mentioned, i.e. $N^*(P_c,\ x,\ t_{87}) = 100\ \%$. The lowest normalized count rate by the SANAE neutron monitor during solar maximum in June 1991 was 73.12 %. Also, the lowest normalized count rates in the same year and month by the Hermanus, Potchefstroom and Tsumeb neutron monitors were 77.91 %, 80.36 % and 84.03 %, respectively (see column 4 of Table 5.1). The difference in normalized count rates between March 1987 and June 1991 is recorded in the last column of Table 5.1.

Table 5.1: The normalized measured count rates of neutron monitors in March 1987, June 1991 and the difference between March 1987 and June 1991.

Stations	P_c (GV)	$N^*(P_c,\ x,\ t_{87})$ (%)	$N^*(P_c,\ x,\ t_{91})$ (%)	Difference (%)
SANAE	0.8	100	73.12	26.88
Hermanus	4.9	100	77.91	22.09
Potchefstroom	7.2	100	80.36	19.64
Tsumeb	9.2	100	84.03	15.97

Now, to model the normalized count rates of neutron monitors using the approximate solutions introduced in sections 4.4.2 and 4.5.2, this study follows the parameterized neutron monitor count rate model proposed in section 3.5, i.e. the Dorman function. These count rates are called the modelled count rates. Therefore, the modelled count rates in March 1987 are denoted by $N(P_c,\ x,\ t_{87})$ and for any other time by $N(P_c,\ x,\ t)$.

The Dorman function for modelling count rates, applied to March 1987, is given as

$$N(\mathrm{P_c},\ x,\ t_{87}) = N_0(1-\exp(-\alpha\ /\ \mathrm{P_c^k})). \tag{5.1}$$

The best fit Dorman function constants, α, k and N_0, used to plot this function are the same as those used for Figure 3.3.

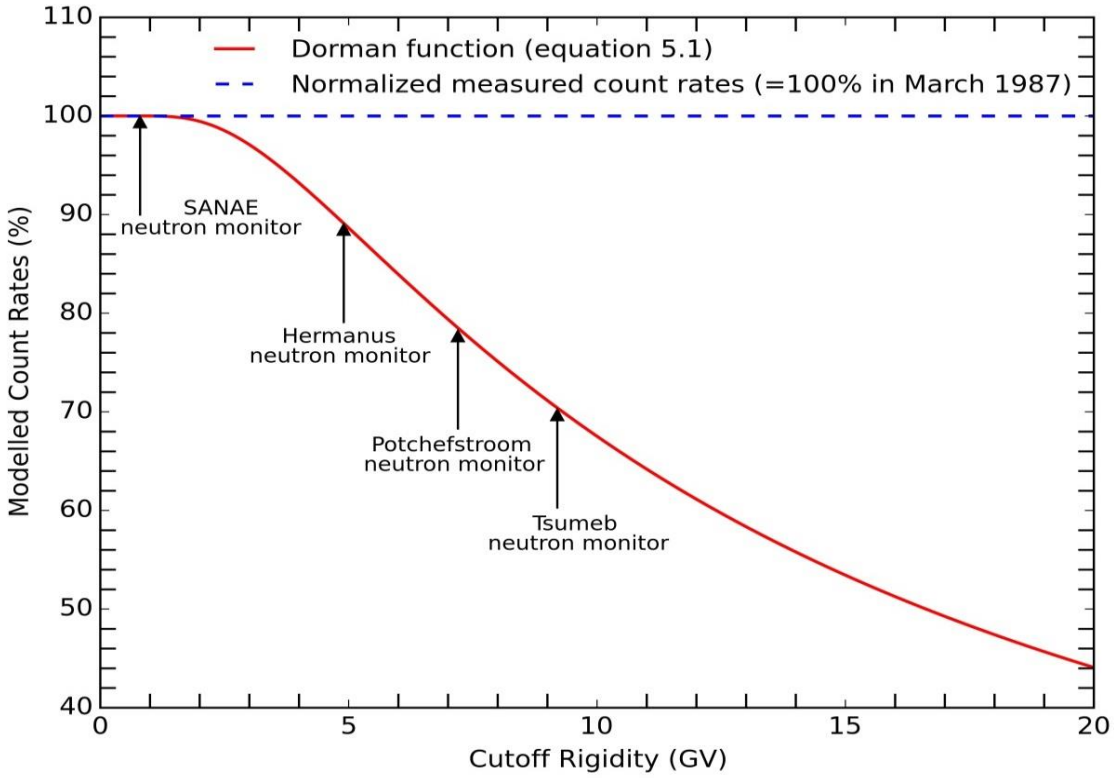

Figure 5.1: Example of the modelled count rate $N(\mathrm{P_c},\ x,\ t_{87})$ plotted as function of the cutoff rigidity $\mathrm{P_c}$ using the Dorman function (equation 5.1).

Figure 5.1 shows the modelled count rate $N(\mathrm{P_c},\ x,\ t_{87})$ as a function of cutoff rigidity $\mathrm{P_c}$. From the figure, the flat portion of the modelled count rate $N(\mathrm{P_c},\ x,\ t_{87})$ at $\mathrm{P_c} < 1$ GV is due to the fact that the geomagnetic cutoff becomes smaller than the atmospheric cutoff at ≈ 1 GV, according to *Caballero-Lopez* and *Moraal* (2012). The flat blue broken line at 100 % represents the normalized measured count rates of neutron monitors in March 1987. The figure shows that the model is in good agreement with

the neutron monitor count rates, specified relative to the count rate at a very small cutoff rigidity. The same good fit was obtained for a latitude survey as shown in Figure 3.3.

Table 5.2 compares the normalized measured count rates of neutron monitors (column 2), modelled count rates (column 3) and the difference between the normalized measured count rates and modelled count rates (column 4) in March 1987. Column 4 shows that these differences increase with cutoff rigidity.

Table 5.2: Comparison of the normalized measured count rates, modelled count rates and the difference between them in March 1987

P_c (GV)	$N^*(P_c,\ x,\ t_{87})$ (%)	$N(P_c,\ x,\ t_{87})$ (%)	Difference (%)
0.8	100	99.997	0.003
4.9	100	89.11	10.9
7.2	100	78.50	21.5
9.2	100	70.40	29.6

The function that relates any modelled count rate to the March 1987 count rate is formulated from the theoretical differential response function, i.e. for March 1987

$$\int_{P_c}^{\infty}\left(-\frac{dN(P_{t_{87}},\ x,\ t_{87})}{dP_{t_{87}}}\right)dP_{t_{87}} = \int_{P_c}^{\infty} S(x,\ P_{t_{87}})j_P(r_{t_{87}},\ P_{t_{87}},\ t_{87})dP_{t_{87}}. \qquad (5.2)$$

For any other time, the function is given as

$$\int_{P_c}^{\infty}\left(-\frac{dN(P_t,\ x,\ t)}{dP_t}\right)dP_t = \int_{P_c}^{\infty} S(x,\ P_t)j_P(r_t,\ P_t,\ t)dP_t, \qquad (5.3)$$

where $\mathrm{S}(x,\ \mathrm{P}_{t_{87}})$ and $\mathrm{S}(x,\ \mathrm{P}_t)$ represent the yield function dependent on rigidity in March 1987 and rigidity in other time t, respectively. Also, $j_{\mathrm{P}}(r_{t_{87}},\ \mathrm{P}_{t_{87}},\ t_{87})$ and $j_{\mathrm{P}}(r_t,\ \mathrm{P}_t,\ t)$ represents differential intensity spectrum in March 1987 and any other time, respectively. Taking the ratio of the integrands of equation 5.2 and 5.3, the count rates of the model at any other time are calculated as

$$N(\mathrm{P}_{\mathrm{c}},\ x,\ t) = \int_{\mathrm{P}_{\mathrm{c}}}^{\infty} \left(\frac{dN(\mathrm{P}_{t_{87}},\ x,\ t_{87})}{d\mathrm{P}_{t_{87}}} \right) \frac{\mathrm{S}(x,\ \mathrm{P}_t) j_{\mathrm{P}}(r_t,\ \mathrm{P}_t,\ t)}{\mathrm{S}(x,\ \mathrm{P}_{t_{87}}) j_{\mathrm{P}}(r_{t_{87}},\ \mathrm{P}_{t_{87}},\ t_{87})} d\mathrm{P}_t. \tag{5.4}$$

In this study, the modelled count rates $N(\mathrm{P}_{\mathrm{c}},\ x,\ t)$ is calculated by using two different approaches. The first approach is the Convection-Diffusion approximation (see section 5.2.1). The second approach is the Force-Field approximation (see section 5.2.2). It is expected that these approximate solutions should be very similar. That is, the total modulation parameter $\Delta\phi$ required to produce modulation for particles detected at 1 AU is nearly 1/3 of the modulation parameter M^*. This comparison is shown in section 5.3.

5.2.1 The Convection-Diffusion approach

In this section, the modelled count rates $N(\mathrm{P}_{\mathrm{c}},\ x,\ t)$ is calculated at a specific cutoff rigidity P_{c}. From equation 5.4, the proton differential intensity spectrum $j_{\mathrm{P}}^{\mathrm{Proton}}(r_{t_{87}},\ \mathrm{P},\ t_{87})$ in March 1987 and $j_{\mathrm{P}}^{\mathrm{Proton}}(r_t,\ \mathrm{P},\ t)$ at any other time is calculated from equation 4.15. According to equation 4.15 the ratio of the differential intensity spectrum in 1987 and any other time is

$$\frac{j_{\mathrm{P}}^{\mathrm{Proton}}(r_t,\ \mathrm{P},\ t)}{j_{\mathrm{P}}^{\mathrm{Proton}}(r_{t_{87}},\ \mathrm{P},\ t_{87})} = \frac{j_{\mathrm{P,\ LIS}}^{\mathrm{Proton}}(r_{\mathrm{LIS},\ t},\ \mathrm{P},\ t)}{j_{\mathrm{P,\ LIS}}^{\mathrm{Proton}}(r_{\mathrm{LIS},\ t_{87}},\ \mathrm{P},\ t_{87})} e^{-\Delta M(r_t,\ r_{t_{87}},\ t,\ t_{87})}, \tag{5.5}$$

where

$$-\Delta M(r_t,\ r_{t_{87}},\ t,\ t_{87}) = -\frac{M^*(r_{t_1},\ t_1,\ r_{t_2},\ t_2)}{\beta^{\eta}\mathrm{P}_0^{(1-\gamma)}\mathrm{P}^{\gamma}}. \tag{5.6}$$

The differential LIS parameterization in equation 5.5 is chosen to be essentially the same in March 1987 as at any other time, i.e. $j^{\text{Proton}}_{\text{P, LIS}}(r_{\text{LIS, }t_{87}},\ \mathrm{P},\ t_{87}) \approx j^{\text{Proton}}_{\text{P, LIS}}(r_{\text{LIS, }t},\ \mathrm{P},\ t)$. Also, the rigidity dependence of the yield function in March 1987, $\mathrm{P}_{t_{87}}$, or any other time, P_t, is assumed to be the same. Substituting equations 5.5 and 5.6 into equation 5.4, the Convection-Diffusion neutron monitor count rate is given as

$$N(\mathrm{P}_c,\ x,\ t) = \int_{\mathrm{P}_c}^{\infty} \alpha k \mathrm{N}_0 \exp(-\alpha \mathrm{P}_c^{-k})\mathrm{P}_c^{-k-1}\ e^{-\left(\frac{M^*(r_{t_1},\ t_1,\ r_{t_2},\ t_2)}{\beta^{\eta}\mathrm{P}_0^{(1-\gamma)}\mathrm{P}^{\gamma}}\right)} d\mathrm{P}, \tag{5.7}$$

where the constants α, k and N_0 are the same as those used to plot Figure 5.1. Using equation 5.7, the following procedure was followed to calculate $N(\mathrm{P}_c,\ x,\ t)$, i.e.

i) The values of $\eta = 1$ and $\beta = 1$ (or $\beta \neq 1$) were chosen. The values of γ chosen were between 0.8 and 1.2.

ii) As mentioned before, the measured count rates of neutron monitors chosen in this study were normalized to 100 % in March 1987 and the lowest count rate for all the neutron monitors during solar maximum was in June 1991. Therefore, any positive value for M^* can be chosen for all neutron monitors starting from 0. The value of $M^* = 0$ makes equation 5.7 equivalent to the Dorman function which was used to fit the 1987 measurements from a mobile neutron monitor survey. Therefore, depending on the neutron monitor cutoff rigidity, M^* was changed until the modelled $N(\mathrm{P}_{c,\,t},\ x,\ t)$ was the same as the normalized measured count rate during solar maximum in June 1991.

iii) The modelled values for $N(P_c, x, t)$ using $\beta = 1$ were compared with those calculated using $\beta \neq 1$ for the same γ.

Using the above procedure, the relationship between the modelled count rate $N(P_c, x, t)$ and cutoff rigidity P_c was obtained for different chosen values of M^*. Figures 5.2a and 5.2b show $N(P_c, x, t)$ as a function of P_c for different chosen values of M^*. In both figures the modelled count rates $N(P_c, x, t)$ was plotted based on a combination of β and γ. That is, for Figure 5.2a $\beta = 1$ and $\gamma = 1$, and for Figure 5.2b, $\beta \neq 1$ and $\gamma = 1$. To demonstrate the effects of the choice of β and γ in the calculation of $N(P_c, x, t)$ as a function of P_c, values of M^* were chosen from 0 to 5 GV in steps of 0.01 GV in each panel.

In Figure 5.2a, the chosen values of M^* have an inverse relationship with values of $N(P_c, x, t)$. That is, when $M^* = 0$ was chosen the modelled count rate of $N(P_c, x, t)$ was 100 % at $P_c < 1$ GV (as seen in Figure 5.1). Hence, when the values of $M^* > 0$ were chosen the modelled values of $N(P_c, x, t)$ became less than 100 % at $P_c < 1$ GV. Similarly, Figure 5.2b, shows the same inverse relationship when comparing the chosen M^* and the modelled values of $N(P_c, x, t)$.

The other inverse relationship seen in both panels was between the modelled count rate $N(P_c, x, t)$ and cutoff rigidity P_c. When P_c increases, $N(P_c, x, t)$ tends to decrease.

Now, the chosen values of M^* from both figures were plotted as a function of the modelled count rate $N(P_c, x, t)$ at different cutoff rigidities, P_c (as seen in Figures 5.3).

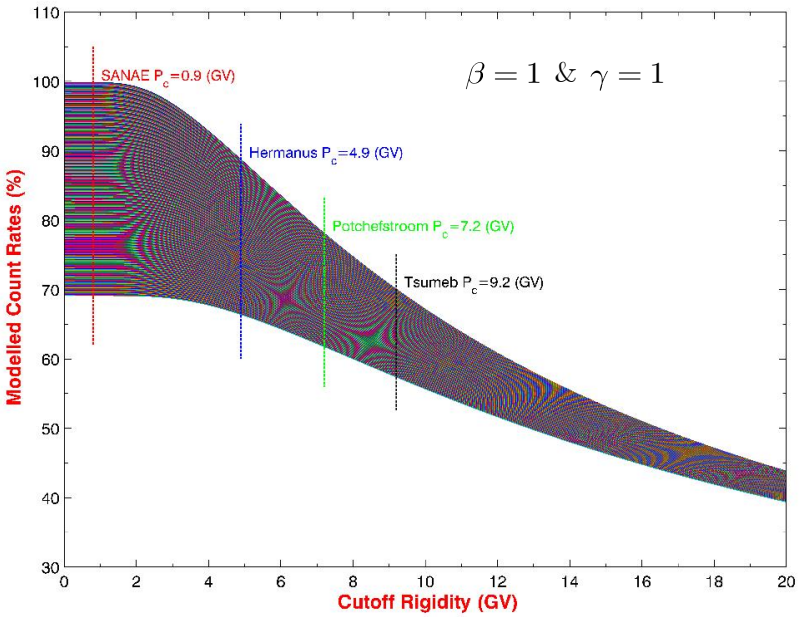

Figure 5.2a: Example of the modelled count rate $N(\mathrm{P_c}, x, t)$ plotted as a function of cutoff rigidity $\mathrm{P_c}$ at different values of M^*, varying from 0 (top curve) to 5 GV (bottom curve).

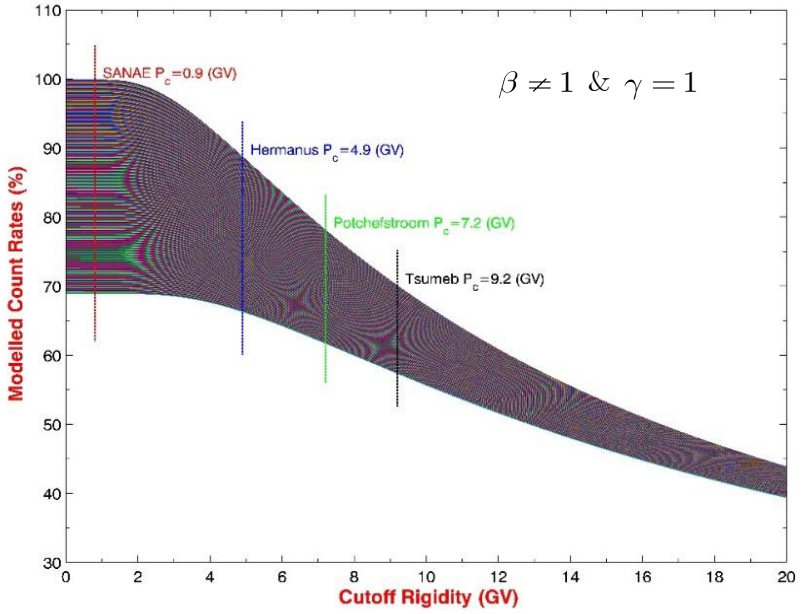

Figure 5.2b: Example of the modelled count rate $N(\mathrm{P_c}, x, t)$ plotted as a function of cutoff rigidity $\mathrm{P_c}$ at different values of M^*, varying from 0 (top curve) to 5 GV (bottom curve).

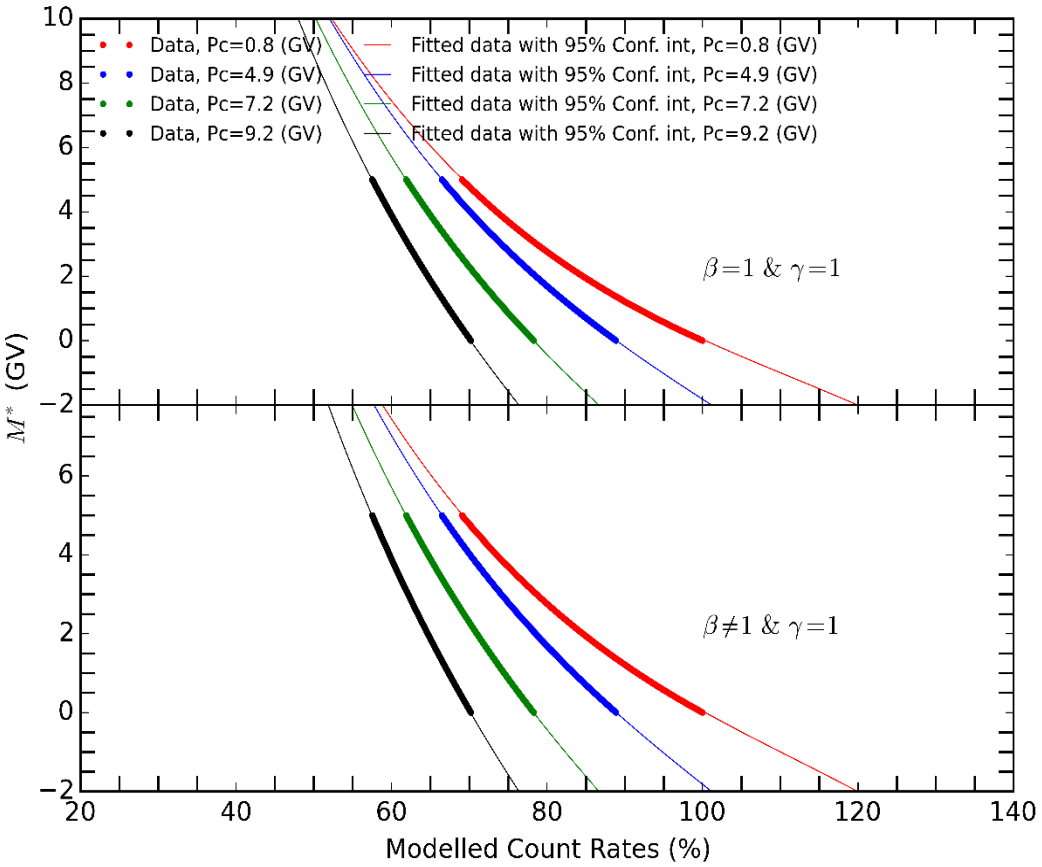

Figure 5.3: The modulation parameter M^* as a function of the modelled count rate $N(\mathrm{P_c},\ x,\ t)$ on a linear scale. The solid lines represent equation 5.8.

The relationship between the plotted values of M^* against $N(\mathrm{P_c},\ x,\ t)$ (substituted as N) was obtained by finding a fit function for these data points. A polynomial fit function of the order of three was obtained as

$$M^* = a(N)^3 + b(N)^2 + c(N) + d, \tag{5.8}$$

where the polynomial coefficients a, b, c and d are real numbers given in Table 5.3 and 5.4. The numbers in brackets represents the confidence bounds coefficients of $N(\mathrm{P_c},\ x,\ t)$ with 95 %. The coefficients of M^* from Figure 5.2a are represented in Table 5.3 and those of Figure 5.2b are represented in Table 5.4. The solid lines of Figure 5.3 represent equation 5.8. The polynomial equation 5.8 is cutoff rigidity dependent. Now the problem is to link the time-dependent normalized measured count

rates from a neutron monitor to the cutoff rigidity dependent modelled count rates. The modelled count rates $N(\mathrm{P_c},\ x,\ t)$ were converted to the time-dependent normalized measured count rates $N^*(\mathrm{P_c},\ x,\ t)$ in the following way

$$N(\mathrm{P_c},\ x,\ t) = N^*(\mathrm{P_c},\ x,\ t)\left(\frac{N(\mathrm{P_c},\ x,\ t_{87})}{N^*(\mathrm{P_c},\ x,\ t_{87})}\right), \tag{5.9}$$

where $N(\mathrm{P_c},\ x,\ t_{87})$ is the modelled count rate calculated in March 1987 from equation 5.1 (or equation 5.7 when $M^* = 0$) at a specific cutoff rigidity, $\mathrm{P_c}$. In equation 5.9, $N^*(\mathrm{P_c},\ x,\ t_{87})$ is the measured count rate in March 1987 from neutron monitors, normalized to 100 %.

Table 5.3: Coefficients with 95 % confidence bounds in brackets

Coefficients		
$\mathrm{P_c}$	a	b
08	-2.487e-05 (-2.507e-05,-2.466e-05)	0.008316 (0.008264, 0.008368)
4.9	-3.22e-05 (-3.242e-05,-3.199e-05)	0.009985 (0.009935, 0.01003)
7.2	-4.816e-05 (-4.841e-05,-4.791e-05)	0.01363 (0.01358, 0.01369)
9.2	-7.049e-05 (-7.08e-05,-7.018e-05)	0.0183 (0.01824, 0.01836)
$\mathrm{P_c}$	c	d
08	-1.03 (-1.035,-1.026)	44.72 (44.6, 44.84)
4.9	-1.189 (-1.192,-1.185)	49.37 (49.27, 49.47)
7.2	-1.504 (-1.507,-1.5)	57.28 (57.2, 57.37)
9.2	-1.867 (-1.871,-1.864)	65.27 (65.19, 65.35)

Table 5.4: Coefficients with 95 % confidence bounds in brackets

Coefficients		
P_c	a	d
08	-2.496e-05 (-2.517e-05,-2.475e-05)	0.008369 (0.008316, 0.008422)
4.9	-3.236e-05 (-3.257e-05,-3.214e-05)	0.01002 (0.009971, 0.01007)
7.2	-4.825e-05 (-4.85e-05,-4.799e-05)	0.01365 (0.01359, 0.0137)
9.2	-7.055e-05 (-7.086e-05,-7.024e-05)	0.01831 (0.01825, 0.01837)
P_c	c	d
08	-1.035 (-1.04,-1.031)	44.81 (44.69, 44.93)
4.9	-1.19 (-1.194,-1.186)	49.34 (49.24, 49.44)
7.2	-1.504 (-1.508,-1.5)	57.23 (57.15, 57.32)
9.2	-1.867 (-1.871,-1.863)	65.22 (65.14, 65.3)

Now, substituting equation 5.9 (as $N(t)$ into equation 5.8), the time-dependent modulation parameter from normalized measured count rates of neutron monitors is

$$M^* = aN(t)^3 + bN(t)^2 + cN(t) + d, \qquad (5.10)$$

where coefficients a, b, c and d are the same as those used in equation 5.8. Therefore, using equation 5.10 and the long-term records of monthly data from the neutron monitors chosen in this study, the time-dependent modulation parameters were calculated for each station. These calculated

M^* were plotted in Figure 5.4a (from panel (a) to (e)) and Figure 5.4b (from panel (f) to (j)) as a function of time. The values of M^* were based on a combination of β and γ for all four stations at different cutoff rigidities, P_c. The combination of $\beta = 1$ while γ takes values 0.8, 0.9, 1.0, 1.1 and 1.2 is shown in Figure 5.4a panels (a), (b), (c), (d) and (e), respectively. The combination of $\beta \neq 1$ while γ takes on 0.8, 0.9, 1.0, 1.1 and 1.2 is shown in Figure 5.4b panels (f), (g), (h), (i) and (j), respectively.

From the figures, the calculated values of M^* from July 1957 to October 2016 show two main cycles, i.e. the 11-year and the 22-year periodic cycles. The imprint of the 11-years cycle in these calculated values of M^* anti-correlates with the normalized measured count rates of neutron monitors. Also worth noting was that during the 2009 solar minimum, the M^* values calculated showed a very low value compared with March 1987 solar minimum. Note that this quantity can become negative for physical reasons, but these are not discussed in this study.

The calculated values of M^* from the four individual stations are quite close to each other for all years except for 1989, 1994 to 1998 and 2008 to 2010, reflecting the neutron monitor cutoff rigidity dependence. The time between 1989 and 1991 was characterized by Forbush decreases (see also *Usoskin et al.*, 2005) which distorts M^*. In Figures 5.4a and 5.4b, the calculated M^* for individual stations is the same in March 1987. Values of M^* during solar maximum in June 1991 are very high compared with those of March 1987. A summary is given in Table 5.5 listing all calculated values of M^* during solar maximum in June 1991 for $\beta = 1$ and $\beta \neq 1$ for a specific γ. Column 3 represents M^* for $\beta = 1$ at a specific γ and column 4 represent M^* for $\beta \neq 1$ at a specific γ. Column 5 represents the differences between them while γ takes on 0.8, 0.9, 1.0, 1.1 and 1.2.

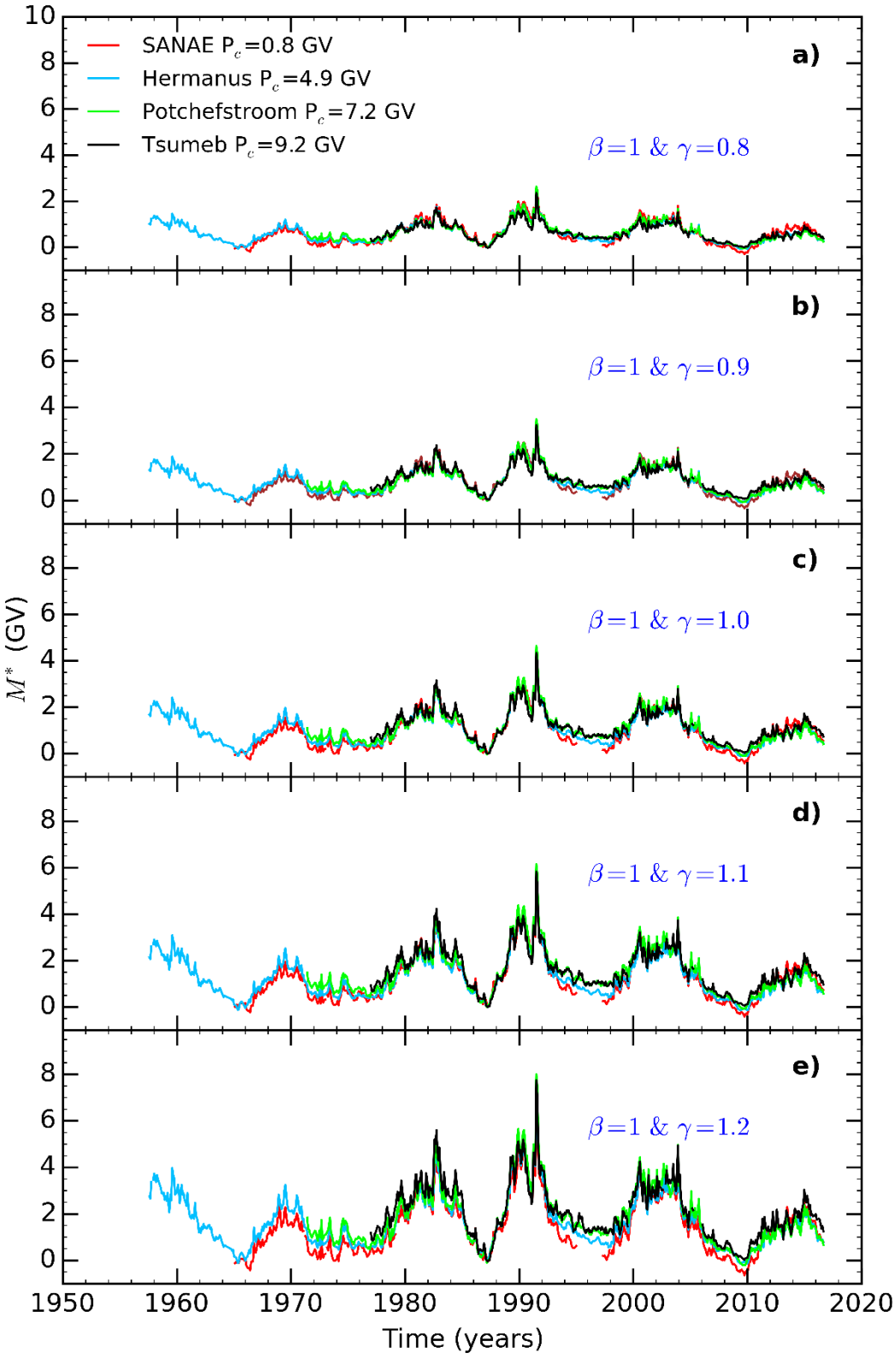

Figure 5.4a: Calculated M^* using neutron monitor data from July 1957 to October 2016

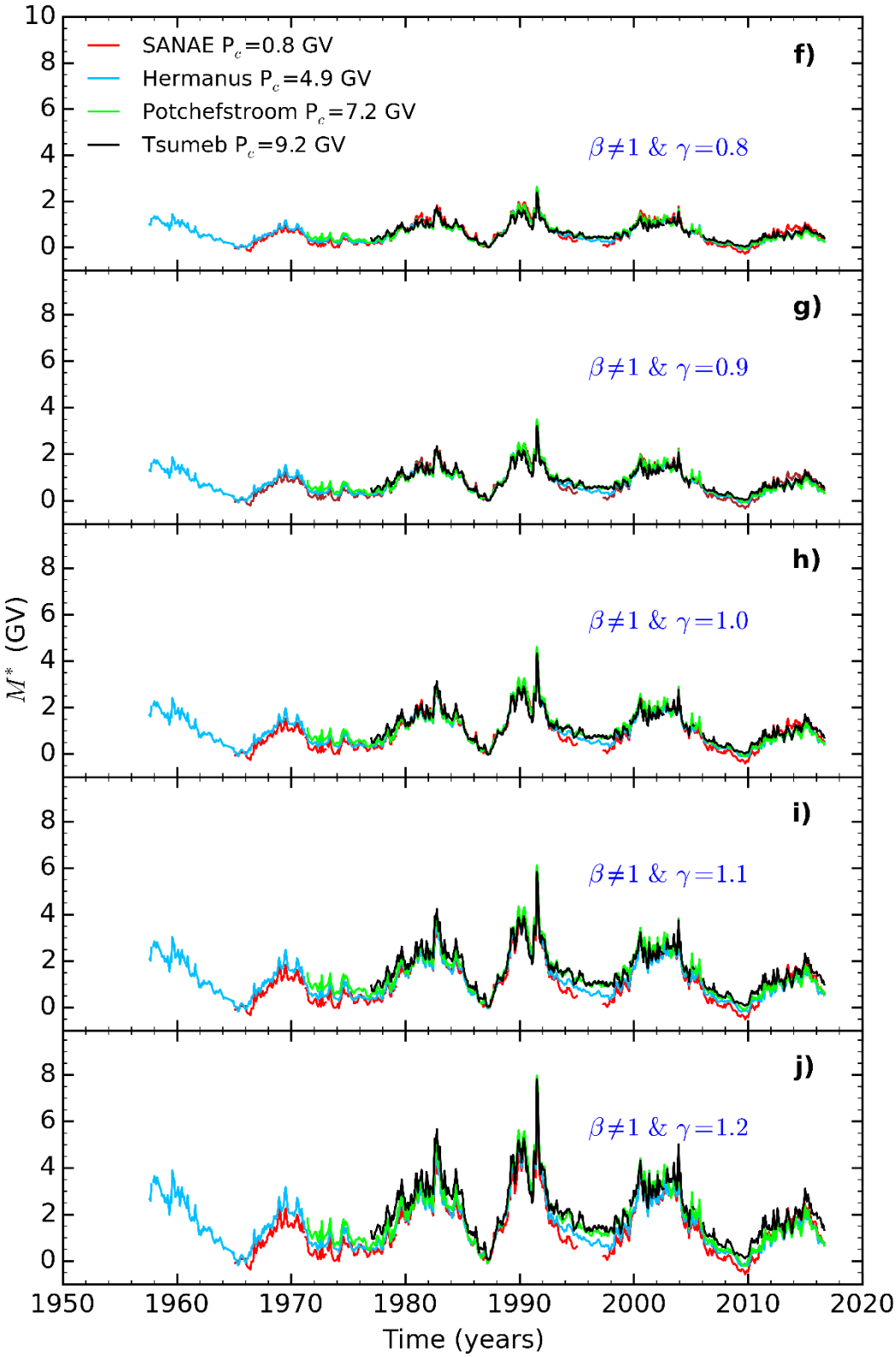

Figure 5.4b: Calculated M^* using neutron monitor data from July 1957 to October 2016

Table 5.5: The calculated M^* for $\beta = 1$ and $\beta \neq 1$ for a specific γ and the differences between them for June 1991.

Station	γ	M^* for $\beta = 1$	M^* for $\beta \neq 1$	Difference
SANAE	0.8	2.59	2.56	0.03
	0.9	3.28	3.25	0.03
	1.0	4.14	4.09	0.05
	1.1	5.23	5.01	0.22
	1.2	6.49	6.40	0.09
Hermanus	0.8	2.53	2.52	0.01
	0.9	3.29	3.27	0.02
	1.0	4.25	4.24	0.01
	1.1	5.47	5.42	0.05
	1.2	7.06	6.96	0.1
Potchefstroom	0.8	2.64	2.63	0.01
	0.9	3.5	3.49	0.01
	1.0	4.64	4.62	0.02
	1.1	6.15	6.12	0.03
	1.2	8.02	7.97	0.05
Tsumeb	0.8	2.36	2.31	0.05
	0.9	3.25	3.22	0.03
	1.0	4.34	4.32	0.02
	1.1	5.82	5.53	0.32
	1.2	7.76	7.81	0.05

In Figures 5.4a and 5.4b, the calculated M^* for individual stations is the same in March 1987. Values of M^* during solar maximum in June 1991 are very high compared with those of March 1987. A summary is given in Table 5.5 listing all calculated values of M^* during solar maximum in June 1991 for $\beta = 1$ and $\beta \neq 1$ for a specific γ. Column 3 represents M^* for $\beta = 1$ at a specific γ and column 4 represent M^* for $\beta \neq 1$ at a

specific γ. Column 5 represents the differences between them while γ takes on 0.8, 0.9, 1.0, 1.1 and 1.2. For all the calculated M^* in Figures 5.4a and 5.4b, Table 5.5 shows that whether the relativistic limit of β is used, or the exact expression, leads to a change of less than 5 % for all values of γ considered. However, changing γ by 50 %, results in a factor of two or more change in M^*. An estimate for an acceptable value of γ is deferred to section 5.3.

5.2.2 The Force-Field approach

This section presents no new physics pertaining to modulation of cosmic rays apart from the fact that the modulation parameter, $\Delta\phi(r_{t_1},\ t_1,\ r_{t_2},\ t_2)$, is now calculated using neutron monitor data. To calculate the time-dependent $\Delta\phi(r_{t_1},\ t_1,\ r_{t_2},\ t_2)$, a simple method might be used provided the Convection-Diffusion modulation function is known. According to *Gleeson and Urch* (1973) this equation is given as

$$\frac{\phi}{\kappa_2} = \beta\frac{M}{3}. \tag{5.11}$$

However, it would be incorrect to use this procedure to calculate $\Delta\phi(r_{t_1},\ t_1,\ r_{t_2},\ t_2)$, because the parameters for ϕ and M are not the same, and the assumptions, range of validity and limitations made for the two approximations differ. For these reasons it is advisable to use equation 5.11 for comparisons purposes only, which might also serve as an independent test to confirm its validity.

Similar to the Convection-Diffusion approximation, this section also starts by calculating count rates from the model and comparing them with the normalized measured count rate from a neutron monitor. However, the differences compared with the Convection-Diffusion approximation are that:

i) In this Force-Field approximation, the yield function that was excluded is now taken into account. However, the LIS is still assumed to remain constant.

ii) In this approach there are certain restrictions imposed on the type of diffusion coefficient one can use and still obtain simple expressions. For example, *Caballero-Lopez* and *Moraal* (2004) and *Moraal* (2011) show that if the diffusion coefficient, $\kappa(r,\ \mathrm{P},\ t)$, have parameter values $\eta = 1$, $\beta = 1$ and $\gamma = 1$ in equation 4.6, the solution describing the modulation parameter reduces to the widely used form, $\Delta\phi(r_{t_1},\ t_1,\ r_{t_2},\ t_2) = \mathrm{P}_{t_{87}} - \mathrm{P}_t$. This form occurs because at neutron monitor energies $\mathrm{P}_{\mathrm{LIS}}$ at time t_2 and t_1 is assumed to be the same.

The parameterized differential response function to be used in equation 5.4 is the same as that in chapter 3 (equation 3.3).

$$\frac{dN(\mathrm{P}_{t_{87}},\ x,\ t_{87})}{d\mathrm{P}_{t_{87}}} = \alpha k N_0 e^{(-\alpha \mathrm{P}_{t_{87}}^{-k})} \mathrm{P}_{t_{87}}^{-k-1}. \tag{5.12}$$

The yield function used is a parameterized double power law equation adopted from *Caballero-Lopez* and *Moraal* (2012) equation 2. In equation 5.4, the ratio of the proton yield functions for any other time to March 1987 is given as

$$\xi(\mathrm{P}_t,\ \mathrm{P}_{t_{87}},\ x) = \frac{\mathrm{S}^{\mathrm{Proton}}(\mathrm{P}_t,\ x)}{\mathrm{S}^{\mathrm{Proton}}(\mathrm{P}_{t_{87}},\ x)} = \frac{\mathrm{S}_0(\mathrm{P}_0^a + \mathrm{P}_t^a)^{(\gamma_1-\gamma_2)/a}\mathrm{P}_t^{\gamma_2}}{\mathrm{S}_0(\mathrm{P}_0^a + \mathrm{P}_{t_{87}}^a)^{(\gamma_1-\gamma_2)/a}\mathrm{P}_{t_{87}}^{\gamma_2}}, \tag{5.13}$$

where S_0, P_0, a, γ_1 and γ_2 are constants identical to those used in equation 3.5. According to equation 4.36, which was formulated from the distribution functions, the ratio of the proton differential intensity spectrum for any other time to that of March 1987 is given as

$$\frac{j_{\mathrm{P}}^{\mathrm{Proton}}(r_t,\ \mathrm{P}_t,\ t)}{j_{\mathrm{P}}^{\mathrm{Proton}}(r_{t_{87}},\ \mathrm{P}_{t_{87}},\ t_{87})} = \left(\frac{\mathrm{P}_t}{\mathrm{P}_{t_{87}}}\right)^2 \tag{5.14}$$

where $\mathrm{P}_{t_{87}} = \mathrm{P}_t + \Delta\phi$. The rigidity P_t is given in equation 2.8. Substituting equations 5.12, 5.13 and 5.14 into 5.4, the Force-Field neutron monitor count rate equation is given as

$$N(\mathrm{P_c},\ x,\ t) = \int_{\mathrm{P_c}}^{\infty} \alpha k \mathrm{N}_0 \exp(-\alpha \mathrm{P}_c^{-k}) \mathrm{P}_c^{-k-1}\ \xi(\mathrm{P}_t,\ \mathrm{P}_{t_{87}},\ x) \left(\frac{\mathrm{P}_t}{\mathrm{P}_{t_{87}}}\right)^2 d\mathrm{P}_t\ . \tag{5.15}$$

To calculate $N(\mathrm{P_c},\ x,\ t)$, the same procedure as in section 5.2.1 was followed. However, the differences compared with that procedure are that:

i) The only values which will be considered for the diffusion coefficient parameters in equation 4.6 are $\eta = 1$, $\beta = 1$ and $\gamma = 1$.

ii) Here, $\Delta\phi$ values are chosen in equation 5.15 from 0 to 1.5 GV in steps of 0.01 GV. Everything else is the same, i.e. if $\Delta\phi = 0$ this makes equation 5.15 to be equivalent to the Dorman function which was used to fit the 1987 measurements from a mobile neutron monitor survey. Also, $\Delta\phi$ is changed until the modelled $N(\mathrm{P_c},\ x,\ t)$ is the same as that measured during solar maximum in June 1991 by all neutron monitors chosen in this study.

No unnecessary repetition will be done in this section, henceforth only results from this Force-Field approximation are shown.

The relationship between the modelled count rate $N(\mathrm{P_c},\ x,\ t)$ and cutoff rigidity $\mathrm{P_c}$ are shown in Figure 5.5 for different chosen values of $\Delta\phi$.

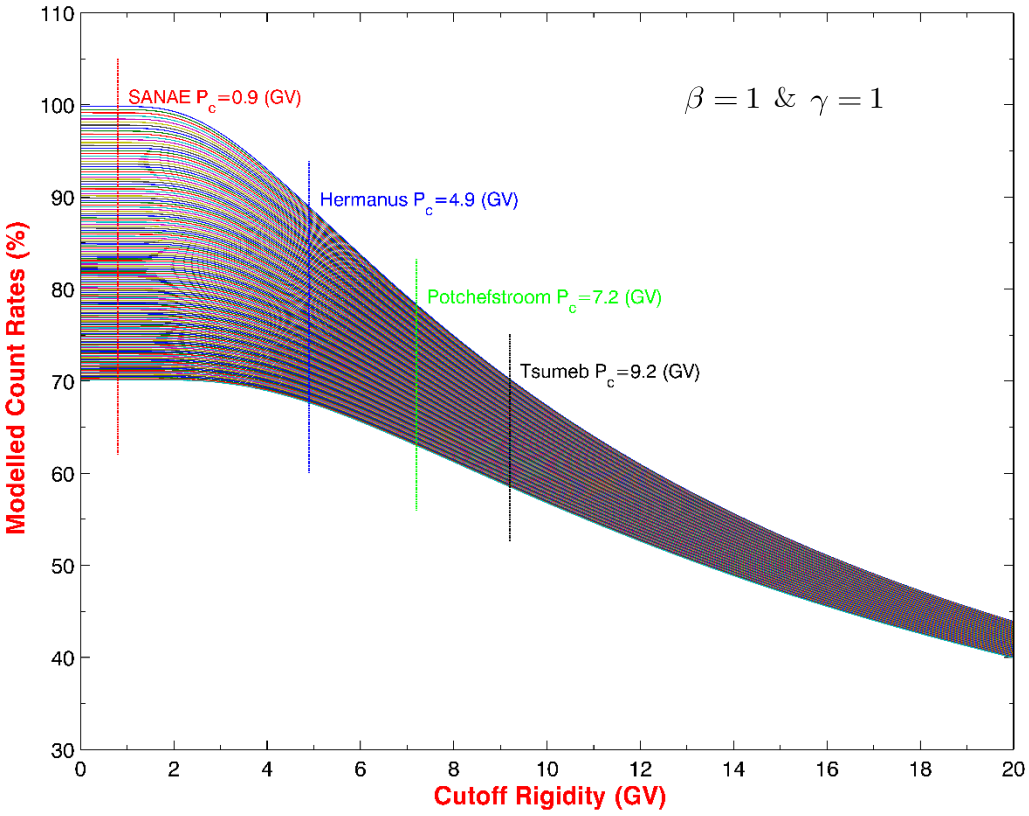

Figure 5.5: Example of the modelled count rate values of $N(\mathrm{P_c}, x, t)$ as function of cutoff rigidity, $\mathrm{P_c}$, for different chosen values of $\Delta\phi$ from 0 (top curve) to 1.5 GV (bottom curve).

Now, the chosen values of $\Delta\phi$ from Figure 5.5 are plotted as a function of the modelled count rates of $N(\mathrm{P_c}, x, t)$ at different cutoff rigidities, $\mathrm{P_c}$ (similar to Figure 5.3). The solid lines in Figure 5.6 represent a polynomial fit function of the order three, similar to equation 5.8. The polynomial coefficients of this fit function are given in Table 5.6 with 95 % confidence bounds.

Similar to the Convection-Diffusion approximation, the polynomial equation 5.8 (whose coefficients are in Table 5.6) together with the measured count rates of neutron monitors were used. These count rates of neutron monitors were normalized to 100 % in March 1987, as mentioned

before. The modulation parameter $\Delta\phi$ is plotted as a function of time in Figure 5.7.

Table 5.6: Coefficients with 95 % confidence bounds in brackets.

Coefficients		
P_c	a	b
08	-1.148e-05 (-1.166e-05, -1.129e-05)	0.003811 (0.003763, 0.003858)
4.9	-1.591e-05 (-1.61e-05, -1.571e-05)	0.004827 (0.004782, 0.004873)
7.2	-2.41e-05 (-2.433e-05, -2.387e-05)	0.00667 (0.006621, 0.006718)
9.2	-3.567e-05 (-3.595e-05, -3.539e-05)	0.009046 (0.008992, 0.009101)
P_c	c	d
08	-0.4472 (-0.4512, -0.4433)	18.09 (17.98, 18.21)
4.9	-0.5324 (-0.5359, -0.5289)	20.36 (20.27, 20.46)
7.2	-0.6786 (-0.682, -0.6752)	23.83 (23.75, 23.91)
9.2	-0.849 (-0.8525, -0.8455)	27.37 (27.3, 27.45)

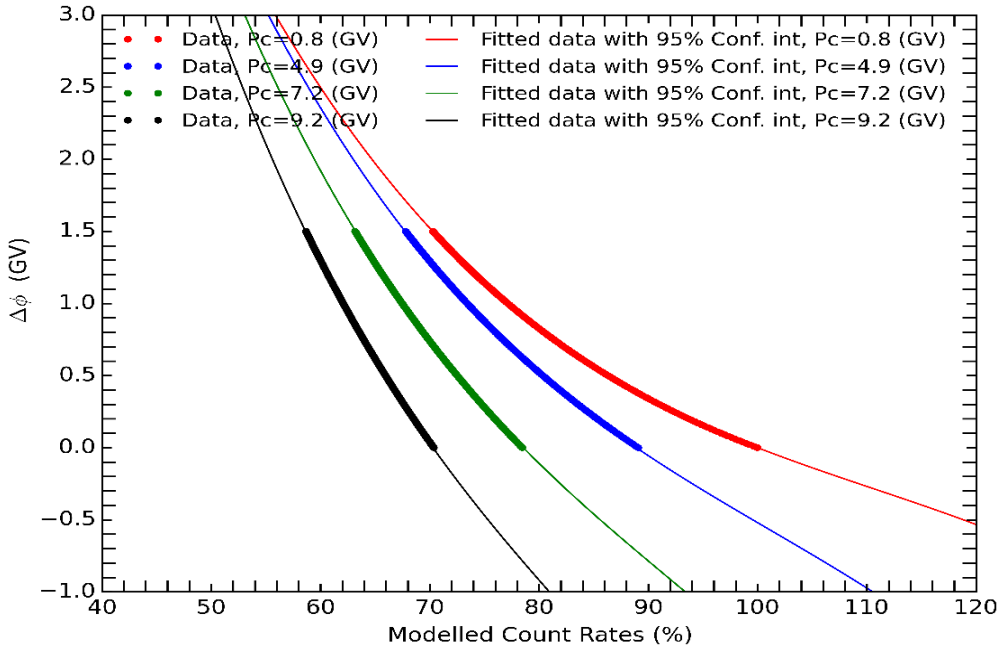

Figure 5.6: Modulation parameter $\Delta\phi$ as function of the modelled count rate $N(\mathrm{P}_c,\ x,\ t)$. The solid lines represent a polynomial of the order three similar to that of equation 5.8.

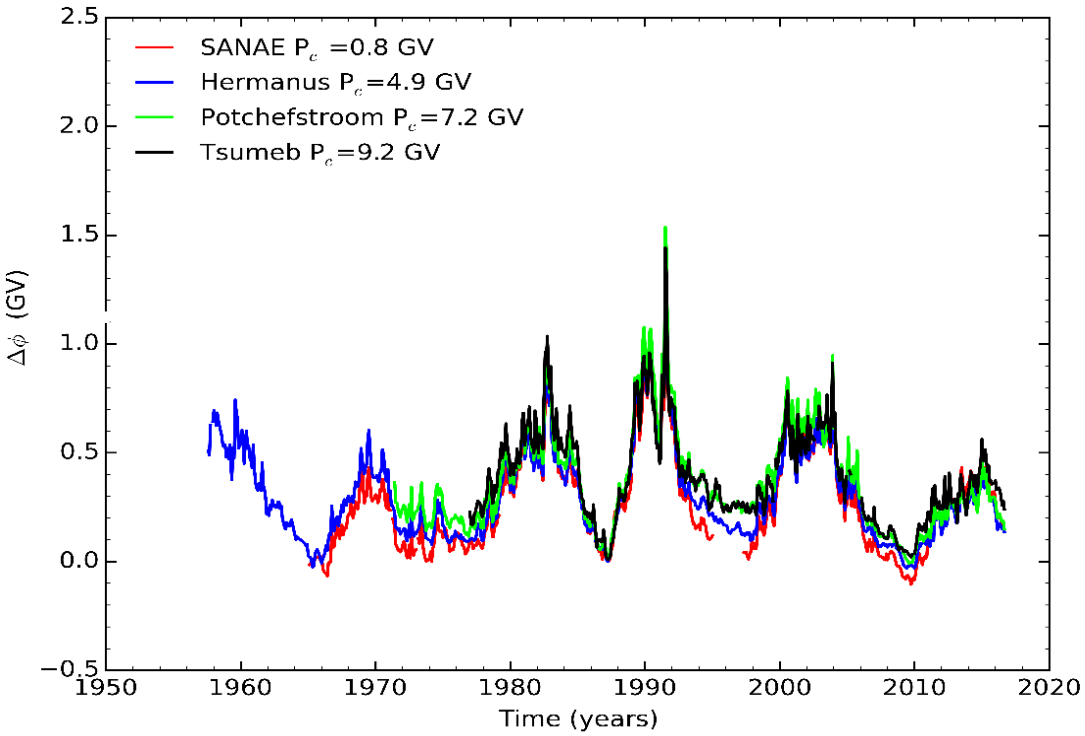

Figure 5.7: Calculation of $\Delta\phi$ using neutron monitor data from July 1957 to October 2016.

5.3 Comparison of the calculated modulation parameters

The modulation parameters $\Delta\phi(r_{t_1},\ t_1,\ r_{t_2},\ t_2)$ and $M^*(r_{t_1},\ t_1,\ r_{t_2},\ t_2)$ are now compared using equation 5.11. These parameters were formulated between two specific times, where one of them is chosen to be March 1987 and the other one is any other time. In March 1987

$$\frac{\phi(r_{t_{87}},\ t_{87})}{\kappa_2(\mathrm{P},\ t)} = \beta^{\eta}\,\frac{M(r_t,\ t_{87})}{3}, \tag{5.16}$$

and at any other time

$$\frac{\phi(r_t,\ t)}{\kappa_2(\mathrm{P},\ t)} = \beta^{\eta}\,\frac{M(r_t,\ t)}{3}. \tag{5.17}$$

The difference between equation 5.16 and 5.17 is

$$\frac{\phi(r_{t_{87}},\ t_{87}) - \phi(r_t,\ t)}{\kappa_2(\mathrm{P},\ t)} = \beta^{\eta}\,\frac{M(r_{t_{87}},\ t_{87}) - M(r_t,\ t)}{3}, \tag{5.18}$$

or

$$\frac{\Delta\phi(r_{t_1},\ t_1,\ r_{t_2},\ t_2)}{\kappa_2(\mathrm{P},\ t)} = \beta^{\eta}\,\frac{\Delta M(r_{t_1},\ t_1,\ r_{t_2},\ t_2)}{3}. \tag{5.19}$$

In equation 4.19 it was shown that

$$\Delta M(r_{t_1},\ t_1,\ r_{t_2},\ t_2) = \frac{M^*(r_{t_1},\ t_1,\ r_{t_2},\ t_2)}{\beta^{\eta}\kappa_2(\mathrm{P},\ t)}. \tag{5.20}$$

Substituting equation 5.20 into 5.19 gives

$$\Delta\phi = \frac{M^*}{3}. \tag{5.21}$$

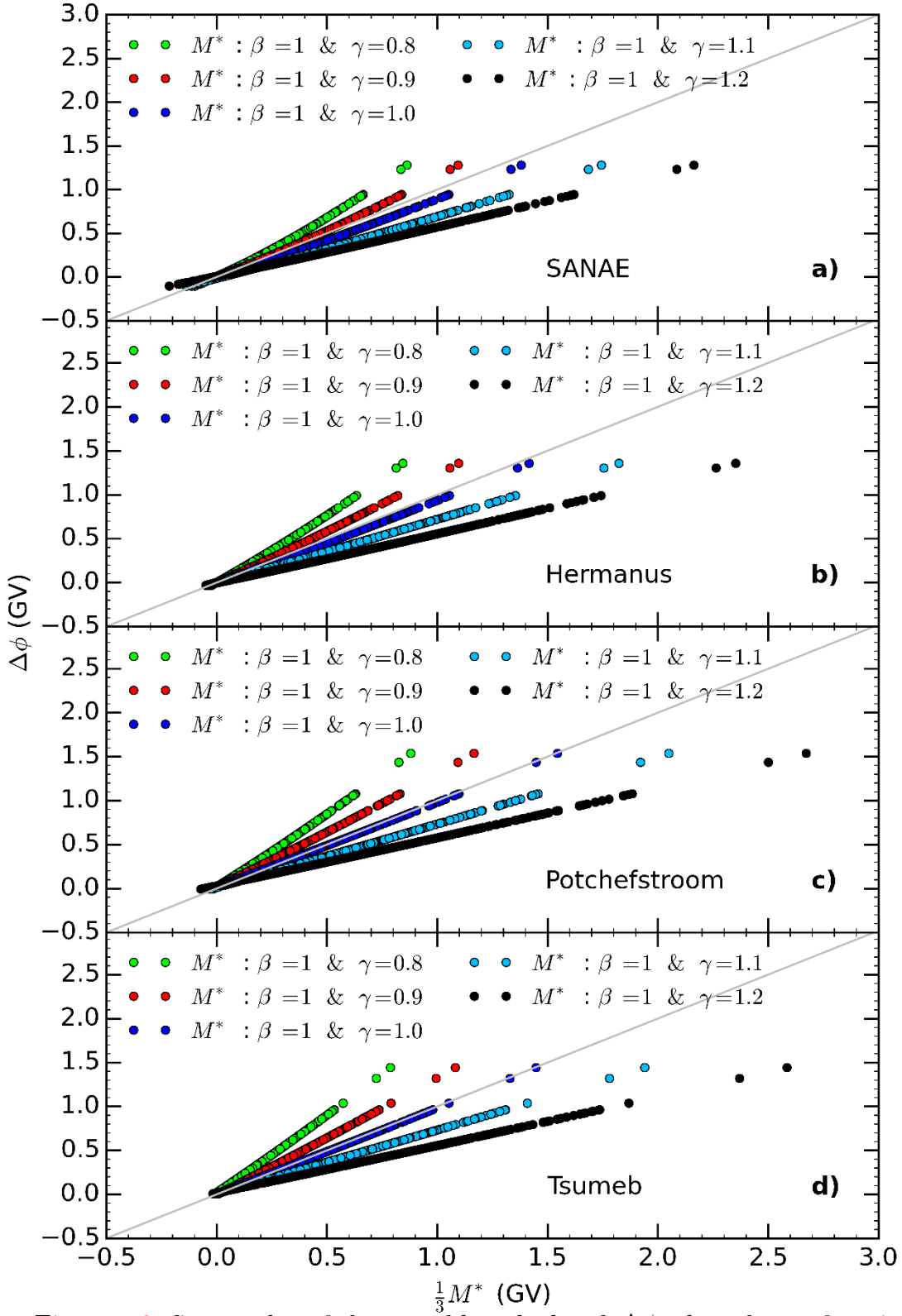

Figure 5.8: Scatterplot of the monthly calculated $\Delta\phi$ plotted as a function of M^* / 3 for each station. The grey reference line denotes a direct proportionality

Figure 5.8 shows a scatterplot of the calculated values of $\Delta\phi$ as a function of $M^* / 3$ for all four stations. In all panels, i.e. panels (a), (b), (c) and (d), $M^* / 3$ is calculated when the diffusion coefficient parameters of $\kappa(r_t, \mathrm{P}, t)$ given in equation 4.6, i.e. $\beta = 1$ while $\eta = 1$ and γ takes 0.8, 0.9, 1.0, 1.1 and 1.2 are chosen for each station. $\Delta\phi$ as a function of time is calculated when the diffusion coefficient parameters of $\kappa(r_t, \mathrm{P}, t)$ given in equation 4.6, i.e. $\beta = 1$ while $\eta = 1$ and $\gamma = 1$ are chosen for each station.

In all panels the diagonal lines are shown to guide the eye. An almost direct proportionality is seen in panels (b), (c) and (d) for $\gamma = 1$. However, in panel (a) for SANAE, a value of γ somewhere between 0.9 and 1.0 for M^* and $\gamma = 1$ for $\Delta\phi$ is required. This means that the Convection-Diffusion approximation and the Force-Field approximation are equivalent through equation 5.21 for these values of the parameters for $\kappa(\mathrm{P}, t)$. Therefore, the appropriate value of γ referred to in Section 5.2.1 is approximately 1.

5.4 Summary

In this chapter, the diffusion coefficient parameters were discussed based on the obtained results from the calculated modulation parameters using neutron monitor data. Detailed calculations of the monthly values of the modulation parameters, using both the Convection-Diffusion approximation and the Force-Field approximation, were discussed.

This chapter showed how to calculate the Convection-Diffusion modulation parameter between two specific times by using a procedure that does not depend on the yield function or the LIS. A relationship between the modulation parameters, the count rates and cutoff rigidity were obtained from the plotted figures. It was shown that the value of γ

that enters into the diffusion coefficients as the exponent of the rigidity, plays a major role in the calculation of the time-dependent modulation parameters using neutron monitor data.

It was shown that modulation parameters calculated for the Convection-Diffusion model and for the Force-Field model follow the theoretical relationship for neutron monitors at Hermanus, Tsumeb and Potchefstroom for the standard form of the diffusion coefficient chosen here, but not the low-cutoff monitor at SANAE. This suggests that the chosen rigidity dependence may have to be reconsidered.

Chapter 6

Calculation of modulation parameters using space-borne detector measurements

6.1 Introduction

The availability of cosmic-ray data from space-borne detectors is very useful and helpful to understand long-term modulation. In this chapter, the modulation parameters are calculated with reference to LIS intensities. These modulation parameters are described by the modulation parameters $\phi^{\mathrm{R}}(r_{t_{87}},\ t_{87})$ and $M^{\mathrm{R}}(r_{t_{87}},\ t_{87})$ in equations 4.42 and 4.25, respectively.

This chapter commences with a discussion of the intensity measurements by IMP - 8, PAMELA and Voyager - 1 missions described in chapter 3. A new parameterization of the LIS will be presented based on data from PAMELA and Voyager - 1. The spectra approximations presented in sections 4.6 and 4.9 will be used to fit data and calculate the modulation parameters. At the end of this chapter a brief summary is given.

6.2 Data from space-borne detectors

Measurements of cosmic-ray protons performed during quite different heliospheric conditions were chosen, by Voyager - 1, IMP - 8 and PAMELA detector. Sections 6.2.1 to 6.2.3 discuss data from these missions and how these data were used in the calculation of modulation parameters.

6.2.1 Voyager - 1 measurements

Currently, 2016, the Voyager - 1 spacecraft is at a distance of about 135 AU from earth. Figures 6.1 and 6.2 give a brief outline on how the intensity of helium and of cosmic-ray nuclei ($>$ 70 MeV) on Voyager - 1 have changed throughout its mission towards the boundary of the heliosphere.

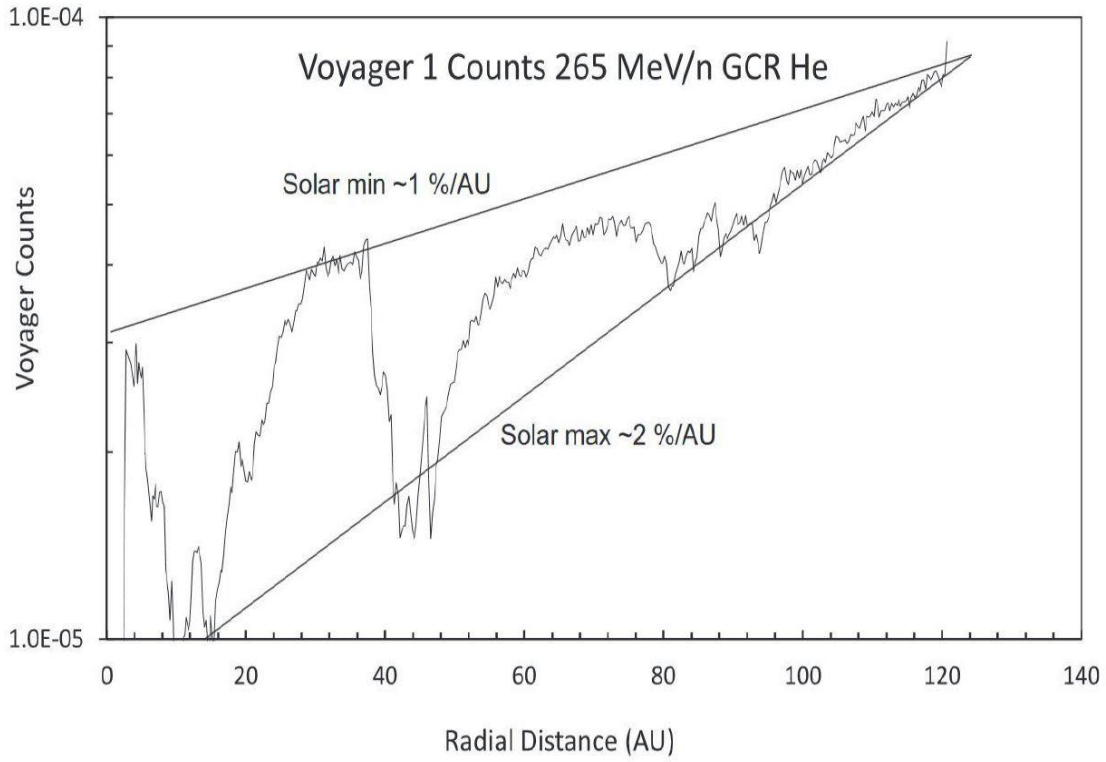

Figure 6.1: Voyager - 1 count rates for helium as a function of heliocentric radial distance, displaying the 11-year solar cycle. Source: *Moraal* (2014).

The intensity-cycle of helium is clearly visible in Figure 6.1, with three cosmic-ray intensity maxima observed corresponding to the solar minima in 1977, 1987 and 1998. These count rates were recorded as a function of heliocentric radial distance towards the boundary of the heliosphere. The two lines show that the radial gradients are of the order of 1 %/AU at solar minimum and during solar maximum it is of the order of 2 %/AU (*Moraal*, 2014). It is noteworthy to see that there is little indication of a

modulation cycle or a cosmic-ray maximum in 2009 at 113 AU in the heliosheath. This is probably due to the fact that the subsonic solar wind speed drops off there, so that the fluctuations in the heliospheric magnetic field that cause modulation are less effective. Although not shown, the proton intensities also increased throughout its mission towards the LISM and cosmic-ray intensity cycles were also observed.

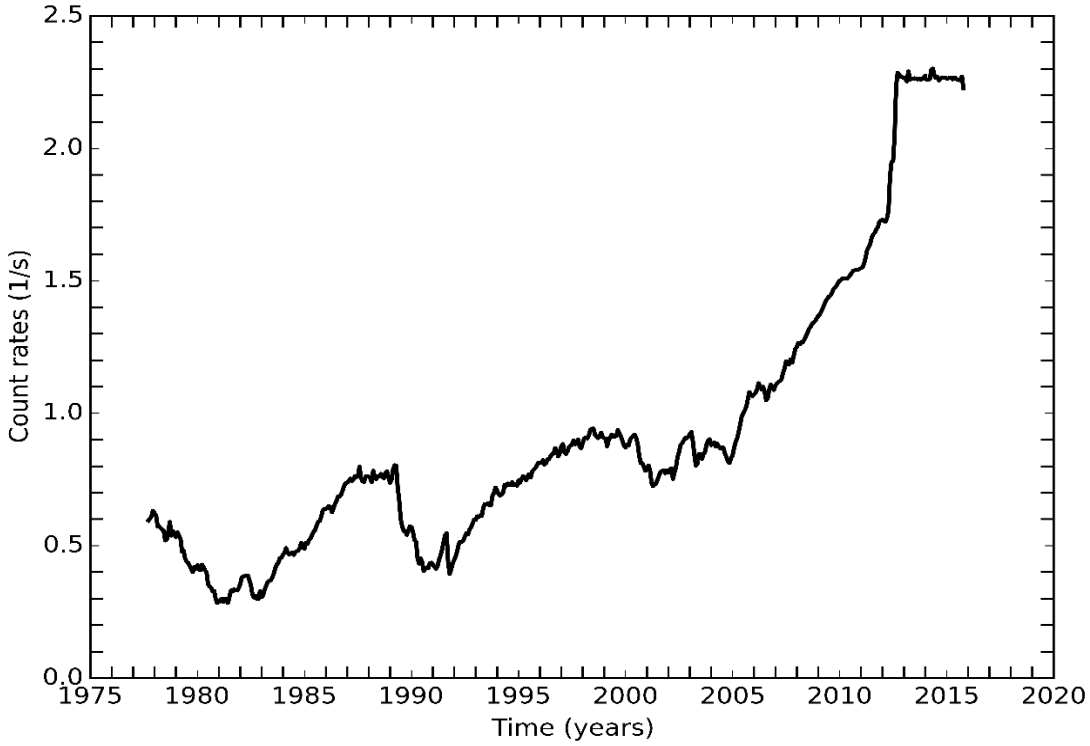

Figure 6.2: Voyager - 1 count rates (26-day averages) for the integral rates of $>$ 70 MeV nuclei as a function of time. Data source: *http //Voyager.gsfc.nasa.gov/.*

In Figure 6.2, the average integral rates of galactic cosmic-ray nuclei $>$ 70 MeV were detected as a function of time towards the boundary of the heliosphere. While Voyager - 1 was in the heliosheath in 2009, it measured the highest ever count rate compared with all the years before 2009. Since 2009 the measured count rates increased and stopped increasing on the 25th of August 2012. In 2012, the total increase of the count rate before the 7th of May 2012 and after the 25th of August 2012

was about 32 %. After the 25th of August 2012, the count rates remained essentially constant, strongly suggesting that the spacecraft is actually sampling the LISM. Also seen in Figure 6.2 are intensity cycles with three maxima related to the times of solar minimum in 1977, 1987 and 1998. Several papers have been published on these measurements, e.g. *Krimigis et al.* (2013), *Stone et al.* (2013), *Webber* and *McDonald* (2013), *Webber* and *Intriligator* (2014) and *Senanayake et al.* (2015).

In section 6.3, Voyager - 1 proton differential intensity in units of particles·m^{-2}·s^{-1}·sr^{-1}·MeV^{-1} is given as a function of kinetic energy. These proton data measurements were adopted from *Stone et al.* (2013) Figure 3 and the other data from *Webber* and *McDonald* (2013) Figure 2. These intensities will be revisited later, as it will be important when it comes to the parameterization of the proton LIS used in this study.

6.2.2 The IMP - 8 proton measurements

Other space-borne measurements used in this study are from the IMP - 8 satellite at 1 AU. Figure 6.3 shows the count rates of protons as measured by IMP - 8 (dark line) and Voyager - 1 (light line), respectively. By comparing the two graphs, it is evident that the amplitude of the solar cycle intensity-variation depends on radial position. Prior to the 1980s, the count rate variation between the two was significantly small. However, Voyager - 1 count rates after the 1980s increased by approximately 2 % per year compared with IMP - 8. The maximum count rate of about 0.55 per second for IMP - 8 at 1 AU and about a 0.78 count per second for Voyager - 1 at 70 AU were reached towards the end of 1998.

When repeating the calculation of the modulation parameters described in section 6.6.2 and 6.7.2, the proton IMP - 8 data are for kinetic energy

ranging from 0.0265 to 0.406 GeV per nucleon. These energies correspond to the differential intensities between 0.251 and 2.253 in units of particles·m^{-2}·s^{-1}·sr^{-1}·MeV^{-1}. These data were measured from February to October 1987 and were adopted from *Caballero-Lopez et al.* (2004).

The IMP - 8 data were chosen for the solar minimum of 1987, a year in which a neutron monitor latitude survey was conducted (*Moraal et al.*, 1989).

One would therefore expect both spacecraft data and neutron monitor data in 1987 to reflect the same modulation conditions and therefore be described by the same modulation parameters. As mentioned before, March 1987 was used to normalize all measured count rates of neutron monitors chosen in this study to the same value.

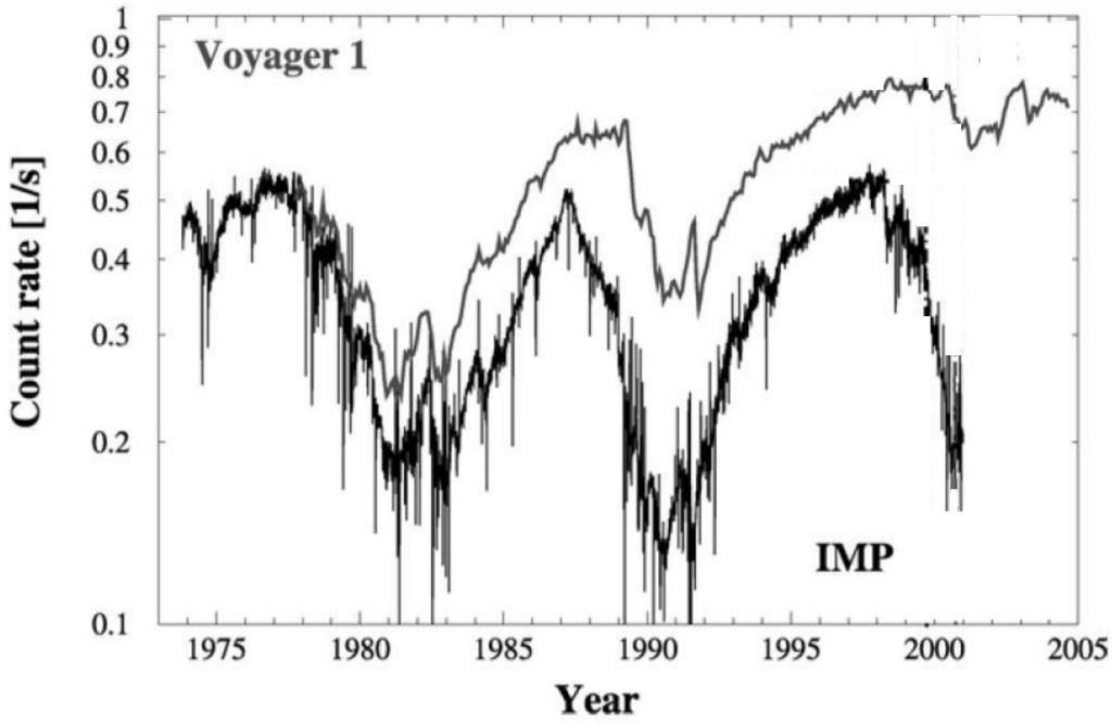

Figure 6.3: Voyager - 1 proton count rate is compared with the IMP - 8 proton count rate. Source: *Heber* and *Potgieter* (2006).

6.2.1 PAMELA proton measurements

Equally important for heliospheric studies at 1 AU is the PAMELA satellite-borne experiment detection of high energy particles. PAMELA operated from late 2006 to late 2009. Measurements from January to March 2008 were chosen because at neutron monitor energies, the count rates for the chosen neutron monitors in 2008 were close to 100 % on average similar to the March 1987 normalized count rate. The 2009 solar minimum itself was quite different from the one in 1987, as discussed in several publications including that of *Adriani et al.* (2011) whose datasets were used in this study. The measurements used were given as a function of kinetic energy ranging from 1 to 100 in units of GeV per nucleon. Differential intensity varied between 4.63×10^{-5} and 1.11 in units of particles·m^{-2}·s^{-1}·sr^{-1}·MeV^{-1}.

6.3 Parameterization of the proton LIS

Over the years, many LIS models have been proposed, based on fits to data from ionization chamber experiments to spacecraft measurements, or numerical simulations like the GALPROP models. The lack of a low energy measurement of the LIS has always been a problem for the calculation of the modulation parameters. However, in 2012, Voyager - 1 is believed to have crossed the heliopause and now it is in the interstellar space. Since then, the cosmic-ray intensity measured by Voyager - 1 has remained constant, strongly suggesting that this spacecraft is actually sampling the LIS, as mentioned in section 6.2.1.

Using three dataset measurements from Voyager - 1, adopted from *Stone et al.* (2013) and *Webber* and *McDonald* (2013) and the 2008 PAMELA data from *Adriani et al.* (2011), a precise picture of the proton

LIS at very low and high energies can be obtained. The proton intensity data from these spacecraft are given in Table 6.1. Figure 6.4 shows the measured cosmic-ray proton LIS Voyager - 1 in the energy range between 0.034 and 0.5623 in units of GeV per nucleon. These energies correspond to differential intensity between 27.1 and 6.5 particles·m^{-2}·s^{-1}·sr^{-1}·MeV^{-1}. At the high energy end, the spectrum is constrained by PAMELA measurements at 1 AU in the energy range between 1 and 100 in units of GeV per nucleon. These energies correspond to differential intensity between 1.11 and 4.63×10^{-5} particles·m^{-2}·s^{-1}·sr^{-1}·MeV^{-1}.

Table 6.1: Voyager - 1 and PAMELA proton data. All energies are in GeV per nucleon and all intensities in particles·m^{-2}·s^{-1}·sr^{-1}·MeV^{-1}.

Voyager - 1 *Stone et al.* (2013)		Voyager - 1 *Webber* and *McDonald* (2013)		PAMELA *Adriani et al.* (2011)	
Energy	Intensity	Energy	Intensity	Energy	Intensity
0.034	27.1	0.1442	19	1	1.11
0.043	26	0.1644	19	1.5	0.674
0.049	25.8	0.1825	16.7	2	0.475
0.08	23	0.208	15.3	3	0.256
0.139	19.4	0.231	13.5	4	0.149
0.16	18.1	0.2434	12.9	6	0.0672
0.175	16.9	0.3081	10	10	0.0215
0.2	15	0.3798	9.6	20	0.00379
0.233	13.6	0.4561	8.8	30	0.0013
0.3	10.7	0.5623	6.5	40	0.000592
-	-	-	-	60	0.000193
-	-	-	-	80	0.0000888
-	-	-	-	100	0.0000463

A double power law equation was used to parameterize the shape of the proton LIS from these data points. The formalism of this equation is the same as the one used by *Caballero-Lopez* and *Moraal* (2012) equation 2. This proton LIS parameterization in terms of rigidity is given as

$$j^{\text{Proton}}_{\text{P, LIS}}(\text{P}_{\text{LIS},\,t},\, t) = j_0(\text{P}_0^{\alpha} + \text{P}^{\alpha})^{(\gamma_1-\gamma_2)/\alpha}\text{P}^{\gamma_2}, \tag{6.1}$$

where P is the rigidity in GV and j_0, P_0, α, γ_1 and γ_2 are constants. In terms of kinetic energy, equation 6.1 can be written as

$$j^{\text{Proton}}_{\text{T, LIS}}(\text{T},\, t) = j_0(\text{P}_0^{\alpha} + (\text{T}(\text{T}+2\text{E}_0))^{\alpha/2})^{(\gamma_1-\gamma_2)/\alpha}(\text{T}(\text{T}+2\text{E}_0))^{\gamma_2/2}, \tag{6.2}$$

where T is the kinetic energy per nucleon and E_0 is the rest-mass energy. The constants, j_0, P_0, α, γ_1 and γ_2, are given in Table 6.3.

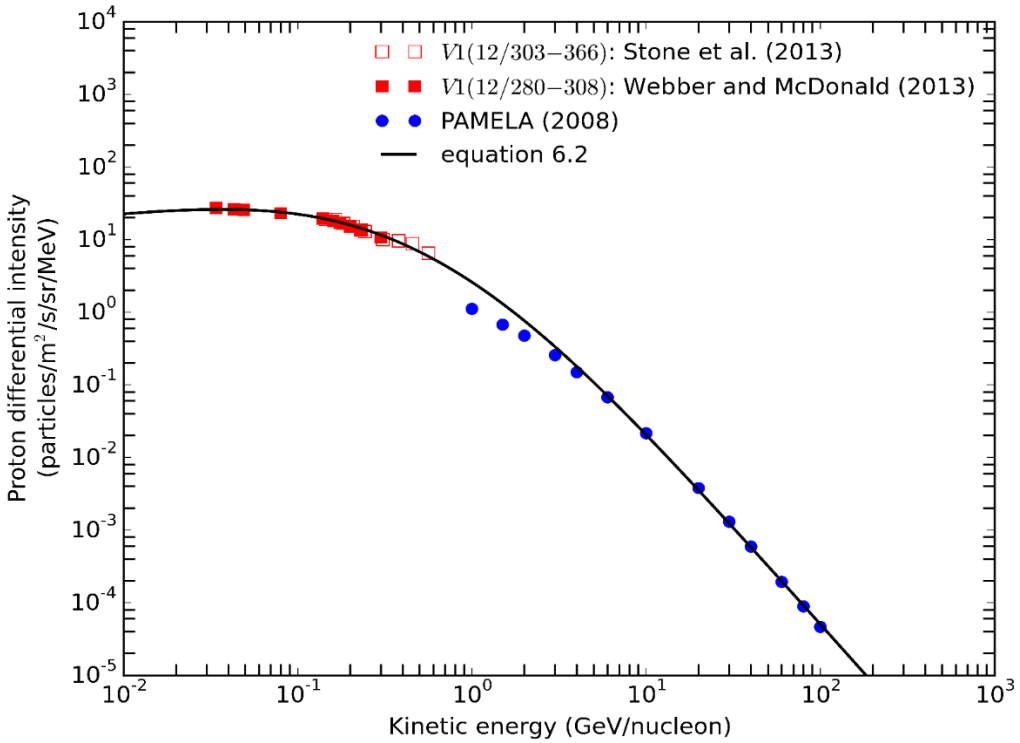

Figure 6.4: The proton LIS (solid black line) obtained from Voyager - 1 data (Source: *Stone et al.*, 2013 (hollow red squares) and *Webber* and *McDonald*, 2013 (filled red squares)) and the 2008 PAMELA data (Source: *Adriani et al.*, 2011 (blue circles)).

Table 6.2: IMP - 8 and PAMELA proton data, all energies are in GeV per nucleon and all intensities in particles·m^{-2}·s^{-1}·sr^{-1}·MeV^{-1}.

IMP - 8 *Caballero-Lopez et al.* (2004)		PAMELA *Adriani et al.* (2011)	
Energy	Intensity	Energy	Intensity
0.0265	0.2511	1	1.11
0.0358	0.3408	1.5	0.674
0.047	0.4518	2	0.475
0.0571	0.5293	3	0.256
0.0721	0.6443	4	0.149
0.114	1.175	6	0.0672
0.138	1.28	10	0.0215
0.166	1.335	20	0.00379
0.204	1.34	30	0.0013
-	-	40	0.000592
-	-	60	0.000193
-	-	80	0.0000888
-	-	100	0.0000463

In Figure 6.4, equation 6.2 is represented by a solid black line from 0.01 to 120 GeV per nucleon. Voyager - 1 data from *Stone et al.* (2013) are represented by the hollow red squares in the figure while data from *Webber and McDonald* (2013) are represented by the filled red squares. PAMELA data in the figure are represented by the blue circles. As can be seen in the figure, data measured by Voyager - 1 at 121 AU and by PAMELA at 1 AU do not overlap well in energy. The figure shows that equation 6.2 does not fit data between 1 and 6 GeV per nucleon. This is of course expected because cosmic-ray particles with energies below 10 GeV per nucleon are subjected to modulation at 1 AU. To fit data in this energy

range, two approximate solutions of the full Parker transport equation will be used in this study together with a double power law equation.

6.4 Parameterization of the modulated proton spectrum

In this section, three parameterizations of the cosmic-ray spectra are performed where two of those use the LIS parameterization of equation 6.2 and one uses a double power law equation. These parameterizations are used to fit the proton intensities measured by IMP - 8 and PAMELA. Data of these proton intensities are given in Table 6.2. PAMELA data are repeated from Table 6.1 for ease of reference.

6.5 The double power law spectrum parameterization

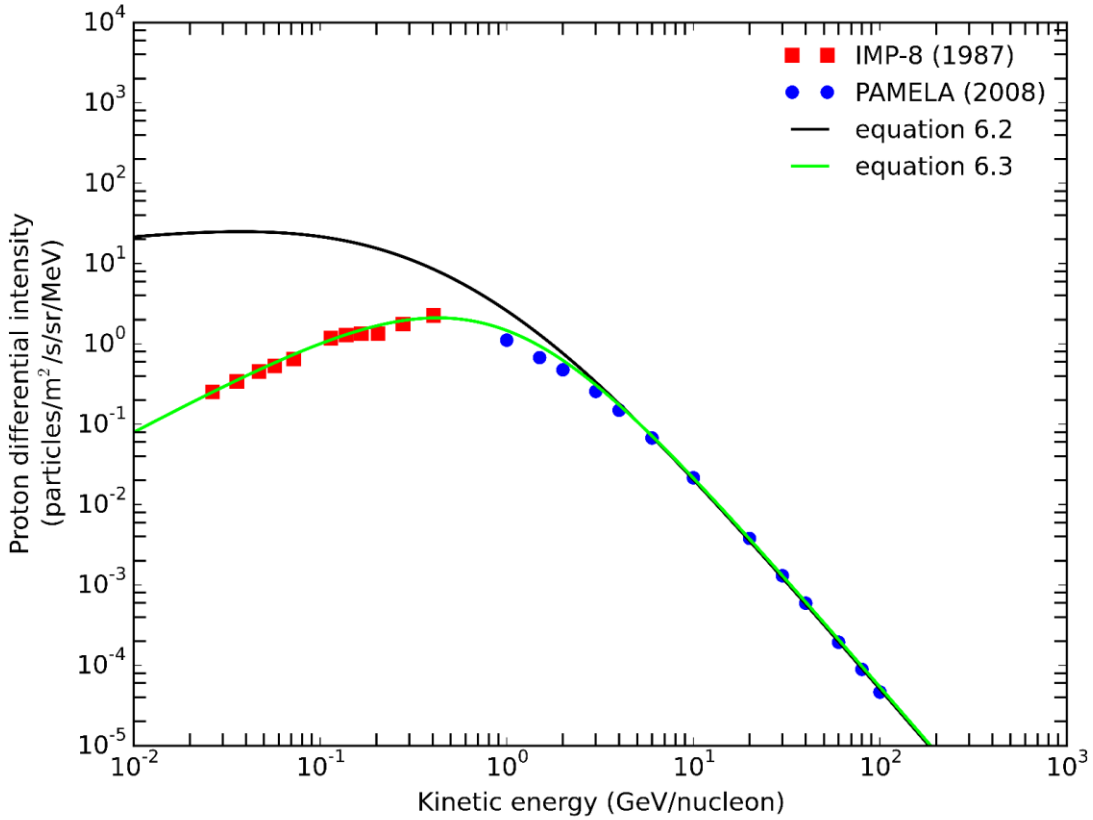

Figure 6.5: The proton IMP - 8 (red squares) and PAMELA (blue circles) data is plotted together with equation 6.2 (black line) and equation 6.3 (green line).

Figure 6.5 shows data points of IMP - 8 at 1 AU during the solar minimum time of 1987 (red squares) and PAMELA at 1 AU measurements during 2008 (blue circles). The proton double power law parameterization equation in terms of energy as in equation 6.2 was used to fit these data points, i.e.

$$j^{\text{Proton}}_{\text{T, DPL}}(\text{T}_{t_{87}}, t_{87}) = j_0(\text{P}_0^{\alpha} + (\text{T}_{t_{87}}(\text{T}_{t_{87}} + 2\text{E}_0))^{\alpha/2})^{(\gamma_1-\gamma_2)/\alpha}(\text{T}_{t_{87}}(\text{T}_{t_{87}} + 2\text{E}_0))^{\gamma_2/2}, \quad (6.3)$$

where the constants, j_0, P_0, α, γ_1 and γ_2 are given in the last raw of Table 6.3.

Table 6.3: Parameters for the double power law equations used in this study

Function	Constants				
	j_0	P_0	α	γ_1	γ_2
Equation 6.2	13.792	0.60	2.0	–2.73	0.49
Equation 6.3	13.792	1.03	2.0	–2.73	0.49

The figure shows the calculated fit for LIS intensities (solid black line) and intensities at 1 AU (solid green line) between 0.01 and 120 GeV per nucleon. However, while the fit to data is quite good, the expression has no physical significance and does not explain how the modulation occurs. Therefore, the following sections repeat this fit to data at 1 AU using two approximate solutions from the full Parker transport equation, and in section 6.8 all these fits are compared.

6.6 The Convection-Diffusion approximation approach

This section describes how the Convection-Diffusion approximation is used to fit data and calculate the modulation parameters at all rigidities.

6.6.1 The Convection-Diffusion intensity spectrum approximation

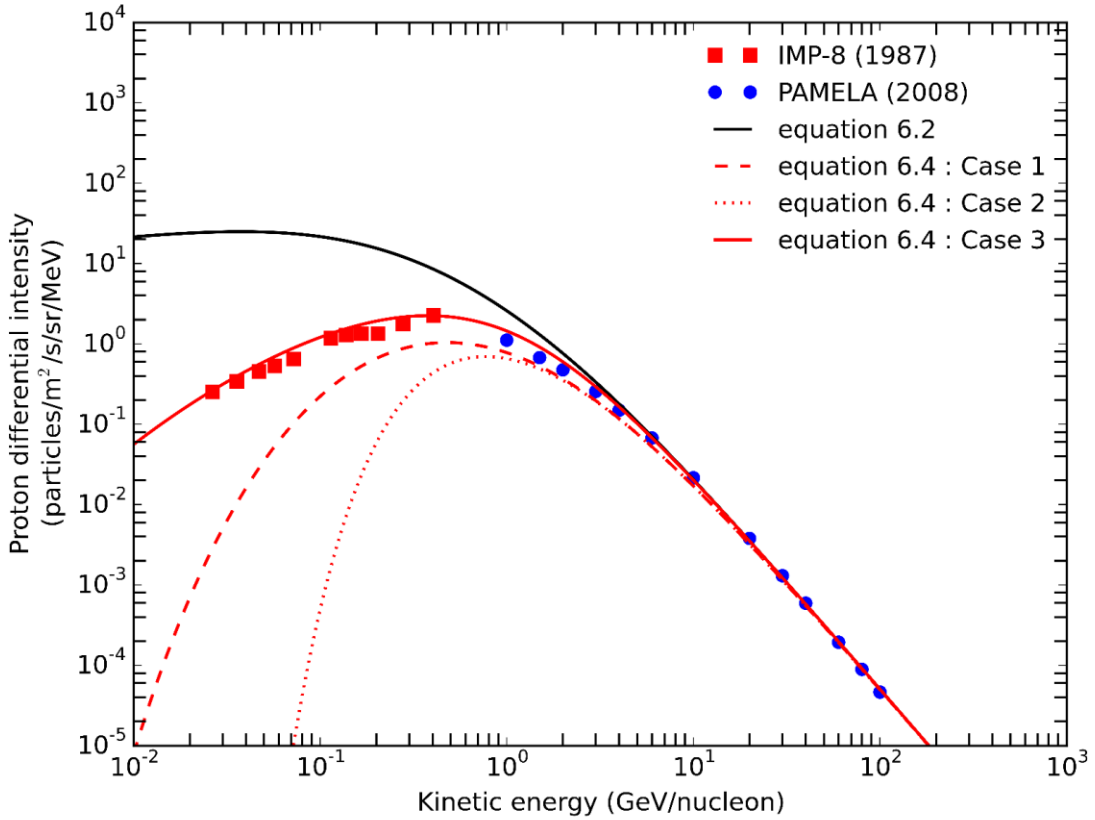

Figure 6.6: Proton data from IMP - 8 (red squares) and PAMELA (blue circles) are plotted together with equation 6.4 using three different combinations of β, η and γ.

In section 4.6, a detailed formulation of this approximation was given. In terms of rigidity this is

$$j^{\text{Proton}}_{\text{P, CD}}(r_{t_{87}}, \text{P}, t_{87}) = j^{\text{Proton}}_{\text{P, LIS}}(r_{\text{LIS}}, \text{P}, t_{87})\, e^{-M(r_{t_{87}}, t_{87})}, \tag{6.4}$$

where

$$M(r_{t_{87}}, t_{87}) = \frac{\text{V}}{\kappa(r_{t_{87}}, \text{P}, t_{87})}(r_{\text{LIS}} - r_{t_{87}}). \tag{6.5}$$

Here, $M(r_{t_{87}}, t_{87})$ is the modulation function and $j^{\text{Proton}}_{\text{P, LIS}}(r_{\text{LIS}}, \text{P}, t_{87})$ is given by equation 6.2. The values chosen to fit the measured IMP - 8 and PAMELA data at 1 AU were the solar wind speed $\text{V} = 400$ km·s^{-1} and the diffusion coefficient parameter $\kappa(r_{t_{87}}, \text{P}, t_{87}) = 4.38\times10^{12}\beta^{\eta}\text{P}_0^{(1-\gamma)}\text{P}^{\gamma}$ km^2·s^{-1}. Here β is given by equation 4.10. In the outer heliosphere, equation 6.4 gives better results when the LIS boundary is chosen to be $r_{\text{LIS}} = 150$ AU, according to *Moraal* (2011).

To fit the proton intensities measured by IMP - 8 and PAMELA using equation 6.4, certain parameters have to be carefully adjusted in the diffusion coefficient $\kappa(r_{t_{87}}, \text{P}, t_{87})$. The η and γ in the diffusion coefficient parameters are free parameters. These parameters are varied to obtain results compatible with measurements. The effect of η and γ on these measured intensities at 1 AU are shown in Figure 6.6. In this figure, the black solid line represents the LIS intensities (equation 6.2). Equation 6.4 is plotted for different combinations η, β, and γ, namely

i) If $\eta = 1$, $\beta = 1$ and $\gamma = 1$ are chosen, denoted by Case 1, equation 6.4 does not fit IMP - 8 data (see the red dashed line). This combination of η, β, and γ was also tested by *Caballero-Lopez* and *Moraal* (2004) using the *Webber* and *Lockwood* (2001) LIS parameterization at $r_{\text{LIS}} = 90$ AU to fit IMP - 8 data and it also did not fit.

ii) If $\eta = 1$, $\beta \neq 1$ and $\gamma = 1$ are chosen as Case 2, the equation also does not fit IMP - 8 data and it progressively gets worse than Case 1 (see the red dotted line).

iii) However, a combination of $\eta = -3/2$, $\beta \neq 1$ and $\gamma = 2$ for Case 3, fits IMP - 8 data (see the red solid line). This case is chosen for further analysis and calculations.

The three cases presented here show that, to fit IMP - 8 data using equation 6.4, the diffusion coefficient parameters of $\kappa(r_{t_{87}}, \mathrm{P}, t_{87})$ have to be modified from the widely used $\eta = 1$, $\beta = 1$ and $\gamma = 1$. Note that the fit equation can also change if a different solar wind speed or radial boundary distance is chosen.

6.6.2 Calculation of the modulation parameter $M^{\mathrm{R}}(r_{t_{87}}, t_{87})$

As mentioned in section 4.6, the spectrum in terms of intensity is useful to compare with observations while theoretically it is more useful to work with distribution functions. To do that, the experimental measured intensities have to be divided by the squared rigidity (see equation 4.11).

The distribution function calculated from the measured proton intensities at the LIS is

$$f_{\mathrm{LIS}}^{\mathrm{Proton}}(r_{\mathrm{LIS},\,t_{87}},\,\mathrm{P}_{\mathrm{LIS},\,t_{87}},\,t_{87}) = \frac{j_{\mathrm{P,\,LIS}}^{\mathrm{Proton}}(r_{\mathrm{LIS},\,t_{87}},\,\mathrm{P}_{\mathrm{LIS},\,t_{87}},\,t_{87})}{\mathrm{P}^2_{\mathrm{LIS},\,t_{87}}} = j_0(\mathrm{P}_0^{\alpha} + \mathrm{P}^{\alpha}_{\mathrm{LIS},\,t_{87}})^{(\gamma_1-\gamma_2)/\alpha}\mathrm{P}^{\gamma_2-2}_{\mathrm{LIS},\,t_{87}}. \tag{6.6}$$

At earth the distribution function calculated from the proton double power law equation is

$$f_{\mathrm{DPL}}^{\mathrm{Proton}}(r_{t_{87}},\,\mathrm{P},\,t_{87}) = \frac{j_{\mathrm{P,\,DPL}}^{\mathrm{Proton}}(r_{t_{87}},\,\mathrm{P},\,t_{87})}{\mathrm{P}^2} = j_0(\mathrm{P}_0^{\alpha} + \mathrm{P}^{\alpha})^{(\gamma_1-\gamma_2)/\alpha}\mathrm{P}^{(\gamma_2-2)}, \tag{6.7}$$

and for the Convection-Diffusion approximation

$$f_{\mathrm{CD}}^{\mathrm{Proton}}(r_{t_{87}},\,\mathrm{P},\,t_{87}) = \frac{j_{\mathrm{P,\,CD}}^{\mathrm{Proton}}(r_{t_{87}},\,\mathrm{P},\,t_{87})}{\mathrm{P}^2} = f_{\mathrm{LIS}}^{\mathrm{Proton}}(r_{\mathrm{LIS}},\,\mathrm{P},\,t_{87})\,\mathrm{e}^{-M(r_{t_{87}},\,t_{87})}. \tag{6.8}$$

The distribution functions from the double power law parameterization (equation 6.7) and Convection-Diffusion approximation (equation 6.8) at 1 AU are shown in Figure 6.7. In this figure, the black, red and green solid lines represent equation 6.6, 6.7 and 6.8, respectively. The proton measured intensities from IMP - 8 (red squares) and PAMELA (blue circles) were also converted to distribution functions.

According to modulation theory (see equation 4.25), the rigidity dependent modulation parameter is given as

$$M^{\mathrm{R}}(r_{t_{87}},\ t_{87}) = \beta^{\eta}\,\frac{\mathrm{P}^{\gamma}}{\mathrm{P}_0^{(\gamma-1)}}\ln\left(\frac{f_{\mathrm{LIS}}^{\mathrm{Proton}}(r_{\mathrm{LIS}},\ \mathrm{P},\ t_{87})}{f_{\mathrm{Earth}}^{\mathrm{Proton}}(r_{t_{87}},\ \mathrm{P},\ t_{87})}\right). \tag{6.9}$$

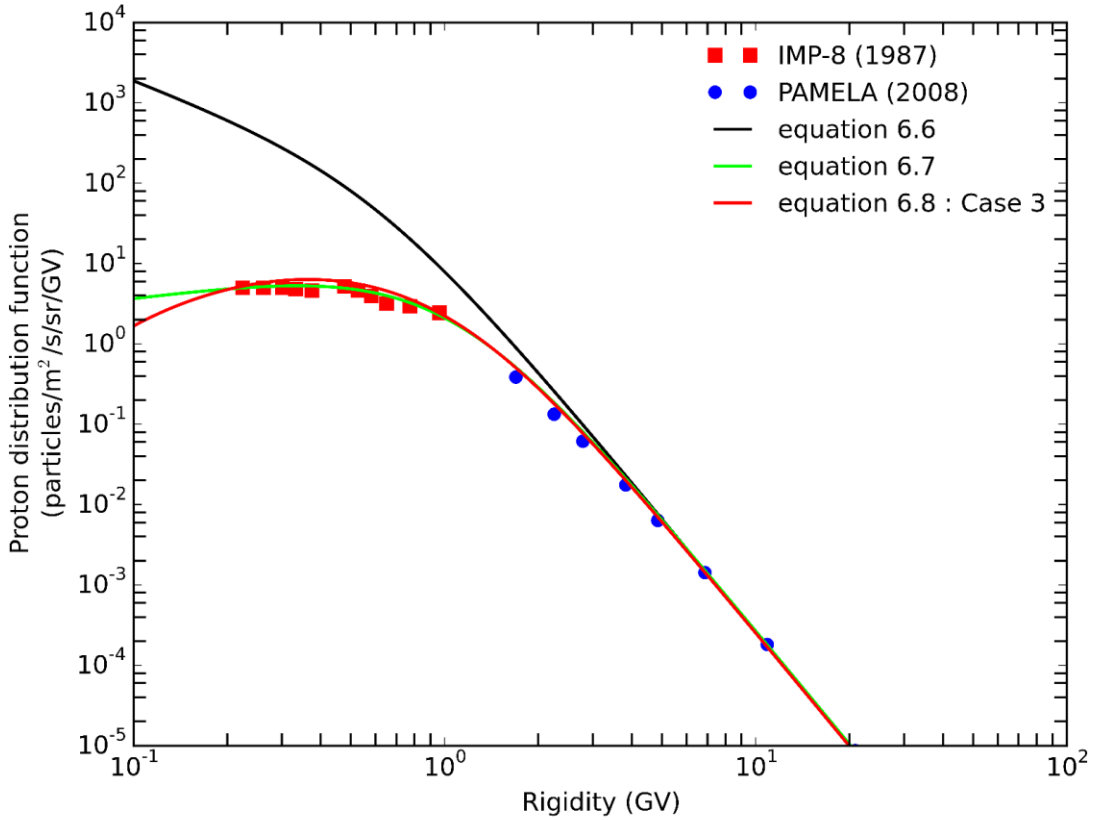

Figure 6.7: Proton data from IMP - 8 (red squares) and PAMELA (blue circles) are plotted together with equation 6.6 (black line), 6.7 (green line) and 6.8 (red line).

The parameters $M^{\mathrm{R}}(r_{t_{87}},\ t_{87})$ can be calculated as a function of heliocentric radial distance, rigidity or time. In this section $M^{\mathrm{R}}(r_{t_{87}},\ t_{87})$ is calculated as a function of rigidity between the 1987 and 2008 measured intensities by IMP - 8 and PAMELA. For a quantitative comparison between the calculated $M^{\mathrm{R}}(r_{t_{87}},\ t_{87})$ using the double power law (equation 6.7) and Convection-Diffusion (equation 6.8), this study follows the guidelines of *Caballero-Lopez* and *Moraal* (2012). The proton LIS parameterization and the double power law fit equation at 1 AU are both based on *Caballero-Lopez* and *Moraal* (2012) equation 2. These authors recommended that their equation 2 should not be used below its limit of validity at P = 0.7 GV. Therefore, all the calculated $M^{\mathrm{R}}(r_{t_{87}},\ t_{87})$ values will only be compared above $\mathrm{P} = 0.7$ GV. Figure 6.8 shows the parameter $M^{\mathrm{R}}(r_{t_{87}},\ t_{87})$ as a function of rigidity.

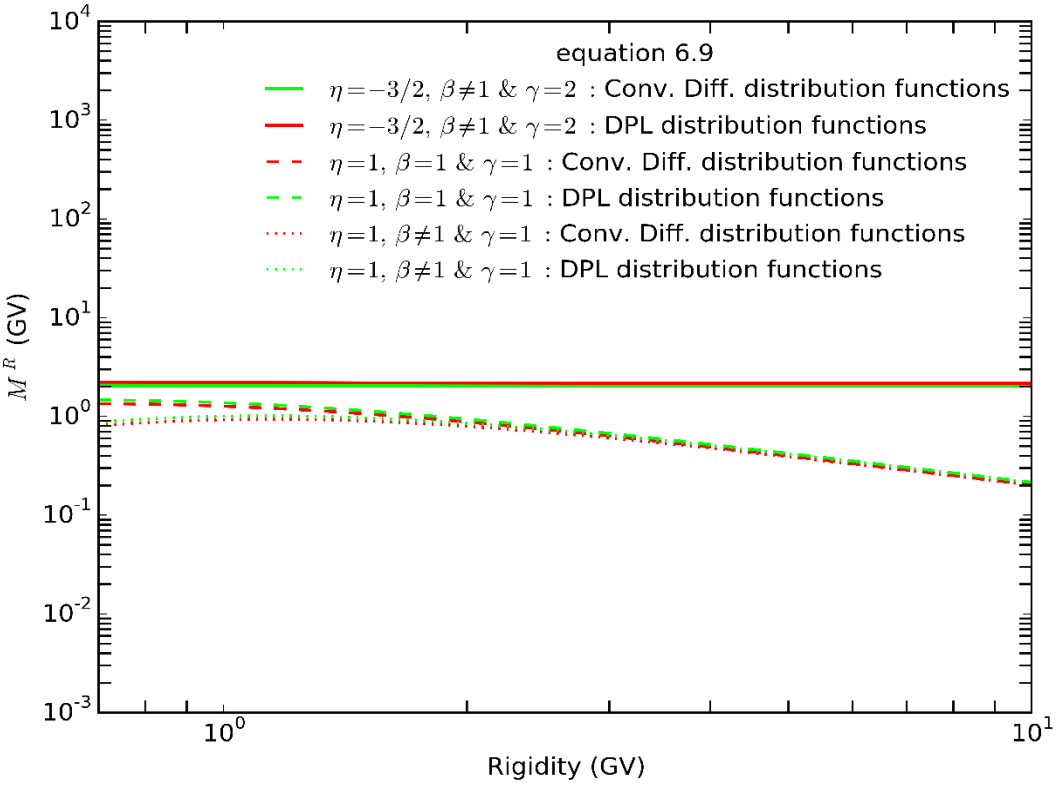

Figure 6.8: The parameter $M^{\mathrm{R}}(r_{t_{87}},\ t_{87})$ is plotted as function of rigidity.

From the figure, $M^{\mathrm{R}}(r_{t_{87}},\ t_{87})$ is calculated from the double power law parameterization (green lines) and Convection-Diffusion approximation (red lines). Here, parameters for the diffusion coefficient for the three cases mentioned in section 6.6.1 are used. Case 1 parameters are represented by the dashed lines, Case 2 are represented by the dotted lines and the lines represent Case 3 parameters. The parameter $M^{\mathrm{R}}(r_{t_{87}},\ t_{87})$ represents modulation at all rigidities and it is constant only when Case 3 parameters are chosen and this is very important at neutron monitors energies for long-term studies. $M^{\mathrm{R}}(r_{t_{87}},\ t_{87})$ calculated between 1987 and 2008 is $\approx$ 2.036 GV above 0.7 GV using the Convection-Diffusion approximation and $\approx$ 2.186 GV using the double power law parameterization.

6.7 The Force-Field approximation approach

This section describes how the Force-Field approximation is used to fit data at 1 AU and how the rigidity loss $\Phi(r_t,\ t)$ and the modulation parameter $\phi(r_t,\ t)$ are calculated.

6.7.1 The Force-Field intensity spectrum approximation

In section 4.7, a detailed formulation of this approximation was given. In terms of rigidity this is given as

$$j^{\mathrm{Proton}}_{\mathrm{P,\ FF}}(r_{t_{87}},\ \mathrm{P}_{t_{87}},\ t_{87}) = j^{\mathrm{Proton}}_{\mathrm{P,\ LIS}}(r_{\mathrm{LIS},\ t_{87}},\ \mathrm{P}_{\mathrm{LIS},\ t_{87}},\ t_{87})\left(\frac{\mathrm{P}_{t_{87}}}{\mathrm{P}_{\mathrm{LIS},\ t_{87}}}\right)^2, \tag{6.10}$$

where $\mathrm{P}_{\mathrm{LIS}}$ is the rigidity at the location of the LIS. Similar to the Convection-Diffusion approximation, this approximation is used to fit the measured cosmic-ray proton intensities from IMP - 8 and PAMELA data at 1 AU. The values chosen to fit these measured datasets at 1 AU were

the solar wind speed $V = 400\ \mathrm{km \cdot s^{-1}}$ and the diffusion coefficient $\kappa(r, P, t) = 4.38 \times 10^{12} \beta^{\eta} P_0^{(1-\gamma)} P^{\gamma}\ \mathrm{km^2 \cdot s^{-1}}$ The quantity β is given by equation 4.10. In the outer heliosphere, equation 6.10 gives better results when the LIS boundary is chosen to be $r_{LIS} = 90\ \mathrm{AU}$, according to *Caballero-Lopez* and *Moraal* (2004).

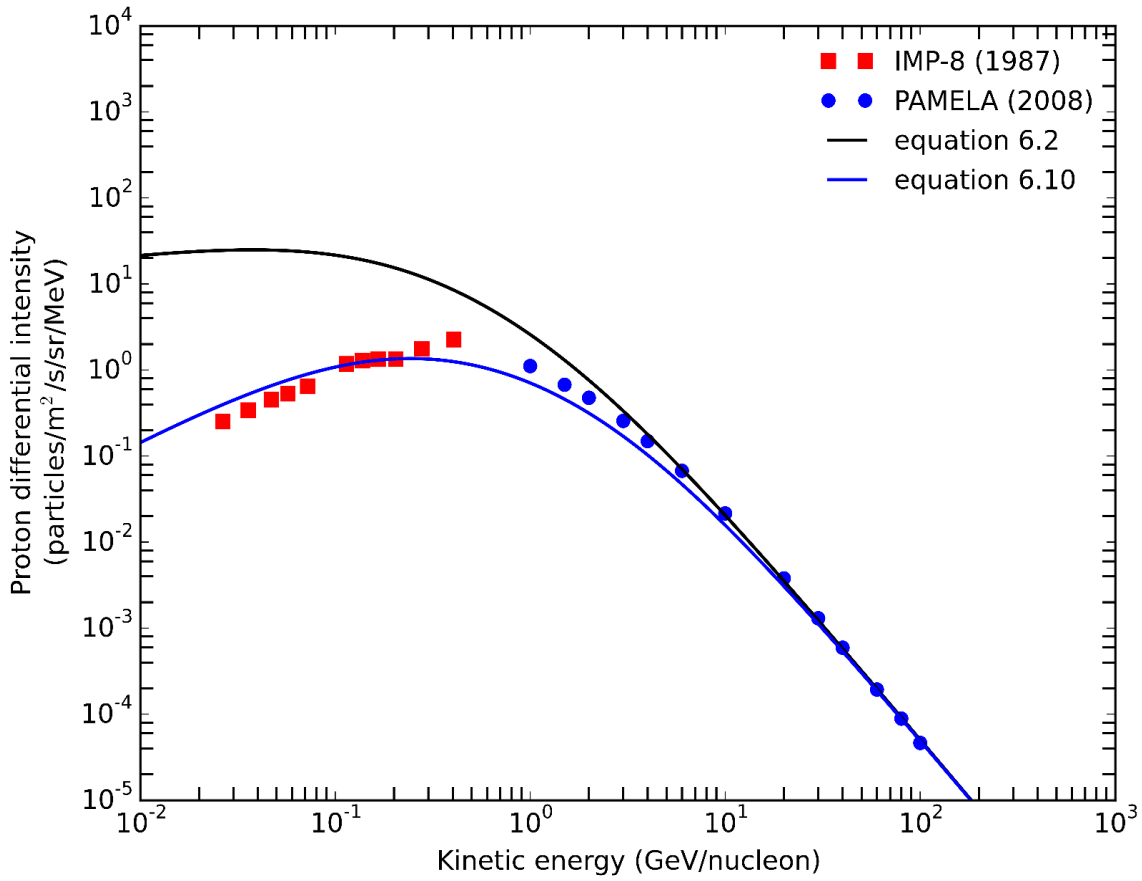

Figure 6.9: IMP - 8 (red squares) and PAMELA (blue circles) proton data are plotted together with equation 6.2 (black line) and 6.10 (blue line).

To obtain a simple expression as mentioned earlier, the diffusion coefficient parameter $\eta = 1$, $\beta = 1$ and $\gamma = 1$ in equation 4.35, have to be chosen. For these values, the Force-Field approximation describes modulation as a rigidity loss as (*Gleeson* and *Axford*, 1968)

$$\Phi(r_{t_{87}}, t_{87}) = P_{LIS,\, t_{87}} - P_{t_{87}}, \tag{6.11}$$

as mentioned in section 4.8. Figure 6.9 shows the fit to data of this approximation, which is clearly not good.

6.7.2 Calculation of the modulation parameter $\phi^{\mathrm{R}}(r_{t_{87}}, t_{87})$

Similar to Figure 6.7, the IMP - 8 (red squares) and PAMELA (blue circles) measured proton intensities were also converted to distribution functions. The distribution functions calculated from the measured proton intensities using the double power law equation and the LIS are shown in equation 6.7 and 6.6, respectively. The distribution function using the Force-Field approximation is

$$f_{\mathrm{FF}}^{\mathrm{Proton}}(r_{t_{87}}, \mathrm{P}_{t_{87}}, t_{87}) = \frac{j_{\mathrm{P,\,FF}}^{\mathrm{Proton}}(r_{t_{87}}, \mathrm{P}_{t_{87}}, t_{87})}{\mathrm{P}_{t_{87}}^{2}} = f_{\mathrm{LIS}}^{\mathrm{Proton}}(r_{\mathrm{LIS},\,t_{87}}, \mathrm{P}_{\mathrm{LIS},\,t_{87}}, t)\mathrm{P}_{t_{87}}^{2}\,\mathrm{P}_{\mathrm{LIS},\,t_{87}}^{-2}. \quad (6.12)$$

Similar to Figure 6.7, these distribution functions are plotted as a function of rigidity, as shown in Figure 6.10. The black, red and green solid lines represent equations 6.6, 6.7 and 6.12, respectively.

The parameter $\phi^{\mathrm{R}}(r_{t_{87}}, t_{87})$ using both approximate solutions is calculated by choosing two rigidity values in Figure 6.10, i.e. one from $\mathrm{P}_{\mathrm{LIS},\,t}$ and the other one from $\mathrm{P}_{t_{87}}$. When $\mathrm{P}_{\mathrm{LIS},\,t_{87}}$ values are substituted in the distribution function $f_{\mathrm{LIS}}^{\mathrm{Proton}}(\mathrm{P}_{\mathrm{LIS},\,t_{87}})$ and $\mathrm{P}_{t_{87}}$ values are substituted in $f_{\mathrm{DPL}}^{\mathrm{Proton}}(\mathrm{P}_{t_{87}})$ and $f_{\mathrm{FF}}^{\mathrm{Proton}}(\mathrm{P}_{t_{87}})$, they must produce the same output value. Then, the parameter $\phi^{\mathrm{R}}(r_{t_{87}}, t_{87})$ has to be equal to 1/3 of the modulation parameter

$$M^{\mathrm{R}}(r_{t_{87}}, t_{87}) = \beta^{\eta}\frac{\mathrm{P}^{\gamma}}{\mathrm{P}_{0}^{(\gamma-1)}}\ln\left(\frac{f_{\mathrm{LIS}}^{\mathrm{Proton}}(r_{\mathrm{LIS}}, \mathrm{P}, t_{87})}{f_{\mathrm{Earth}}^{\mathrm{Proton}}(r_{t_{87}}, \mathrm{P}, t_{87})}\right) = \frac{\mathrm{V}(r_{\mathrm{LIS},\,t_{87}} - r_{t_{87}})}{\kappa_{1}}.$$

According to *Caballero-Lopez* and *Moraal* (2004) and *Moraal* (2011), if the above procedure is not possible, then the modulation rigidity loss $\Phi(r_{t_{87}}, t_{87})$ cannot be converted to the parameter $\phi^{R}(r_{t_{87}}, t_{87})$. These authors proposed that in this case it is more correct to describe modulation in the Force-Field formalism with the magnitude of the dimensionless parameter $M(r_{t_{87}}, t_{87})$.

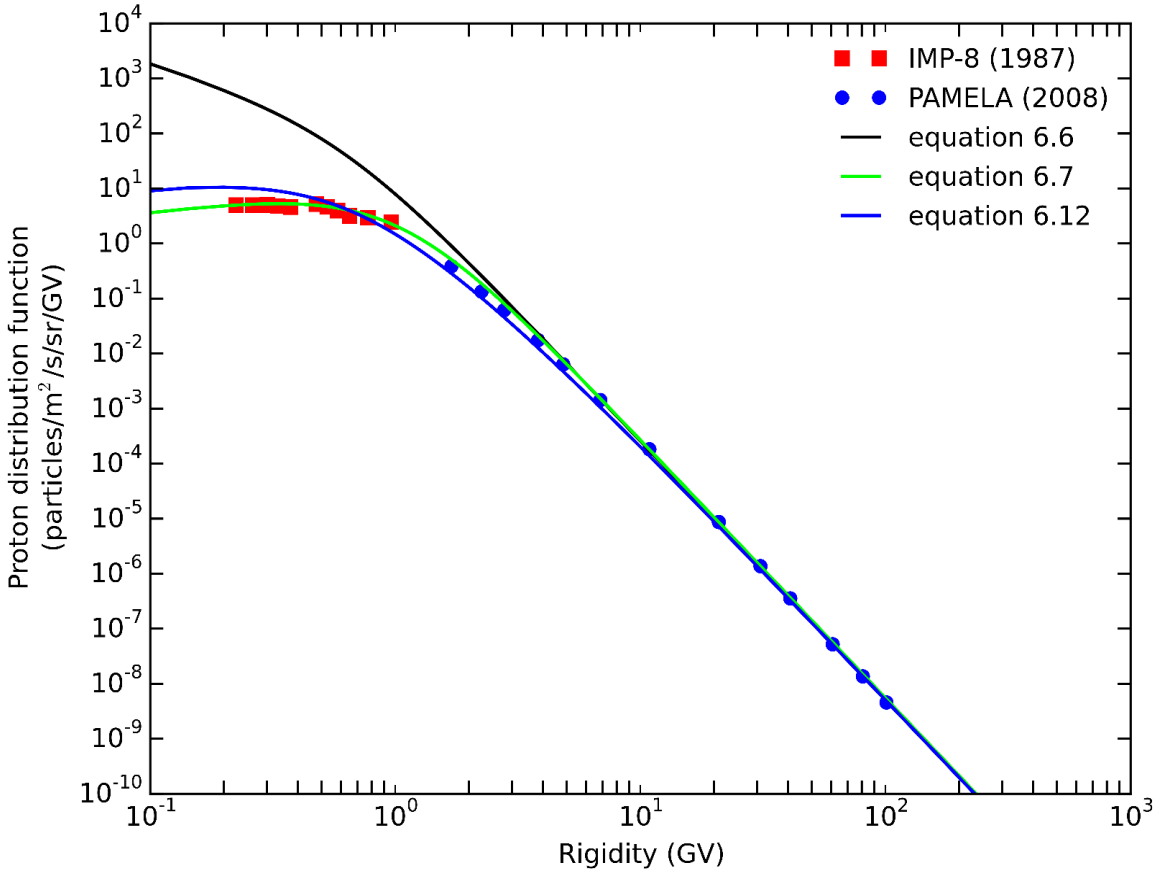

Figure 6.10: IMP - 8 (red squares) and PAMELA (blue circles) proton data are plotted together with equation 6.6 (black line), 6.7 (green line) and 6.12 (blue line).

Since a constant rigidity loss parameter $\Phi(r_{t_{87}}, t_{87})$ could not be obtained through the substitution of $P_{LIS,\, t_{87}}$ and $P_{t_{87}}$ in the distribution functions in this study, it was calculated through $V(r_{LIS,\, t_{87}} - r_{t_{87}}) / \kappa_1$, where

$r_{\mathrm{LIS},\, t_{87}} = 90$ AU and $\kappa_1 = 4.38\times10^{12}$ km^2·s^{-1}·GV^{-1}. Therefore, modulation parameter $\phi^{\mathrm{R}}(r_{t_{87}},\, t_{87}) = 0.407\,\mathrm{GV}$

6.8 Comparing the approximate spectra

In this section, the Convection-Diffusion approximation, Force-Field approximation and the double power law parameterization used to fit the proton IMP - 8 and PAMELA data, are compared as shown in Figure 6.11. The green solid line represents the double power law fit (equation 6.3). The blue and red lines represent the Convection-Diffusion (equation 6.4) and Force-Field (equation 6.10) fits, respectively. However, because of the fact that the full nature of the diffusion coefficient is not yet fully understood (*Moraal* 2011), not all approximate solutions are expected to produce a good fit to data at lower energies. Nonetheless, equation 6.10 fits IMP - 8 data at 1 AU poorly compared with both equations 6.3 and 6.4.

The comparison between these fit equations confirms that the Convection-Diffusion approximation is a good approximation compared with the Force-Field approximation for the current choice of diffusion parameters. With increasing heliocentric radial distance the Force-Field approximation gets progressively worse, but the Convection-Diffusion solution improves. For a detailed discussion on the limitations of the Force-Field approximation, see the study by *Caballero-Lopez* and *Moraal* (2004). According to them, the Force-Field model is a better approximation in the inner heliosphere than in the outer one. This is because this model gives the higher limit on the rigidity changes and therefore this must happen once the cosmic rays reach the inner heliosphere.

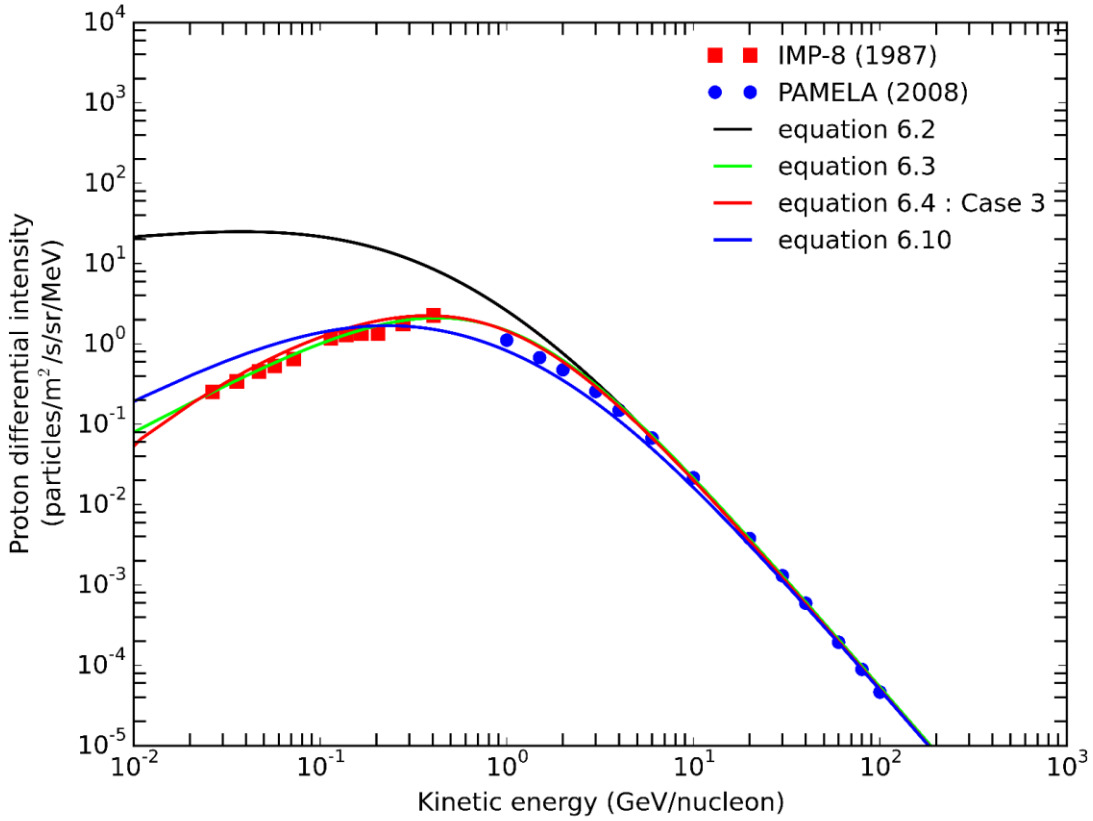

Figure 6.11: Comparisons of fits to the IMP - 8 and PAMELA proton data at 1 AU.

6.9 Summary

This chapter concludes that the Force-Field approximation does not fit IMP - 8 data well. With the type of diffusion coefficient used in this study, it is evident that the approximation might fit data only if the diffusion coefficient is modified. The double power law parameterization and Convection-Diffusion approximation are both very good in fitting data and calculating the modulation parameters compared with the Force-Field approximation.

Chapter 7

A comparative study of modulation parameters and their implications

7.1 Introduction

The imprint of the 11-year solar activity cycle is present in modulation parameters. The anti-correlation between the count rates of neutron monitors and the modulation parameters are shown in sections 5.2.1 and 5.2.2. The time-dependent parameter $\phi^f(r_t,\ t)$ has been calculated by *Usoskin et al.* (2011), using the Force-Field approximation. These authors used ionization chamber data from July 1936 to January 1951 and neutron monitor data from February 1951 to December 2009. This chapter aims to calculate the parameters $M^f(r_t,\ t)$ and re-calculate the parameters $\phi^f(r_t,\ t)$ as function of time.

The approach used in this study to calculate $\phi^f(r_t,\ t)$ is different from that of *Usoskin et al.* (2005, 2011). In this study, it was calculated as proposed in sections 4.7 and 4.10, where the modulation parameter changes are calculated first. To carry out these calculations a detailed procedure was outlined in sections 5.2.1 and 5.2.2. The procedure used is independent of the LIS parameterization, and only one yield function (adopted from *Caballero-Lopez* and *Moraal*, 2012) was chosen for all neutron monitors. The second part of calculating the modulation parameter was done in sections 6.6.2 and 6.7.2 with reference to the recent proton LIS intensities measured by Voyager - 1 in 2012. Also, data from two other spacecraft, i.e. IMP - 8 and PAMELA were used (see subsections of 6.7). These

modulation parameters of the second part were called the reference modulation parameter. Now, to find the full modulation parameter, the reference modulation parameter of section 6.6.2 (and 6.7.2); and the modulation parameter changes of section 5.2.1 (and 5.2.2) have to be combined, as outlined in equation 4.24 (and 4.42), respectively. Calculations of the parameters $\phi^f(r_t, t)$ and $M^f(r_t, t)$ as function of time may have a significant impact on the re-construction and analysis of cosmic-ray intensities in the past.

The chapter is organised as follows. In sections 7.2 and 7.3, the time-dependent parameters $M^f(r_t, t)$ and $\phi^f(r_t, t)$ are shown. In Section 7.4, the time-dependent parameter $\phi^f(r_t, t)$ calculated by *Usoskin et al.* (2011) for July 1936 onward is compared with those obtained in this study from July 1957 to October 2016. In section 7.5, the long-term cosmic-ray intensities are discussed. Then, a brief summary follows.

7.2 The modulation parameter $M^f(r_t, t)$

According to equation 4.26, the combined reference modulation parameter and the modulation parameter change gives the full modulation parameter as

$$M^f(r_t,\ t) = M^{\mathrm{R}}(r_{t_{87}},\ t_{87}) + M^{*}(r_{t_1},\ t_1,\ r_{t_2},\ t_2). \tag{7.1}$$

The reference modulation parameter $M^{\mathrm{R}}(r_{t_{87}},\ t_{87})$ was calculated and plotted in Figure 6.8. This parameter was about 2.036 GV at all rigidities when it was calculated using the diffusion coefficient parameters chosen for Case 3. The difference between the calculated $M^{\mathrm{R}}(r_{t_{87}},\ t_{87})$ from the double power law parameterization and the Convection-Diffusion spectrum approximation for Case 3 is about 7.37 %. These values of

$M^{\mathrm{R}}(r_{t_{87}},\ t_{87})$ calculated for Case 3 have to be added to the parameter $M^{*}(r_{t_1},\ t_1,\ r_{t_2},\ t_2)$ already calculated in section 5.2.1.

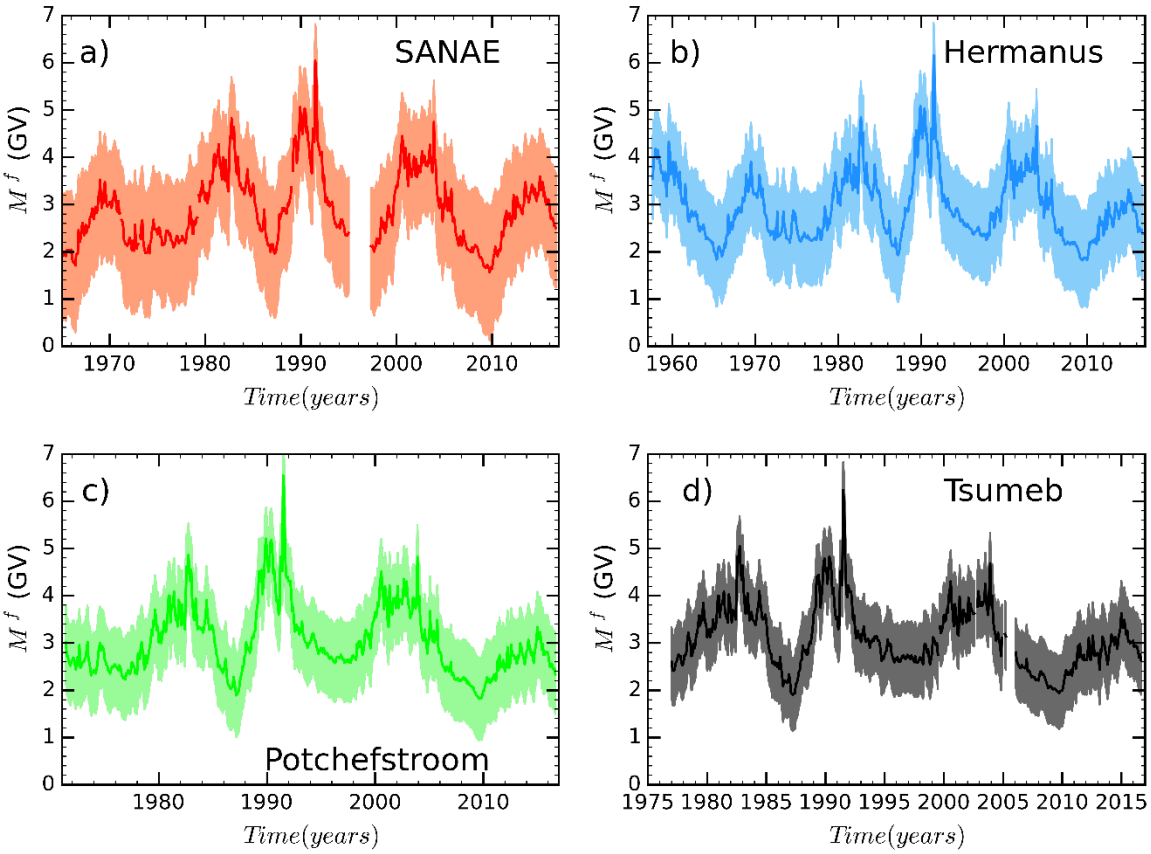

Figure 7.1: Calculated monthly values of $M^f(r_t,\ t)$ as a function of time for each of the four chosen stations. The 95 % confidence intervals are shown as grey shading in all panels.

Now, the question is of all the possible calculated values of M^{*}, which ones must the calculated $M^{\mathrm{R}}(r_{t_{87}},\ t_{87})$ for Case 3 be added to. Unfortunately, because there has never been a study to calculate $M^f(r_t,\ t)$ as function of time before, there is nothing to compare with.

In section 5.3, it was shown that at neutron monitor energies the calculated M^{*} at $\mathrm{P} = 0.8$ GV using parameters $\eta = 1$, $\beta = 1$ and a value of γ somewhere between 0.9 and 1.0 is $\approx 3\Delta\phi$ at the same P. Hence, $M^{*} \approx 3\Delta\phi$ at $\mathrm{P} > 0.8$ GV only if parameters $\eta = 1$, $\beta = 1$ and $\gamma = 1$, are chosen. Therefore, without any preference for the calculated

M^* in section 5.3, the M^* calculated using parameters $\eta = 1$, $\beta \neq 1$ and $\gamma = 1$, was chosen to calculate $M^f(r_t, t)$.

Figure 7.1 shows the calculated monthly values of $M^f(r_t, t)$ as a function of time for each of the four chosen stations with 95 % confidence intervals (grey shading). The four chosen neutron monitors, SANAE, Hermanus, Potchefstroom and Tsumeb, are indicated by (a), (b), (c) and (d), respectively.

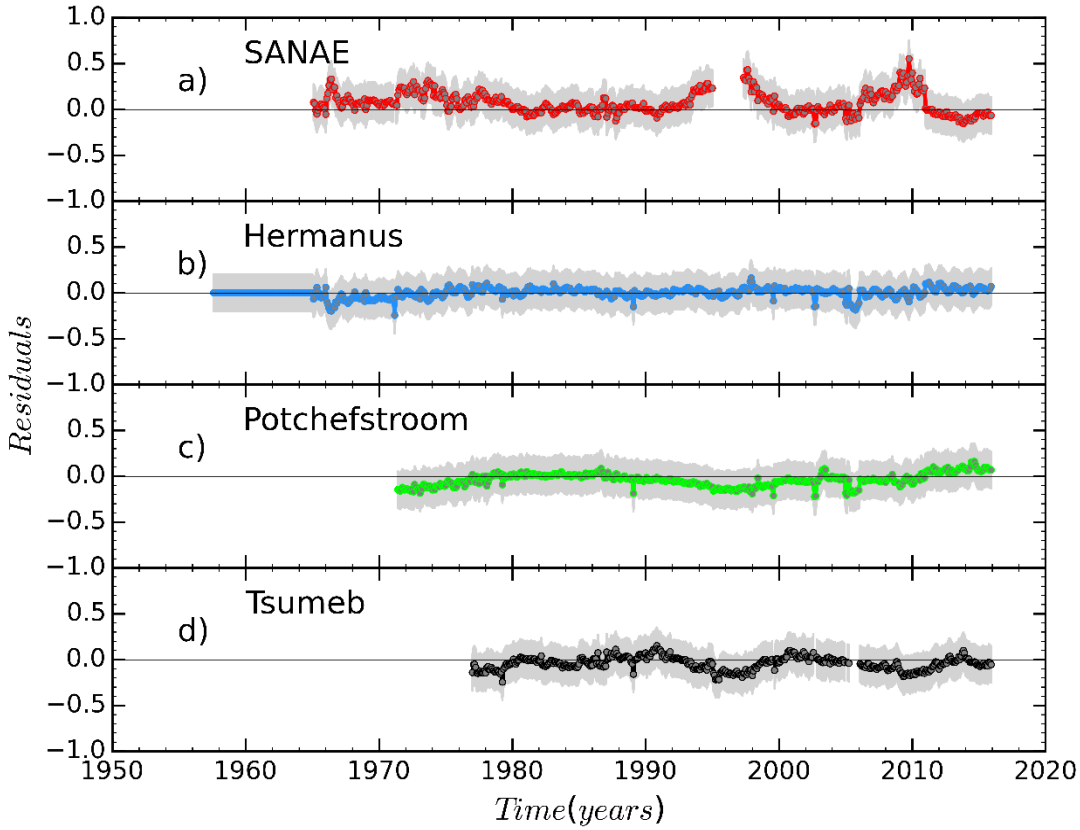

Figure 7.2: Calculated residuals using equation 7.2. All stations agree to within ± 25 %. The 95 % confidence intervals are shown as grey shading in all panels.

Figure 7.2 shows the calculated residuals between monthly values of the calculated $M^f(r_t, t)$ for all stations (denoted as $\bar{M}^f(r_t, t)$) and $M^f(r_t, t)$ from one station (used as a reference). These residuals are calculated from the equation

$$\text{Residuals} = \left[\frac{\bar{M}^f(r_t,\, t) - M^f(r_t,\, t)}{M^f(r_t,\, t)} \right] \tag{7.2}$$

Panels (a), (b), (c) and (d) represent the residuals calculated for the SANAE, Hermanus, Potchefstroom and Tsumeb neutron monitors, respectively. From the figure, the residuals of these stations agree to within $\pm$ 25 %. However, the calculated residual for Hermanus is significantly less and essentially constant over time compared with other stations. This implies that the calculated $\bar{M}^f(r_t,\, t)$ is essentially the same as the calculated $M^f(r_t,\, t)$ from the Hermanus neutron monitor. Instead of using $\bar{M}^f(r_t,\, t)$, the calculated $M^f(r_t,\, t)$ from the Hermanus neutron monitor could be used for long-term studies.

7.3 The modulation parameter $\phi^f(r_t, t)$

Similar to the Convection-Diffusion approximation, the modulation parameter change $\Delta\phi$ was calculated as function of time in section 5.2.2 from count rates of neutron monitors at various cutoff rigidities. Now, according to equation 4.44, the full modulation parameter can be calculated as

$$\phi^f(r_t,\, t) = \phi^{\mathrm{R}}(r_{t_{87}},\, t_{87}) + \Delta\phi(r_{t_1},\, t_1,\, r_{t_2},\, t_2), \tag{7.3}$$

where $\phi^{\mathrm{R}}(r_{t_{87}},\, t_{87})$ is the reference modulation parameter calculated in section 6.7.2. In that section, it was mentioned that it is not easy to get a constant $\phi^{\mathrm{R}}(r_{t_{87}},\, t_{87})$ between the rigidity at the LIS and the earth from measured intensities using the double power law parameterization and Force-Field approximation. Hence, using equation 4.36 together with the parameters used to plot Figure 6.9, the calculated value of $\phi^{\mathrm{R}}(r_{t_{87}},\, t_{87})$ is about 0.407 GV which is equivalent to what was expected when using the rigidity loss concept.

This calculated value of $\phi^{\mathrm{R}}(r_{t_{87}},\ t_{87})$ will be used in all stations in the calculation of the parameter $\phi^{f}(r_{t_{87}},\ t_{87})$. Figure 7.3 shows the calculated monthly values of $\phi^{f}(r_{t_{87}},\ t_{87})$ as a function of time for each of the four chosen stations with 95 % confidence intervals (grey shading). From the figure, the four chosen neutron monitors SANAE, Hermanus, Potchefstroom and Tsumeb are indicated by (a), (b), (c) and (d) respectively.

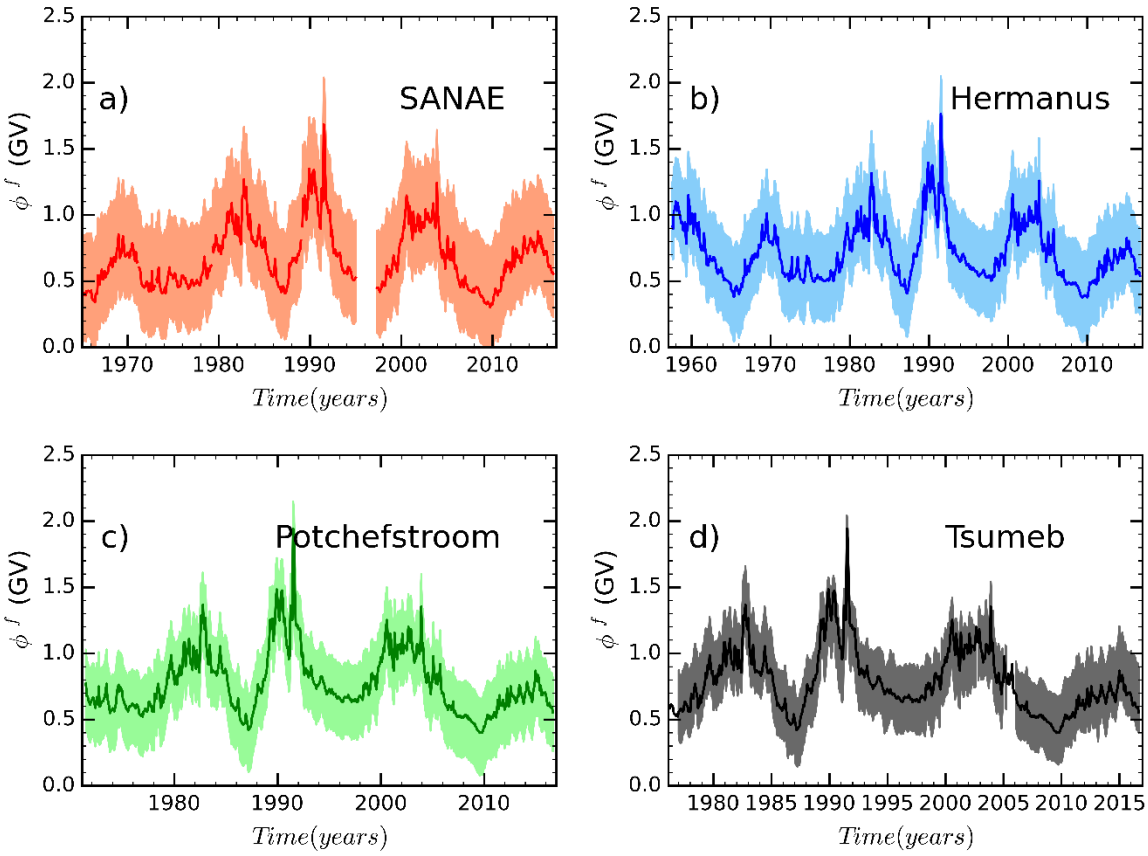

Figure 7.3: Calculated monthly values of $\phi^{f}(r_{t},\ t)$ as a function of time for each of the four chosen stations. The 95 % confidence intervals are shown as grey shading in all panels.

Figure 7.4 shows the calculated residuals between the monthly values of the calculated $\phi^{f}(r_{t},\ t)$ for all stations (denoted as $\overline{\phi}^{f}(r_{t},\ t)$) and $\phi^{f}(r_{t},\ t)$ from one station (used as a reference). Panel (a), (b), (c) and (d) represents the residuals calculated for the SANAE, Hermanus, Potchefstroom and Tsumeb neutron monitors, respectively. The

equation used to calculate residuals is as in equation 7.2, the only difference is that here $\phi^f(r_t, t)$ is used instead of $M^f(r_t, t)$. From the figure, the residuals of these stations agree to within $\pm$ 25 %. The calculated residual for Hermanus is again significantly less and essentially constant over time compared with other stations. This motivates the use of data from the Hermanus neutron monitor for long-term studies and for comparing with other published results.

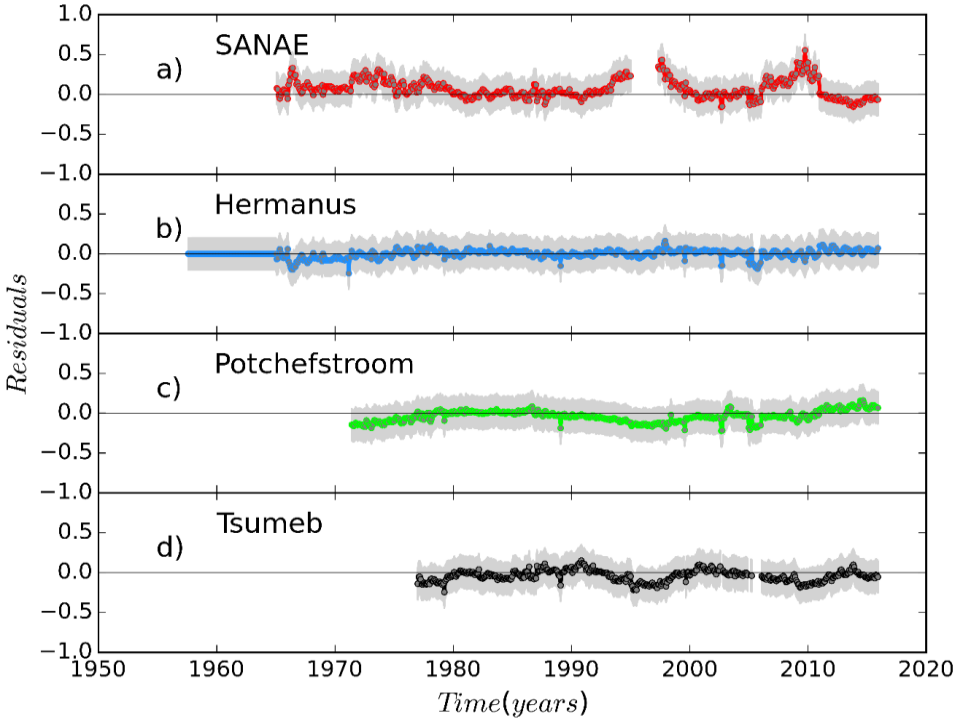

Figure 7.4: Calculated residuals using equation 7.2. All stations agree to within $\pm$ 25 %. The 95 % confidence intervals are shown as grey shading in all panels.

7.4 Comparison of calculated modulation parameters

The *Usoskin et al.* (2005, 2011) calculation of the modulation parameter $\phi^f(r_t, t)$ as function of time is based on a weighted mean over several neutron monitor stations, three different yield functions and the *Burger et al.* (2000) LIS parameterization. However, the calculated

$\phi^f(r_t, t)$ as function of time by *Usoskin et al.* (2005, 2011) in 1991 is significantly higher than all solar maximum values.

Recently, *Ghelfi et al.* (2016) calculated the monthly values $\phi^f(r_t, t)$ using the KIEL neutron monitor. Compared to *Usoskin et al.* (2005, 2011), the re-constructed $\phi^f(r_t, t)$ as a function of time by *Ghelfi et al.* (2016) has smaller amplitude of variation during both solar minimum and maximum times. Also, they obtain lower modulation levels when one takes the difference between modulation parameter $\phi^f(r_{t_{87}}, 1987)$ and $\phi^f(r_{t_{91}}, 1991)$. For more information on the calculated $\phi^f(r_t, t)$ as function of time from *Ghelfi et al.* (2016) compared with *Usoskin et al.* (2005, 2011), see Figure 5 of *Ghelfi et al.* (2016).

The calculation of $\phi^f(r_t, t)$ using an LIS parameterization different from both *Usoskin et al.* (2005, 2011) and *Ghelfi et al.* (2016) prove the consistency of *Herbs et al.* (2010) study. These authors pointed out that the use of various LIS parameterizations can cause the calculated modulation parameters to be either high (with positive values) or significantly low (often with negative values).

Figure 7.5 shows an updated calculated $\phi^f(r_t, t)$ as function of time from July 1936 to October 2016 according to *Usoskin et al.* (2011) compared with $\phi^f(r_t, t)$ from the Hermanus neutron monitor. The calculated $\phi^f(r_t, t)$ from the Hermanus neutron monitor shows to be higher than that calculated by *Usoskin et al.* (2011), as indicated by the predominantly positive values of the percentage difference in the bottom panel.

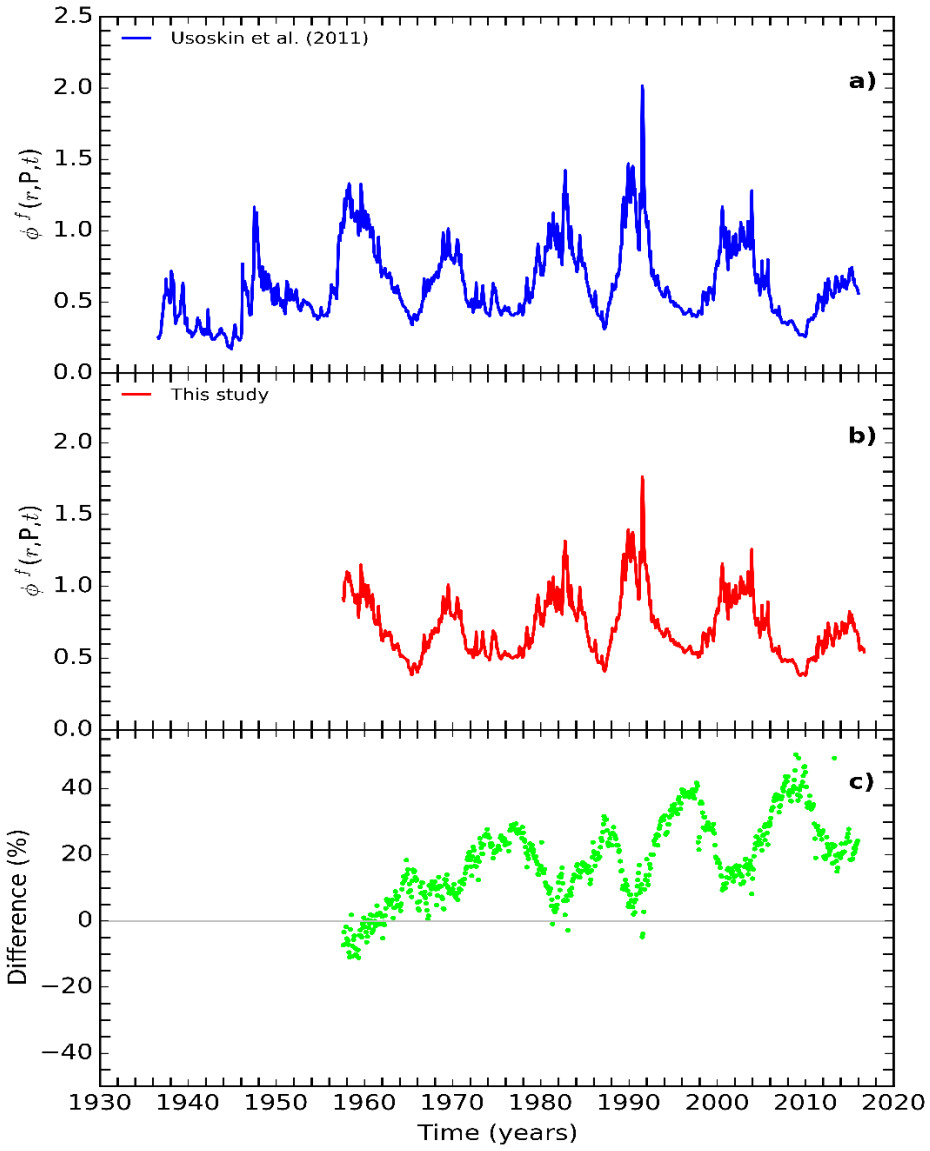

Figure 7.5: Comparison of calculated modulation parameters. Panel (a) represents the re-constructed $\phi^f(r_t, t)$ calculated by *Usoskin et al.* (2011) from July 1936 to October 2016 (blue line). Panel (b) represents the re-constructed $\phi^f(r_t, t)$ using the Hermanus neutron monitor from July 1957 to October 2016 (red line). Panel (c) represents the percentage difference between the $\phi^f(r_t, t)$ calculated from this study and that of *Usoskin et al.* (2011) from July 1957 to October 2016 (green dots).

7.5 Long-term cosmic-ray intensity record

In the simplest modulation theories, the calculated modulation parameter $M^f(r_t, t)$ and $\phi^f(r_t, t)$ from count rates of neutron monitors play a significant role in the re-construction and analysis of cosmic-ray intensity profiles at present and in the past. Similar to solar activity indicators (e.g. sunspot number), the calculated modulation parameter displays an anti-correlation when compared with count rates of neutron monitors. To improve our understanding of these scenarios, a series of investigations have been proposed (and tested), and some creditable answers to these open questions were given in section 5.2.1. Sections 5.2.1 and 5.2.2 showed that the calculation of modulation parameter changes from count rates of neutron monitors since the 1950s can either be large or small depending on the type of diffusion coefficient parameters used. *McCracken* and *Beer* (2007) studied cosmic-ray intensities prior to neutron monitor era. They re-constructed a long-term record of cosmic-ray intensities by including ionization chamber data record from 1933 to 1951, and the ^{10}Be record from 1428 to 1933. This ^{10}Be is a secondary product produced from atmospheric processes as mentioned in section 2.8.4. These authors believe that, despite the large uncertainties associated with intensities in ionization chambers and the ^{10}Be record, their methods of correction make the long-term record very reliable.

Figure 7.6 shows the cosmic-ray intensities re-constructed from ^{10}Be data from 1428 to 1933 and the ionization chamber data from 1933 to 1951 calculated by *Forbush* (1958) and *Neher* (1971). The Climax and Hermanus neutron monitors data are shown from 1951 to 2006 and 2006 to 2010, respectively. McCracken and Beer suggest that if the ^{10}Be and the ionization chamber were neutron monitors during the Dalton, Maunder and Spoerer minima years, they could have measured cosmic-ray

intensities which are higher than at present. The Climax neutron monitor LIS of about 119.5 % was used by McCracken and Beer to denote the estimated count rate if there were no modulation of cosmic rays. However, Figures 6.2, 6.3 and 6.4 showed that the intensity of cosmic rays measured at the boundary of the heliosphere by Voyager - 1 is higher than those measured on earth by IMP - 8 and PAMELA. The ^{10}Be record in Figure 7.6 shows the contrary with inferred counting rates exceeding the assumed LIS. Around the year 1450, 1510 and 1700, the ^{10}Be intensity at earth is higher than the intensity at the boundary of the heliosphere and beyond, which is unlikely.

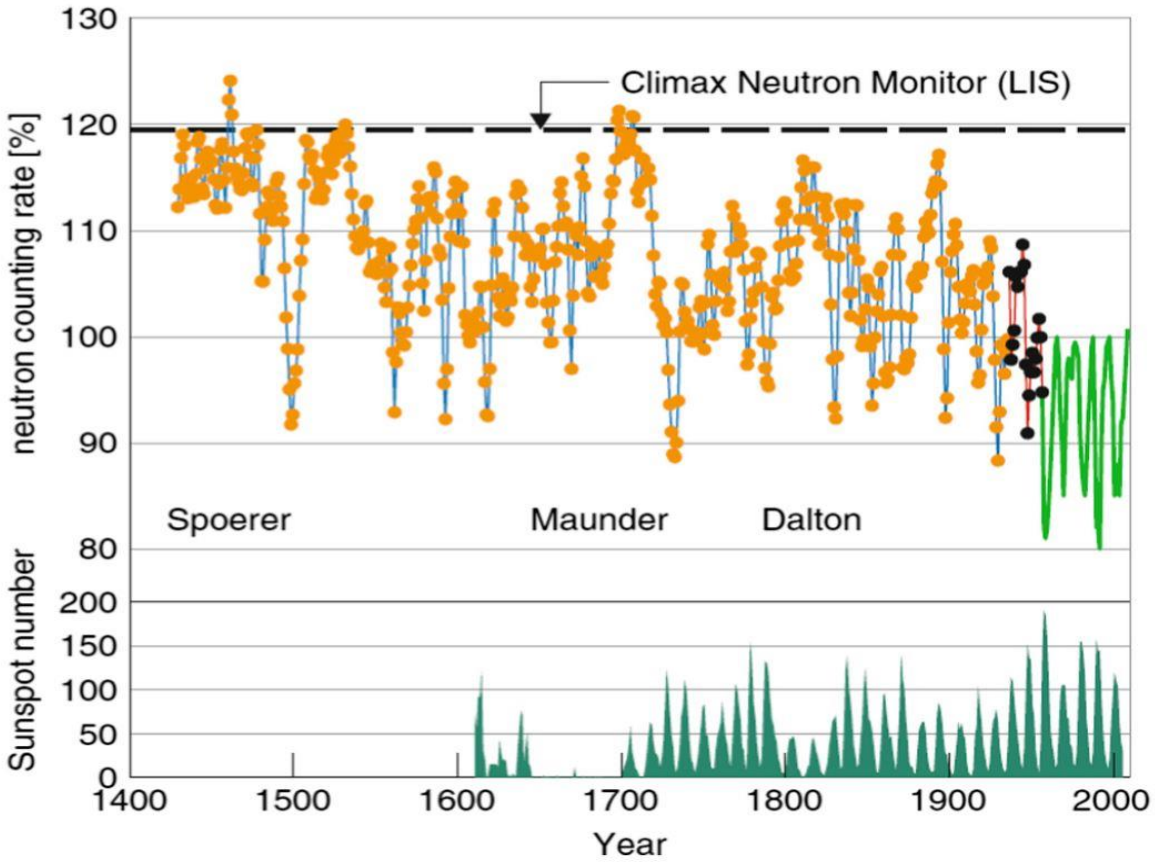

Figure 7.6: The orange dots and blue line represent the ^{10}Be data from 1428 to 1933. The black dots and red line represent the *Forbush* (1958) and *Neher* (1971) ionization chamber data from 1933 to 1951 and the green line represents the Climax neutron monitor from 1951 to 2006 and Hermanus neutron monitor from 2007 to 2010. Sunspot numbers are represented from 1610 to 1995 (dark green). Source: *Beer et al.* (2012).

7.6 Summary

This study has revisited the calculation of $\phi^f(r_t, t)$ as function of time (and its uncertainties) of *Usoskin et al.* (2005, 2011). The analysis made here benefits from the improvements made on the determination of the proton LIS from Voyager - 1 measurements. Further improvements of the time-dependent $\phi^f(r_t, t)$ are required by improving the yield function parametrization. The calculated modulation parameters as function of time from the Convection-Diffusion and the Force-Field approximations might have a significant impact on the re-construction of cosmic-ray intensities in the past, such as that of *McCracken* and *Beer* (2007) cosmic-ray intensities.

Chapter 8

Summary, conclusions and recommendations

This chapter serves to summarize the previous chapters with emphasis on the most important conclusions and recommendations. The brief summaries and conclusions were presented at the end of each chapter and here they are expanded. In chapter 1 an overview of this dissertation was given.

The relevant background, concepts and nomenclature important for modulation of cosmic ray studies and heliospheric physics were discussed in chapter 2. The concept of the solar wind and the heliospheric magnetic field was introduced, i.e. how the solar wind carries the sun's magnetic field with it throughout the solar system to form the heliosphere. The concept of solar activity was outlined following a discussion on the dynamic magnetic nature of the sun. The sunspot number was introduced as proxy for solar activity. This was followed by a description of cosmic rays, classifying them according to their origin. Chapter 2 concluded with a discussion of the interaction of primary cosmic rays with the atmospheric nitrogen and oxygen creating a cascade of secondary cosmic rays with lower energies than the primaries. The ^{10}Be and nucleonic component of these secondaries are both of particular interest in the re-construction of the cosmic -ray intensities currently and in the past.

Chapter 3 discussed space-borne detectors used for primary cosmic rays and ground-based detectors for secondary cosmic rays. Missions used in the present study for primary cosmic rays are IMP - 8, PAMELA and Voyager - 1. Detectors for secondary cosmic rays, such as the neutron

monitors and ionization chambers, as well as the cosmogenic radionuclide ^{10}Be, were discussed. Four neutron monitors of the Centre for Space Research at the Potchefstroom campus of the NWU were used in this study. These neutron monitors are stationed at Hermanus, Tsumeb, SANAE and Potchefstroom. After discussing these detectors, response functions and differential response functions were introduced. The chapter ended with a discussion of the neutron monitor yield functions.

Chapter 4 introduced the concept of modulation of cosmic rays at neutron monitor energies. Also, a mathematical description of the transport of cosmic rays in the heliosphere was presented, known as the full Parker transport equation. This equation combines and describes the processes of cosmic rays in the heliosphere. A simplified approach was followed to solve the full Parker transport equation in the heliosphere. Before discussing the approximate solutions of the full Parker transport equation, two processes out of four, i.e. convection and diffusion, were discussed in some detail.

Inside the heliosphere, cosmic-ray diffusion is described by the diffusion tensor which specifies the scattering properties of the heliospheric magnetic field. The process of convection describes the manner in which the solar wind "pushes" all the cosmic-rays (on average) entering the spherically symmetric heliosphere. Two solutions of the full Parker transport equation were calculated, i.e. the spherically symmetric Convection-Diffusion approximation and the Force-Field approximation following a series of assumptions made to simplify the full Parker transport equation. Both these solutions depend on the choice of the diffusion coefficient, LIS intensities, the solar wind speed and the heliocentric radial distance to the boundary of the heliosphere. These approximate solutions were calculated from a power law diffusion coefficient of the form $\kappa(r,\ \mathrm{P},\ t) = \beta^{\eta}\kappa_1(r,\ t)\mathrm{P}_0^{(1-\gamma)}\mathrm{P}^{\gamma}$ where η and γ are two free parameters.

Chapter 5 illustrated the count rates of neutron monitors and the method used to calculate the modulation parameters. Further sections illustrated the effects of varying the key components of the diffusion coefficient by changing the parameters η, β and γ, and their influence on the calculated modulation parameter. The accuracy of the solutions obtained upon utilization of the count rates of neutron monitors was discussed. Issues concerning the exclusion of the yield function and LIS parameterization in the Convection-Diffusion approximation were discussed. Also, it was illustrated that the count rate model (equation 5.7 and 5.15) behaves in a consistent manner when adjusting the diffusion coefficient parameters η, β and γ.

It was concluded that, for the purposes of this study, selecting $\beta = 1$ or $\beta \neq 1$ while $\eta = 1$ in the Convection-Diffusion approximation has little effect for the same γ. However, choosing a different γ compared with the widely used $\gamma = 1$ has a very significant effect on the calculation of modulation parameter M^* using the Convection-Diffusion approximation. When any $\gamma > 1$ was chosen, the M^* calculated was distorted compared with those of $\gamma = 1$. Hence, for any $\gamma < 1$ chosen, the M^* calculated were suppressed compared with those of $\gamma \geq 1$. These results have never been reported before. Similarly, the Force-Field approximation was used to calculate the time-dependent modulation parameter $\Delta\phi$. This approach included the yield function adopted from *Caballero-Lopez* and *Moraal* (2012). Here the LIS intensities were also excluded. To calculate $\Delta\phi$, this approach was limited because of the restrictions imposed on the type of diffusion coefficient one can use. The diffusion coefficient chosen in this study was only useful if its parameters have the values i.e. $\eta = 1$, $\beta = 1$ while $\gamma = 1$.

In section 5.3, it was shown that between two specific times these approximations, i.e. M^* and $\Delta\phi$, are equivalent based on the *Gleeson* and *Urch* (1973) relation given in equation 5.11. The results from chapter 5 allowed one final conclusion regarding long-term studies of these modulation parameters. That is, as shown in section 5.2.1, the Convection-Diffusion should be a preferable choice because it produces reasonable results. Also, it has less restriction in the use of the parameters β, η and γ in the diffusion coefficient. This approximation can be useful to long-term studies such as the re-calculation of cosmic ray intensities in the past by *McCracken* and *Beer* (2007).

Chapter 6 discussed the concept of modulation using cosmic-ray intensities measured in space and at earth. In that chapter, the approximate solutions calculated in section 4.6 and 4.9 were applied to the measured galactic proton data from IMP - 8 measured in 1987 and PAMELA measured in 2008. The Convection-Diffusion and Force-Field approximate solutions were compared with the double power law parameterization. It was concluded that the results of the Convection-Diffusion and the double power law were largely the same with a difference of 15.1 %. Also, it was pointed out that the results obtained using the Convection-Diffusion approximation has never been reported before. That chapter has illustrated that the Convection-Diffusion approximate solutions of this study can be applied to fit measurements better than the Force-Field spectrum approximate solutions. A new proton LIS was calculated and used in this study. It was normalized according to the high energy PAMELA data of 2008 and at lower energies it was normalized according to Voyager - 1 data measured in 2012. Using the spectrum parameterization from the double power law and from the approximate solutions, the reference modulation parameters $M^{\mathrm{R}}(r_{t_{87}}, t_{87})$ and

$\phi^{\mathrm{R}}(r_{t_{87}},\ t_{87})$ were calculated. These were important for the calculation of the full modulation parameters.

In chapter 7, the time dependence of the full modulation parameters $M^f(r_t,\ t)$ and $\phi^f(r_t,\ t)$ were discussed. Further, the modulation parameter $\phi^f(r_t,\ t)$ calculated from neutron monitors using the Force-Field approximation in this study and those of *Usoskin et al.* (2005, 2011) were both discussed and compared. The normalized difference between the calculated modulation parameter $\phi^f(r_t,\ t)$ by *Usoskin et al.* (2011) and $\phi^f(r_t,\ t)$ by this study is about 5.1 % for the solar maximum of June 1991.

Further recommendations for calculating the modulation parameters $M^f(r_t,\ t)$ and $\phi^f(r_t,\ t)$ from the Convection-Diffusion approximation and the Force-Field approximation, respectively, include

- Recalculation of the modulation parameters using the helium LIS parameterization. That is essentially needed to verify that modulation described by these modulation parameters are the same when compared with those calculated from protons (from this study) or any other species.
- The 1-dimensional Parker transport equation approximate solution must be used to compare the calculated modulation parameters from the two semi-analytical methods in this study.

References

[1]. Adriani, O., G. C. Barbarino, G. A. Bazilevskaya, R. Bellotti, et al., The PAMELA mission: Heralding a new era in precision cosmic ray physics, *Physics Reports*, 544, pp. 323-370, 2014.

[2]. Adriani, O., G. C. Barbarino, G. A. Bazilevskaya, R. Bellotti, et al., PAMELA measurements of cosmic-ray proton and helium spectra, *Science*, 33(6025), pp. 69-72, 2011.

[3]. Alania, M. V., R. Modzelewska, and A. Wawrzynczak, On the Relationship of the 27-day Variations of the Solar Wind Velocity and Galactic cosmic ray Intensity in Minimum Epoch of Solar Activity, *Physics*, 270(2), pp. 629-641, 2011.

[4]. Babcock, H. W., The topology of the Sun's magnetic field and the 22-year cycle, *The Astrophysical Journal*, 133, pp. 572-587, 1961.

[5]. Balabin, YU. V., E. V. Vashenyuk, and P. H. Stoker, Solar Cosmic Ray study with Neutron Monitors of a Various Design, *Proceedings of the* 30th *International Cosmic Ray Conference*, 1, pp. 213-216, 2008.

[6]. Balogh, A., L. J. Lanzerotti, and S. T. Suess, The heliosphere through the solar activity cycle, *Springer-Praxis Books and Springer Science + Business Media*, 2008.

[7]. Bedijn, P. J., J. J. Burger, and B. N. Swanenburg, The Long-Term Modulation of Cosmic Rays, *Proceedings of the* 13th *International Conference on Cosmic Rays*, held in Denver, Colorado, 5, p. 3106, 1973.

[8]. Beer, J., K. McCracken, and R. Von Steiger, Cosmogenic Radionuclides: Theory and Applications in the Terrestrial and

Space Environments, Springer Berlin Heidelberg, *Physics of Earth and Space Environments*, 2012.

[9]. Blasi, P., Cosmic Ray Acceleration in Supernova Remnants, *Cosmic Rays for Particle and Astroparticle Physics*, pp. 493-506, 2011.

[10]. Brown, R., Neutron Yield Functions of the Nucleonic Component of Cosmic, *Nuovo Cimento*, 6, p. 2816, 1957.

[11]. Burger, J. J., A Phenomenological Approach to the Solar Modulation of Cosmic Rays, *Astrophysical Journal*, 166, p. 651, 1971.

[12]. Burger, J. J., and B. N. Swanenburg, Long-Term Solar Modulation of Cosmic-Ray Electrons with Energies above 0.5 GeV, *Proceedings of the* 12th *International Conference on Cosmic Rays*, held in Tasmania, Australia, 16-25 August, 1971. 2, p. 554, 1971.

[13]. Burger, R. A., M. S. Potgieter, and B. Heber, Rigidity dependence of cosmic ray proton latitudinal gradients measured by the Ulysses spacecraft: Implications for the diffusion tensor, *Journal of Geophysical Research*, 105, pp. 27447-27455, 2000.

[14]. Burlaga, L. F., N. F. Ness, M. H. Acuña, R. P. Lepping, et al., Magnetic fields at the solar wind termination shock, *Nature*, 454, pp. 75-77, 2008.

[15]. Caballero-Lopez, R. A., An estimation of the yield and response functions for the mini neutron monitor, *Journal of Geophysical Research* (*Space Physics*), 121, pp 7461–7469, 2016.

[16]. Caballero-Lopez, R. A., and H. Moraal, Cosmic-ray yield and response functions in the atmosphere, *Journal of Geophysical Research* (*Space Physics*), 117(A12103), 2012.

[17]. Caballero-Lopez, R. A., and H. Moraal, Limitations of the force field equation to describe cosmic ray modulation, *Journal of Geophysical Research*, 109(A01101), 2004.

[18]. Caballero-Lopez, R. A., H. Moraal, and C. D. Steenberg, Validity of the Force-Field Equation to Describe Cosmic Ray Modulation, *Proceedings of the* 28$^{\text{th}}$ *International Cosmic Ray Conference*, 2003.

[19]. Caballero-Lopez, R. A., H. Moraal, and F. B. McDonald, Galactic cosmic-ray modulation: effects of the solar wind termination shock and the heliosheath, *Journal of Geophysical Research*, 109(A05105), 2004.

[20]. Casolino, M., P. Picozza, and PAMELA Collaboration, The PAMELA experiment: A space-borne observatory for heliospheric phenomena, *Advances in Space Research*, 41(12), pp. 2043-2049, 2008.

[21]. Chmeleff, J., F. von Blanckenburg, K. Kossert, and D. Jakob, Determination of the Be-10 half-life by multicollector ionization chamber P-MS and liquid scintillation counting, *Nuclear Instruments and Methods in Physics Research Section* B, 268, pp. 192-199, 2010.

[22]. Clem, J. M., and L. I. Dorman, Neutron Monitor Response Functions, 2000.

[23]. Clette, F., L. Svalgaard, J. M. Vaquero, and E. W. Cliver, Revisiting the Sunspot Number. A 400-Year Perspective on the Solar Cycle, *Space Science Reviews*, 186, pp. 35-103, 2014.

[24]. Cliver, E., Solar energetic particles: Acceleration and transport, In B. D. Dingus (Ed.), Ray Conference, 516, pp. 103-119, 2000.

[25]. Compton A. H., E. O. Wollan, and R. D. Bennett, A precision recording cosmic-ray meter, *Review of Scientific Instruments*, 5(12), pp. 415-422, 1934.

[26]. Davis, L. Jr., Interplanetary Magnetic Fields and Cosmic Rays, *Physical Review*, 100, p. 1440, 1955.

[27]. Dorman, L. I., Cosmic Rays in the Earth's Atmosphere and Underground, *Astrophysics and Space Science Library*, *Kluwer Academic Publishers*, *Dordrecht*, 303, 2004.

[28]. Dorman, L. I., Cosmic rays, *North-Holland Publishing Company*, 1974.

[29]. Dorman, L. I., S. G. Fedchenko, L. V. Granitsky, and G. A. Rishe, Coupling and barometer coefficients for measurements of cosmic-ray variations at altitudes of 260-400mb, *Proceedings of the* 11$^{\text{th}}$ *International Cosmic Ray Conference*, 2, pp. 233-236, 1970.

[30]. Dorman, L., Cosmic Ray Variations, *State Publishing House for Technical*, 102, 1957.

[31]. Dunai, T. J., Cosmogenic Nuclides: Principles, Concepts and Applications in the earth Surface Sciences, *Cambridge University Press*, *Cambridge*, 198, 2010.

[32]. Effenberger, F., H. Fichtner, K. Scherer, S. Barra, et al., A generalized diffusion tensor for fully anisotropic diffusion of energetic particles in the heliospheric magnetic field, *The Astrophysical Journal*, 750(108), 1-8, 2012.

[33]. Engelbrecht, N. E., On the heliospheric diffusion tensor and its effect on 26-day recurrent cosmic ray variations, *Master's*

thesis, *North–West University* (*Potchefstroom Campus*), *South Africa*, 2008.

[34]. Fermi, E., On the Origin of the Cosmic Radiation, *Physical Review*, 75, p. 1169, 1949.

[35]. Ferreira, S. E. S., and M. S. Potgieter, Long-term cosmic-ray modulation in the heliosphere, *The Astrophysical Journal*, 603, pp. 744-752, 2004.

[36]. Ferreira, S. E. S., The heliospheric transport of galactic cosmic rays and Jovian electrons, *Ph.D. thesis*, *North-West University* (*Potchefstroom campus*), *South Africa*, 2002.

[37]. Fichtner, H., Anomalous cosmic rays: Messengers from the outer heliosphere, *Space Science Reviews*, 95, pp. 639-754, 2001.

[38]. Fisk, L. A., and G. Gloeckler, Acceleration of galactic cosmic rays in the interstellar medium, *The Astrophysical Journal*, 744(127), pp. 1-9, 2012.

[39]. Fonger, W., Cosmic Radiation Intensity-Time Variations and Their Origin, *Physical Review*, 91, 351, 1953.

[40]. Forbush, S. E., Cosmic ray intensity variations during two solar cycles, *Journal of Geophysical Research*, 63, pp. 651-669, 1958.

[41]. Forbush, S. E., On world-wide changes in cosmic-ray intensity, *Physical Review*, 54(12), pp. 975-988, 1938.

[42]. Forbush, S. E., Three unusual cosmic-ray increases possibly due to charged particles from the sun, *Physical Review*, 70(9-10), pp. 771-772, 1946.

[43]. Forbush, S. E., Three unusual cosmic-ray increases possibly due to charged particles from the sun, *Physical Review*, 70(9-10), pp. 771-772, 1946.

[44]. Forbush, S. E., World-wide cosmic-ray variations, 1937-1952, *Journal of Geophysical Research*, 59(4), pp. 525-542, 1954.

[45]. Forman, M. A., L. A. Fisk, and W. I. Axford, Particle Distribution Functions in Modulation Theory, *Proceedings of the* 13th *International Conference on Cosmic Rays*, held in Denver, Colorado, 2 (MG and SP Sessions), p. 663, 1973.

[46]. Gaensler, B., and P. Slane, The evolution and structure of pulsar wind nebulae, 36th *COSPAR Scientific Assembly*, held from 16-23 July 2006, in Beijing, China. Meeting abstract from the CDROM, #1683, 2006.

[47]. Gaggero, D., Cosmic Ray Diffusion in the Galaxy and Diffuse Gamma Emission, *Science + Business Media*, 2012.

[48]. Ghelfi, A., D. Maurin, A. Cheminet, L. Derome, et al., Neutron monitors and muon detectors for solar modulation studies: 2. ϕ time series, *eprint arXiv*:1607.01976, 2016.

[49]. Ginzburg, V. L., and S. I. Syrovatskii, The origin of cosmic rays, *New York: Gordon and Breach*, 1969.

[50]. Gleeson, L. J., and I. A. Urch, A study of the force-field equation for the propagation of galactic cosmic rays, *Astrophysics and Space Science*, 11, pp. 288-308, 1973.

[51]. Gleeson, L. J., and I. H. Urch, A Study of the Force-Field Equation for the Propagation of Galactic Cosmic Rays, *Astrophysics and Space Science*, 25(2), pp. 387-404, 1968.

[52]. Gleeson, L. J., and I. H. Urch, Energy losses and modulation of galactic cosmic rays, *Astrophysics and Space Science*, 11, pp. 288-308, 1971.

[53]. Gleeson, L. J., and W. I. Axford, Cosmic Rays in the Interplanetary Medium, *The Astrophysical Journal*, 149, L115-118, 1967.

[54]. Gleeson, L. J., and W. I. Axford, Solar modulation of galactic cosmic rays, *The Astrophysical Journal*, 154, pp. 1011-1026, 1968a.

[55]. Gleeson, L. J., and W. I. Axford, The Compton-Getting effect, *Astrophysics and Space Science*, 2(4), pp. 431-437, 1968.

[56]. Hanslmeier, A., The sun and space weather, *Astrophysics and Space Science Library*, 1st edition, 2002.

[57]. Hathaway, D. H., and R. M. Wilson, What the Sunspot Record Tells Us About Space Climate, *Solar Physics*, 224, 5-19, 2004.

[58]. Hathaway, D. H., The solar cycle, *Living Reviews in Solar Physics.*, 7, p. 1, 2010.

[59]. Hatton, C. J., and H. Carmichael, Experimental Investigation of the NM-64 Neutron Monitor, *Canadian Journal of Physics*, 42, pp. 2443-2472, 1964.

[60]. Hatton, C. J., and W. K. Griffiths, Barometric coefficients of multiplicities in neutron monitors, *Space Physics*, 73, pp. 7503-7509, 1968.

[61]. Heber, B., and M. S. Potgieter, Cosmic rays at high heliolatitudes, *Space Science Reviews*, 127, pp. 117-194, 2006.

[62]. Heber, B., and M. S. Potgieter, Galactic and anomalous cosmic rays through the solar cycle: New insights from Ulysses, in The Heliosphere through the Solar Activity Cycle, (Eds.) Balogh, A., Lanze-rotti, L. J., Suess, S. T., *Springer*, *Praxis*, *Berlin*, *New York*, *Chichester*, pp. 195-249, 2008.

[63]. Herbst, K., A. Kopp, B. Heber, F. Steinhilber, et al., On the importance of the local interstellar spectrum for the solar modulation parameter, *Journal of geophysical research*, 115(D00I20), 2010.

[64]. Hiltner, W. A., On the Presence of Polarization in the Continuous Radiation of Stars II, *Astrophysical Journal*, 109, p. 471, 1949.

[65]. Ihongo, G. D., and C.H.-T. Wang, The effects of solar wind on galactic cosmic ray flux at Earth, *Astrophysics and Space Science*, 361, p 44, 2016.

[66]. Jokipii, J. R., and E. N. Parker, On the convection, diffusion, and adiabatic deceleration of cosmic rays in the solar wind, *The Astrophysical Journal*, 160, pp. 735-744, 1970.

[67]. Jokipii, J. R., E. H. Levy, and W. B. Hubbard, Effects of particle drift on cosmic ray transport, I. General properties, application to solar modulation, *The Astrophysical Journal*, 213, pp. 861-868, 1977.

[68]. Korschinek, G., A. Bergmaier, T. Faestermann, U.C. Gerstmann, et al., A new value for the half-life of Be-10 by heavy-ion elastic recoil detection and liquid scintillation counting, *Nuclear Instruments and Methods in Physics Research Section* B: *Beam Interactions with Materials and Atoms*, 268(2), pp. 187-191, 2010.

[69]. Krimigis, S. M., R. B. Decker, E. C. Roelof, M. E. Hill, et al., Search for the exit: Voyager 1 at heliosphere's border with the Galaxy, *Science*, 341 (6142), pp. 144-147, 2013.

[70]. Krimsky, G. F., Diffusion mechanism of diurnal cosmic ray variations, *Geomagnetic Aeronomy* 4, pp. 763-769, 1964.

[71]. Manuel, R., Time-dependent modulation of cosmic rays in the outer heliosphere, *Ph.D. Thesis*, *North-West University* (*Potchefstroom Campus*), *South Africa*, 2013.

[72]. McComas, D. J., D. Alexashov, M. Bzowski, H. J. Fahr, et al., The heliosphere's interstellar interaction: No bow shock, *Science*, 336, pp. 1291-1293, 2012.

[73]. McCracken, K. G., and J. Beer, Long-term changes in the cosmic ray intensity at Earth, 1428-2005, *Journal of Geophysical Research*, 112(A10101), 2007.

[74]. Moore, R., and D. Rabin, Sunspots, *Annual Review of Astronomy and Astrophysics*, 23, pp. 239-266, 1985.

[75]. Moraal, H., Cosmic ray modulation studies in the outer heliosphere, *Nuclear Physics* B *Proceedings Supplements*, 33, Issue 1-2, pp. 161-178. 1993.

[76]. Moraal, H., Cosmic rays in the heliosphere: Observations, *Astroparticle Physics*, 53, pp. 175-185, 2014.

[77]. Moraal, H., Cosmic rays Modulation Equations, *Space Science Reviews*, 2011.

[78]. Moraal, H., M. S. Potgieter, and P. H. Stoker, Neutron monitor latitude survey of cosmic-ray intensity during 1986/1987 solar minimum, *Journal of Geophysical Research*, 94(A2), pp. 1459-1464, 1989.

[79]. Muscheler, R., J. Beer, G. Wagner, C. Laj, C. Kissel, et al., Changes in the carbon cycle during the last deglaciation as indicated by the comparison of ^{10}Be and ^{14}C records, *Earth and Planetary Science Letters*, 219(3-4), pp. 325-340. 2004.

[80]. Neher, H. V., Cosmic rays at high latitudes and altitudes covering four solar maxima, *Journal of Geophysical Research*, 76, pp. 1637-1651, 1971.

[81]. Parker, E. N., Cosmic Rays modulation by the solar wind, *Physics Revies*, 110, p. 1445, 1958.

[82]. Parker, E. N., Interplanetary Dynamical Processes, *John Wiley and Sons*, *New York*, 1963.

[83]. Parker, E. N., The passage of energetic particles through interplanetary space, *Planetary and Space Science*, 13, p. 9, 1965.

[84]. Pesses, M. E., J. R. Jokipii, and D. Eichler, Cosmic ray drift, shock wave acceleration, and the anomalous component of cosmic rays, *The Astrophysical Journal*, 246, L85-L88, 1981.

[85]. Picozza, P., A.M. Galper, G. Castellini, O. Adriani, et al., PAMELA: A payload for antimatter matter exploration and light-nuclei astrophysics, *Astroparticle Physics*, 27, pp. 296-315, 2007.

[86]. Potgieter, M. S., and H. Moraal, A drift model for the modulation of galactic cosmic rays, *The Astrophysical Journal*, 294, pp. 425-440, 1985.

[87]. Potgieter, M. S., Drift and observations in cosmic-ray modulation, 2, In NASA, Goddard Space Flight Center, 19th *International Cosmic Rays Conference*, 4, pp. 429-432, 1985b

[88]. Potgieter, M. S., Drift and observations in cosmic-ray modulation, 1, In NASA, Goddard Space Flight Center, 19th *International Cosmic Rays Conference*,.4, pp. 425-428, 1985a.

[89]. Potgieter, M. S., Solar cycle variations and cosmic rays, *J. Atmospheric and Solar-Terrestrial Physics*, 70, pp. 207-218, 2008.

[90]. Potgieter, M. S., The modulation of galactic cosmic rays in the heliosphere: Theory and models, *Space Science Reviews*, 83, pp. 147-158, 1998.

[91]. Potgieter, M., Solar Modulation of Cosmic Rays, *Living Reviews in Solar Physics*, 10, 2013.

[92]. Scharmer, G. B., B. V. Gudiksen, D. Kiselman, M. G. Löfdahl, et al., Dark cores in sunspot penumbral Filaments, *Nature*, 420, 2002.

[93]. Scherer, K., H. Fichtner, T. Borrmann, J. Beer, et al., Interstellar-terrestrial relations: Variable cosmic environments, the dynamic heliosphere, and their imprints on terrestrial archives and climate, *Space Science Reviews*, 127, pp. 327-465, 2006.

[94]. Schlaepfer, H., Cosmic rays, *Spatium*, pp. 3-15, 2003.

[95]. Schwabe, M., Die Sonne. Von Herrn Hofrath Schwabe, *Astronomische Nachrichten*, 20, pp. 283-286, 1843.

[96]. Schwadron, N. A., M. Owens, and N. U. Crooker, The heliospheric magnetic field over the hale cycle, *Astrophysics and Space Sciences Transactions*, 4, pp. 19-26, 2008.

[97]. Senanayake, U. K., V. Florinski, A. C. Cummings, and E. C Stone, Spectral Evolution of Anomalous Cosmic Rays at Voyager 1 beyond the Termination Shock, *The Astrophysical Journal*, 804, p. 12, 2015.

[98]. Shea, M. A., and D. F. Smart, 'Secular Variation in Cosmic Ray Cutoff Rigidities', *Journal of Geophysical Research*, 75, pp. 3921-3922, 1970.

[99]. Shea, M. A., D. F. Smart, and K. G. McCracken, A study of vertical cutoff rigidities using sixth degree simulations of the geomagnetic field, *Journal of Geophysical Research*, 70(17), pp. 4117-4130, 1965.

[100]. Shea, M., and D. Smart, *Space Science Reviews*, 93, p. 229, 2000.

[101]. Simpson, J. A, *Annual International Geophysical Year*, **4**, p. 351. 1957.

[102]. Simpson, J. A., Ground level events: the early years, *Proceedings of the* 21st *International Cosmic Ray Conference*, 12, pp. 187-195, 1990.

[103]. Simpson, J. A., The cosmic ray nucleonic component: The invention and scientific uses of the neutron monitors, *Space Science Reviews*, 93, pp. 11-32, 2000.

[104]. Smith, E. J., The heliospheric current sheet, *Journal of Geophysical Research*, 106(A8), p. 15819, 2001.

[105]. Stanev, T., High energy cosmic rays, 2nd edition, *Springer-Praxis*, *Berlin*, 2004.

[106]. Steinhilber, F. A., J. A. Abreu, J. Beer, I. Brunner, et al., 9,400 years of cosmic radiation and solar activity from ice cores and tree rings, *Proceedings of the National Academy of Sciences*, 109(16), pp. 5967-5971, 2012.

[107]. Stoker, P. H., L. I. Dorman, and J. M. Clem, Neutron monitor design improvements, *Space Science Reviews*, 93, pp. 361-380, 2000.

[108]. Stoker, P. H., M. S. Potgieter, and A. J. Veter, Variations in Cosmic-Ray Primary Spectrum from Recordings at SANAE by Neutron Monitors of Different Sensitivities, *Proceedings of the* 16th *International Cosmic Ray Conference*, 4, p. 358, 1979.

[109]. Stone, E. C., A. C. Cummings, F. B. McDonald, B. C. Heikkila, et al., Voyager 1 explores the termination shock region and the heliosheath beyond, *Science*, 309, pp. 2017-2020, 2005.

[110]. Stone, E. C., A. C. Cummings, F. B. McDonald, B. C. Heikkila, et al., An asymmetric solar wind termination shock, *Nature*, 454, pp. 71-74, 2008.

[111]. Stone, E.C., A.C. Cummings, and F.B. McDonald, Voyager 1 observes low-energy galactic cosmic rays in a region depleted of heliospheric ions, *Science*, 341, pp. 150-153, 2013.

[112]. Strauss, R. P., Modelling anomalous cosmic ray oxygen in the heliosheath, *Astronomy and Astrophysics*, 522, pp. 1-8, 2010.

[113]. Teufel, A., and R. Schlickeiser, Analytic calculation of the parallel mean free path of heliospheric cosmic rays. I. Dynamical magnetic slab turbulence and random sweeping slab turbulence, *Astronomy and Astrophysics Review*, 393, pp. 703-715, 2002.

[114]. Usoskin, G. I., A History of Solar Activity over Millennia, *Living Reviews in Solar Physics*, 5, 2013.

[115]. Usoskin, I. A., G. A. Bazilevskaya, and G. A. Kovaltsov, Solar modulation parameter for cosmic rays since 1936 reconstructed from ground-based neutron monitors and ionization chambers, *Journal of Geophysical Research*, 116(A02104), 2011.

[116]. Usoskin, I. G., K. Alanko-Huotari, G. A., Kovaltsov, and K. Mursula, Heliospheric modulation of cosmic rays: Monthly reconstruction for 1951-2004, *Journal of Geophysical Research*, 110(A12108), 2005.

[117]. Webber, W. R., and D. S. Intriligator, Voyager 1 and 2 Observations of Cosmic Ray Intensities in the North-South Heliosheaths-Implications for the Latitude Extent of the Heliospheric Current Sheet and Radial Structure in the Heliosheath, *eprint arXiv*:1403.3322, 2014.

[118]. Webber, W. R., and F. B. McDonald, Recent Voyager 1 data Indicate that on August 25, 2012 at a distance of 121.7 AU from the Sun, sudden and unprecedented intensity changes

were observed in anomalous and galactic cosmic rays, *Geophysical Research Letter*, 40, 2013.

[119]. Webber, W. R., and J. A. Lockwood, Voyager and Pioneer spacecraft measurements of cosmic ray intensities in the outer heliosphere: Toward a new paradigm for understanding the global modulation process: 1. Minimum solar modulation (1987 and 1997), *Journal of Geophysical Research*, 106(29), p. 323, 2001.

[120]. Widrow, L. M., Origin of galactic and extragalactic magnetic fields, *Reviews of Modern Physics*, 74(3), pp. 775-823, 2002.

[121]. Wilkinson, J., New Eyes on the Sun, Astronomers' Universe, *Springer-Verlag Berlin Heidelberg*, 2012.

[122]. Yiou, F., G. M. Raisbeck, S. Baumgartner, J. Beer, et al., Beryllium 10 in the Greenland Ice Core Project ice core at Summit, Greenland, *Journal of Geophysical Research*, 102(C12), pp. 26783-26794, 1997.